Interventional Vascular Enhancement Using Digital Tomosynthesis Facilitated by 2D-3D Registration

Alhrishy, Mazen

Awarding institution:
King's College London

Division of Imaging Sciences and

Biomedical Engineering

School of Medicine

KING'S College LONDON

Interventional Vascular Enhancement Using Digital Tomosynthesis Facilitated by 2D-3D Registration

by Mazen G. Alhrishy

A thesis submitted in partial fulfilment of the requirements for the degree of Doctor of Philosophy of the University of London

Sep 2015

Supervisors:

Dr. Graeme Penney

Dr. Andrew King

Examiners:

Prof. Dr. Wiro Niessen

Dr. Fernando Bello

Abstract

Endovascular image-guided surgery (EIGS) using C-arm fluoroscopy is being performed for more and more complex procedures with longer imaging times. An example of such complex procedures is fenestrated endovascular aneurysm repair (EVAR), which involves delivering bespoke stent-grafts through vasculature into the aneurismal area using low dose images. However, X-ray is much better at visualizing interventional devices and dense structures compared to vasculature. To enhance vascular visualisation, iodinated contrast medium (ICM) is injected and a significantly higher X-ray dose than standard low dose images is employed to produce a digital subtraction angiography (DSA) image. ICM usage is essential but nephrotoxic and can cause renal failure. DSA is also often a major contributor to the overall patient radiation dose. Furthermore, a DSA image is only valid for the current interventional view and not the new view once the C-arm is moved. The required high accuracy, the lengthy imaging time, and the large volumes of ICM used (with the associated radiation dose and high risks of renal failure) during fenestrated EVAR, have motivated this thesis to look into novel methods to enhance vasculature, and reduce ICM usage during complex EIGS procedures, while maintaining the clinical work-flow.

My first novel method proposes using an established two-dimensional (2D)-three-dimensional (3D) rigid registration system to facilitate improved interventional DTS (iDTS) reconstruction, using standard hardware, and with no ICM injection. This is achieved by a small angle C-arm sweep (e.g. 40°) to acquire intraoperative fluoroscopy images, which are then registered to the preoperative computed tomography (CT) volume. The proposed method automatically reconstructs patient-anatomy-specific images and removes clutter resulting from bony anatomy. Experiments were carried out using one phantom and 4 clinical datasets. Phantom results showed a 3419% signal difference to noise ratio (SDNR) improvement compared to standard fluoroscopy images. Patient results showed that the method enabled visualization of clinically relevant features: the outline of the aorta

and some aortic calcifications, without the injection of any ICM, and with much reduced radiation dose compared to DSA imaging.

The second method is an extension to the first method to enable much smaller vascular structures, such as the renal ostia, to be enhanced. This is achieved by injecting a much smaller ICM volume than is usually used for standard DSA imaging (e.g. 10-30%) during the C-arm sweep. Experiments were carried out using CT-based synthetic fluoroscopy images, to which simulated contrast was added in different amounts before deboned iDTS (de-iDTS) reconstruction. Numerical results showed that the reconstructed de-iDTS images with simulated contrast had better SDNR values compared to the synthetic DSA image with motion and noise artefacts. Reconstructed de-iDTS images showed that the renal ostia can be clearly seen after adding motion and noise when using 30% simulated ICM.

The third novel method proposes using the mentioned 2D-3D registration system to facilitate remapping a DSA image from one view to another, after the C-arm is moved. This is achieved by registering the two image views to the preoperative CT volume, which allows repeated ICM-free DSA imaging. Experiments were carried out using 9 clinical datasets. Numerical results showed an overall averaged remapping accuracy error of 2.73 mm, with 7 patients scoring averaged errors ≤ 3 mm. In addition, the overall averaged error was found to increase by 163% when using the 2D-3D overlay method, which was found to be statistically significant ($p < 0.01$).

In summary, I have developed novel imaging methods for vascular enhancement during interventional fluoroscopy using standard hardware. My novel methods have shown: 1) the potential to provide additional intraoperative information, which cannot be provided by the preoperative CT volume alone, such as the deformed aorta position with respect to interventional devices, and 2) the potential to enable a reduction in overall ICM usage, and radiation dose, while maintaining the clinical work-flow. I propose that these methods could find a role alongside DSA imaging, replacing DSA imaging where appropriate, while using DSA for critical points in the procedure. This is particularly beneficial for patients with renal insufficiency and/or patients at high risk of radiation adverse response. Because my novel method of iDTS can be directly employed on any standard fluoroscopy system, in addition

to vascular enhancement during EIGS, the method could be potentially used to enhance structures in other image-guided surgery (IGS) applications.

Acknowledgement

I would like to greatly thank my first supervisor Dr. Graeme Penney. There are not enough words to really describe my gratitude to Graeme. I thank him for helping me to apply for the King's overseas research studentship after finishing my MSc at KCL, which had made all of this possible. For the past 4 years, Graeme has never stopped supporting me, academically and personally, during the good and the bad times that I have been through. I would also like to thank my second supervisor Dr. Andrew King, who helped me to improve my programming skills, and was always available to answer any programming questions that I have.

Thanks also go to Mr. Tom Carrell for his clinical support and help in data acquisition, and to all the clinical staff at St. Thomas' Hospital who aided this research. Thanks to my colleagues Andreas Varnavas for putting up with all my questions about the 2D-3D registration system, and Alberto Gomez for sharing his programming experience.

The greatest thanks of all go to my mum and dad whom have always been proud of me, and of what I am doing.

I would like to acknowledge financial support from King's Overseas Research Studentship, and from the Cardiovascular Healthcare Technology Co-operative Innovation.

Contents

List of Figures

List of Tables

Abbreviations

2D two-dimensional.

3D three-dimensional.

AA aortic aneurysm.

AAA abdominal aortic aneurysm.

AP anterior-posterior.

CBCT cone-beam computed tomography.

CC cranial-caudal.

CT computed tomography.

De-iDTS deboned iDTS.

DRR digitally reconstructed radiograph.

DSA digital subtraction angiography.

DTS digital tomosynthesis.

EBRT external beam radiation therapy.

EIGS endovascular image-guided surgery.

EVAR endovascular aneurysm repair.

FBP filtered back projection.

FoV field of view.

Fps frames per second.

HU Hounsfield unit.

ICM iodinated contrast medium.

IDTS interventional DTS.

IGRT image-guided radiation therapy.

IGS image-guided surgery.

Linac linear accelerators.

MR magnetic resonance.

MRI magnetic resonance imaging.

PL profile line.

RAO/LAO right/left-anterior-oblique.

ROI region of interest.

SAA shift and add.

SDNR signal difference to noise ratio.

SID source to image distance.

TACT tuned aperture computed tomography.

US ultrasound.

Chapter 1

Introduction

Contents

The work presented in this thesis is primarily concerned with vascular enhancement during endovascular image-guided surgery (EIGS) interventions. In particular, fenestrated endovascular aneurysm repair (EVAR) procedures, which involve delivering bespoke stent-grafts through vasculature into the aneurismal area under C-arm fluoroscopy guidance. This chapter provides a brief summary of the clinical motivation, the structure of the thesis, and the main original contributions of this work.

1.1 Clinical Motivation

Image-guided surgery (IGS) offers significant advantages over open surgical procedures, as it allows interventionists to visualize their instruments' position with respect to the surrounding anatomy using a much smaller incision. IGS carries fewer risks of infection and post-procedure complications, and can result in a shorter recovery time [Schermerhorn et al., 2008].

The main focus of the work described in this thesis is EIGS interventions, which involve guiding different types of interventional devices through vasculature, and

into the targeted area to be treated. EIGS interventions have specific requirements which include, for example, the ability to visualize an instrument's position with respect to vasculature when needed, while maintaining the interventional work-flow. Imaging modalities employed for EIGS include: C-arm fluoroscopy and cone-beam computed tomography (CBCT), ultrasound (US), and magnetic resonance (MR).

No single modality fulfils all the requirements for EIGS use, however, the primary modality used for EIGS is C-arm fluoroscopy, due to its high availability and several advantages over other modalities [Perrin et al., 2009]. Nevertheless, a major disadvantage of fluoroscopy is the lack of good soft-tissue visualization. Using the same C-arm platform, CBCT can acquire three-dimensional (3D) images with better soft-tissue visualization than fluoroscopy. However, CBCT greatly interrupts the clinical work-flow, as the set-up time to acquire one CBCT image is often between 5-10 min [Wallace et al., 2008]. Repeated CBCT also involves a significant radiation dose [Bachar et al., 2007], and thus, is unlikely to be used repeatedly during EIGS, if used at all.

If accurate vascular information is required during EIGS interventions using fluoroscopy, iodinated contrast medium (ICM) is injected inside the vessels of interest, and a significantly higher X-ray dose than standard fluoroscopy is employed to enhance vascular visualization. To visualize only the enhanced vasculature, a digital subtraction angiography (DSA) image can be produced by subtracting background structures. ICM usage is essential for vascular enhancement in fluoroscopy imaging, but ICM is nephrotoxic, and can cause renal failure (reported by Nash et al. [2002] to be the third most common cause of hospital-acquired renal failure). DSA is also often a major contributor to the overall patient radiation dose (81% as reported by Patel et al. [2013]). Moreover, once the C-arm is moved to a new position, DSA imaging has to be repeated if accurate vascular information is needed.

The case study presented in this work as an example of EIGS is EVAR of abdominal aortic aneurysms (AAAs). This procedure involves positioning a stent-graft at the top and bottom of the aneurismal segment of the aorta to prevent it from rupture. EVAR candidates with unfavourable anatomy (e.g. aneurysm extending across visceral arteries) require fenestrated stent-grafts, which are more complex than standard stent-grafts. Fenestrated EVAR procedures require high guidance

accuracy, and involve lengthy imaging time (e.g. 294 min as reported by Kauffmann et al. [2015]) and increased risk of ICM induced renal complications due to the large volumes of ICM used compared to standard procedures [Haddad et al., 2005, Scurr and McWilliams, 2007]. It is reported that 50% of EVAR candidates require fenestrated EVAR [Ricotta and Oderich, 2008]. Such complex procedures could benefit greatly from novel techniques that offer enhanced vascular visualization with reduced ICM usage and radiation exposure, but still maintain the clinical work-flow.

Rigid two-dimensional (2D)-3D image registration has been the main technique developed to provide advanced vascular guidance during complex EVAR interventions. The technique overlays 3D preoperative vasculature onto 2D fluoroscopy images to aid guidance. The main limitation, however, is errors due to non-rigid intraoperative vascular deformation [Sailer et al., 2014], especially in very tortuous anatomy where the technique could be very beneficial. The deformation is caused by the introduction of stiff interventional devices [Demirci et al., 2009], and decreases the accuracy of any guidance in the deformed region [Sailer et al., 2014]. Developing non-rigid techniques is still a challenging area of registration research [Markelj et al., 2012].

The use of digital tomosynthesis (DTS) to aid interventional procedures rather than for diagnostic applications has been proposed in the literature (often known as interventional DTS (iDTS)). Using the same C-arm platform, iDTS enables the acquisition of 3D data from a limited C-arm rotation (e.g. 20° - 90°), instead of the semicircular (i.e. 180°) rotation required by CBCT. iDTS has showed recently the potential to reduce imaging time and patient dose compared to CBCT, with much less interruption to the clinical work-flow [Bachar et al., 2007]. Nevertheless, to my knowledge, iDTS has not yet been proposed to reconstruct patient-anatomy-specific 2D images to aid interventions in EIGS. Moreover, proposed iDTS methods still employ the same technique used in diagnostic DTS systems, which requires frequent geometrical calibration, and still suffer from out-of-plane clutter.

This thesis will investigate novel methods to enhance vascular visualization, and to reduce ICM usage and the associated radiation dose during complex EVAR procedures, while maintaining the clinical work-flow. Two main research objectives

will be investigated:

1. Enabling iDTS on a standard fluoroscopy system by employing a rigid 2D-3D image registration algorithm. This has the potential to automatically enhance specific vascular structure visualization without any ICM injection, and to reduce out-of-plane clutter and eliminate the need for frequent geometrical calibration, while maintaining the clinical work-flow.

2. Enabling DSA remapping from one view to another on a standard fluoroscopy system by employing the same rigid 2D-3D image registration algorithm. This has the potential to allow repeated ICM-free DSA imaging, and to reduce radiation dose, which could in turn allow interventionists to perform more complex procedures with longer imaging times.

1.2 Structure of the Thesis

This thesis contains 8 chapters. The original methodology and experimental work are described in chapters 4, 5, 6, and 7. The content of each chapter is described in the following.

Chapter 2: Clinical Background

This chapter focuses on EIGS, the main application of this work. The chapter gives an overview of EIGS interventions, and lists the most important requirements during the course of EIGS. The advantages and limitations of the currently available imaging modalities, in the context of the listed EIGS requirements are then discussed. Next, the chapter briefly discusses two of the main methods to aid EIGS guidance using fluoroscopy: DSA roadmaps, and 2D-3D image registration. Finally, the chapter presents an example case study of EIGS: complex EVAR of AAAs using fenestrated stent-grafts.

Chapter 3: Literature Review

This chapter focuses on the use of DTS as an interventional tool rather than a diagnostic one (i.e. iDTS). The first section of this chapter gives a basic overview of

diagnostic DTS, then describes the required information for reconstruction, and the main limitation which is out-of-plane clutter. In the second section, recent research on the use of iDTS to aid guidance during IGS and image-guided radiation therapy (IGRT) is discussed. The third section describes, in more detail, the main method to aid EIGS guidance using fluoroscopy: 2D-3D image registration, and discusses the main limitation of the registration: intraoperative deformation.

Chapter 4: iDTS Facilitated by 2D-3D Registration on a Standard Fluoroscopy System

This chapter proposes novel methods for vascular enhancement during EIGS by employing a 2D-3D image registration to enable iDTS. The chapter begins by defining three coordinate systems to describe the 2D-3D registration geometry. In the second part, the specific 2D-3D registration algorithm to enable iDTS on a standard fluoroscopy system is briefly described. The third part gives a detailed explanation of how the registration algorithm output can enable improved iDTS reconstruction, using patient-anatomy-specific surfaces, and with greatly reduced out-of-plane clutter. Then, the reconstruction process to produce patient-anatomy-specific 2D iDTS images is detailed.

Chapter 5: Investigation into Vascular Enhancement Using iDTS with No Iodinated Contrast

This chapter investigates the novel methods proposed in chapter 4 without the injection of ICM for vascular enhancement. The first part of this chapter explains the methods by which the clinical datasets were acquired, the experiments performed using the acquired datasets, and explains the validation methods used. The second part shows the numerical and reconstruction results from phantom and patient datasets, including iDTS imaging time and radiation exposure. Finally, results are discussed.

Chapter 6: Investigation into Vascular Enhancement Using iDTS with a Reduced Amount of Iodinated Contrast

This chapter is an extension to chapter 5. It also investigates the novel methods proposed in chapter 4 for vascular enhancement, however, a reduced amount of ICM compared to standard DSA is simulated for enhancement of small vascular structures. The first part of this chapter explains the methods by which the computed tomography (CT)-based synthetic dataset was produced. It also explains the methods used to introduce soft-tissue motion, and quantum-noise to the produced synthetic dataset, and explains the validation methods used. The second part shows the numerical and reconstruction results from the synthetic dataset. Finally, results are discussed.

Chapter 7: DSA Remapping Facilitated by 2D-3D Registration on a Standard Fluoroscopy System

This chapter proposes a novel method to remap a DSA image from one interventional view to another after the C-arm is moved during interventional fluoroscopy. The chapter starts by providing a brief overview of the nature of projection X-ray, and the problem of remapping projection data. The second part explains how the 2D-3D registration algorithm described in chapter 4 can be used to facilitate DSA remapping on a standard fluoroscopy system, and describes the expected remapping errors. Experiments and validation methods are then described in the third part. The fourth part shows the numerical and remapping results from patient datasets. Finally, results are discussed.

Chapter 8: Conclusions and Future Work

This chapter summarises the main conclusions of the novel methods presented in chapters 4-7, in the context of the original contributions described in the next section. Future research, and clinical impact and limitation of the developed methods are also discussed.

1.3 Original Contributions

The original contributions of this thesis can be summarized as follows:

1. For the first time, high contrast vertebral bone can be removed from fluoroscopy images prior to iDTS reconstruction. High attenuation bony features are the largest cause of out-of-plane clutter, and will greatly reduce iDTS image quality. Removing bone prior to reconstruction has the potential to greatly reduce the effect of out-of-plane clutter, and to improve iDTS image quality.

2. For the first time, patient-anatomy-specific iDTS images can be reconstructed, and automatically displayed to clinicians in their preferred 2D fluoroscopy view. Reconstructing 3D iDTS volumes requires interventionists to scan through 2D sections to find the clinically relevant information, which could interrupt the clinical work-flow. My method projects 3D iDTS information back into the used 2D view without requiring clinician interaction, thus, image acquisition and display would fit with the clinical work-flow.

3. For the first time, iDTS images are reconstructed without mechanical tracking of the X-ray source. Therefore, my methods do not depend on accurate geometrical calibration for accurate iDTS reconstruction, neither do they require access to C-arm position information. This is particularly important in C-arm systems which are known to exhibit gravity-induced mechanical flex. All of the above novelties were made possible by proposing for the first time 2D-3D image registration (between fluoroscopy images and preoperative CT scan) to facilitate improved iDTS reconstruction on a standard fluoroscopy system. To date, all proposed iDTS systems still employ the same technique used in diagnostic DTS systems to acquire the imaging geometry, which is to mechanically track the X-ray source as it travels around the patient. However, this requires frequent geometrical calibration and direct access to the C-arm position. In addition, proposed iDTS systems still suffer from the same main drawback, which is clutter resulting from out-of-plane high contrast features, and still reconstruct 3D iDTS volumes.

4. For the first time, DSA images can be remapped from one view to another after C-arm movement by using 2D-3D image registration. This has the potential to enable a reduction in the overall nephrotoxic ICM usage and radiation dose, while maintaining the clinical work-flow. This also has the potential to provide additional intraoperative information which cannot be provided by the preoperative CT volume alone, such as the deformed aorta position. DSA remapping is particularly beneficial for patients with renal insufficiency, and/or patients at high risk of radiation adverse response undergoing complex procedures.

Chapter 2

Clinical Background

Contents

The scope of this chapter is EIGS. The chapter starts by defining IGS, then gives a basic overview of EIGS procedures and the most important requirements

during the course of such procedures. The chapter then discusses the currently available imaging modalities for EIGS including C-arm fluoroscopy and CBCT, US, and MR. It then briefly discusses two of the advanced guidance methods used during fluoroscopy guided EIGS, which are: DSA roadmaps, and preoperative CT/MR to fluoroscopy registration. Finally, the chapter finishes by explaining EVAR of aortic aneurysms (AAs), which is the case study presented in this thesis.

2.1 Image Guided Surgery (IGS)

Traditionally, surgeons have performed procedures by gaining direct access into the area of interest inside the body, and using direct visual inspection. This, in many cases involves significant trauma to the patient to access the targeted area.

IGS, on the other hand, typically requires a much smaller incision, and thus, offers enormous advantages over open surgical procedures: it carries fewer risks of infection and post-procedure complications and can result in a shorter recovery time [Schermerhorn et al., 2008], and it can be performed on patients who are not suitable candidates for open surgery. IGS systems allow the surgeons to visualize their interventional instruments' positions with respect to the surrounding anatomical structures without the need for direct access into the body for visual inspection.

The term IGS might refer to the use of intraoperative information to guide an intervention, or to the use of pre- and intra- operative information for guidance. In the latter case, other terms such as computer aided surgery and computer assisted therapy might be used to imply the use of preoperative images. However, for the purpose of this thesis, the term IGS will be used to refer to the use of intraoperative images for guidance, unless the use of preoperative images is clearly mentioned.

In the case where IGS is used with preoperative images, intra- and pre- operative images are usually shown on separate displays, or if images have been fused by a registration system then information from the preoperative image is often overlaid onto the intraoperative image. Interventionists can then relate the intraoperative scene and preoperative data (mentally or by using the registration overlay), in order to help guide the procedure.

2.2 Endovascular Image Guided Surgery (EIGS)

The main application area of the work described in this thesis is EIGS, thus, more details are given hereafter about EIGS requirements and the currently available imaging modalities to guide vascular interventions. Examples of such procedures include balloon angioplasty, stent-graft placement, coiling of aneurysms, embolization and local drug delivery.

2.2.1 Overview

EIGS generally involves inserting a catheter intra -venously or -arterially through a small incision. The catheter is then guided through the vasculature and into the targeted area to be treated. The targeted area might be a segment of a vessel that has a stenosis or is totally occluded, an aneurismal segment of a vessel which might rupture, or it might be a hypervascular region such as a tumour bed. Depending on the pathology of the targeted area, EIGS might involve delivering devices such as balloons and stent-grafts, or delivering a drug or embolic material through the catheter [Rudin et al., 2008].

Different types of interventional devices could cause different amounts of deformation, as they exert different amounts of force against the blood vessels' walls depending on their characteristics (e.g. stiffness), especially when inserted into very angulated vasculature [Carrell et al., 2010].

Before an EIGS procedure is scheduled, usually a preoperative diagnostic scan using either CT or magnetic resonance imaging (MRI) is acquired to locate the targeted vessels and to plan the intervention. EIGS procedures, if required, are then carried out in an interventional suite, or hybrid operating theatre.

2.2.2 Interventional requirements

EIGS interventions have specific requirements which are different to those of open surgery procedures where a direct access to the targeted area is established. In the following, I list the most important requirements during the course of EIGS interventions:

i. Ability to visualize interventional devices: instruments should be clearly visible in the field of view (FoV), and not introduce artefacts. Artefacts could obscure instruments' contact with surrounding tissue making fine navigation difficult and potentially harmful [Perrin et al., 2009].

ii. Ability to visualize vasculature: interventionists should be able to visualize their instruments' position with respect to vasculature, when needed, to help them navigate into the targeted vessels. To enhance vascular visualization, contrast medium is usually injected into the blood vessels of interest.

iii. Low contrast media usage: nephrotoxic contrast medium should be used as little as possible due to its renal adverse effects (e.g. acute kidney injury) [McCullough, 2008].

iv. Low dose when ionizing radiation is used: exposure from ionizing radiation should be as low as reasonably achievable to allow repeated imaging during the course of the intervention, and therefore, to reduce the risk of radiation adverse response, especially for complex procedures with longer imaging times.

v. Maintaining the interventional work-flow: techniques and imaging methods used must fit with the surgical procedure work-flow, and preserve sterility requirements in the interventional room. This is particularly important during complex procedures which might take several hours to perform.

vi. Fast image acquisition: interventional images should be acquired and displayed in real-time* when required by surgeons to enable real-time guidance of interventional devices. In addition, both image acquisition and subsequent viewing of images should not cause interruption to clinical work-flow.

vii. High spatial resolution: this is required for accurate deployment of interventional devices against the aortic wall. In the case of complex procedures, precise positioning of devices within a few millimetres is essential to prevent, for

* Real-time or live is commonly referred to from an imaging perspective as acquiring 30 frames per second (fps) [Peters and Cleary, 2008]. However, for interventional modalities such as fluoroscopy, the frame rate is often kept low (e.g. 2-3 fps) in order to reduce the dose to the patient. Therefore, in the context of IGS, I refer to real-time if the frame rate is greater than 1 fps.

example, visceral vessel loss when deploying fenestrated stent-grafts [O'Neill et al., 2006].

viii. Good patient access and compatible interventional tools with the imaging modality.

2.3 Current Imaging Modalities for EIGS

C-arm fluoroscopy is still the imaging modality of choice today for EIGS due to its high availability and several advantages over other modalities [Perrin et al., 2009]. Other imaging technologies such as CBCT, US, and MR have also been employed for EIGS in an effort to address the limitations of traditional fluoroscopy.

2.3.1 Fluoroscopy

Fluoroscopy utilizes X-ray with cone-beam geometry to form 2D images, which are projection images. Traditionally, fluoroscopy has employed an image intensifier to detect X-rays, which are then converted into visible light after amplification to be displayed on a monitor. In the late 1990s, however, digital flat-panel detectors have been developed as an alternative to the image intensifier.

Figure 2.1 illustrates the dynamic interventional scene during fluoroscopy guided EIGS. The X-ray source and detector are mounted on a C-arm which can translate and rotate around the patient to almost any view direction. The C-arm components can be moved to a less obstructive position if needed. Moreover, the workspace can be modified by translating both the C-arm and patient table apart from each other or close together.

During the course of an intervention, the C-arm position is regularly adjusted (often many times each minute) from a control panel by a radiographer or by the surgeon to acquire optimum 2D projection views for that particular stage of the procedure. Images can be instantly displayed on a set of display screens for the surgeon to visualize changes of interventional devices' position in real-time. Care needs to be taken during C-arm movement so that the anesthetic equipment will not be in the C-arm path, and that the surgical sterile area will not be compromised.

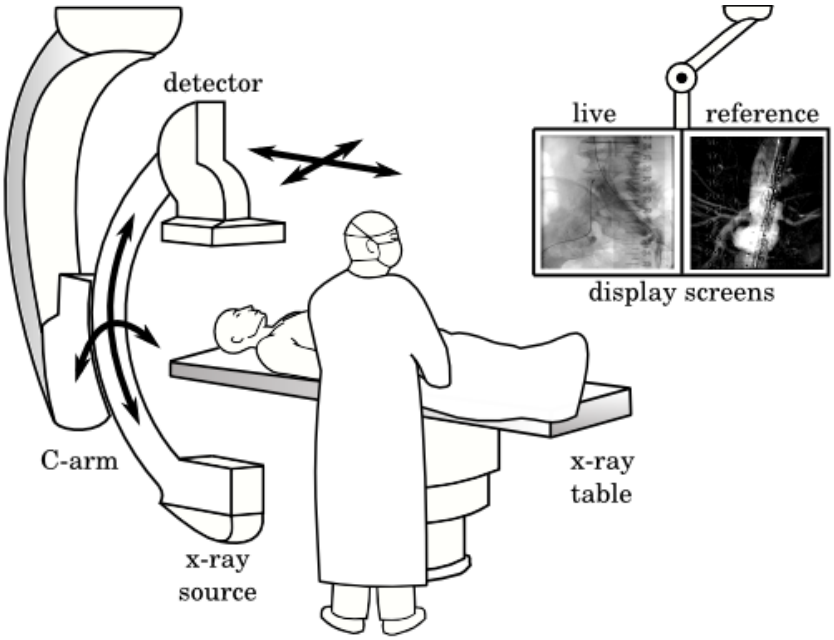

Figure 2.1: Standard interventional fluoroscopy setting. The C-arm can be positioned (rotated and translated) to acquire real-time 2D images from almost any view direction. The C-arm position will change many times during the course of the procedure. The real-time 2D image, plus useful previously acquired 2D images, are displayed so the surgeon can easily see them while manipulating the interventional instruments.

Standard fluoroscopy images are acquired using low dose X-ray (often known as screening images) to reduce the radiation exposure for both the patient and the interventional team as imaging time can be lengthy (e.g. 294 min for complex procedures as reported by Kauffmann et al. [2015]). Example screening images are shown in Fig. 2.2, where only interventional devices and dense tissues such as bone are adequately visualized, but not soft-tissue anatomy such as vasculature. This is because the difference in attenuation coefficients between blood and surrounding soft-tissue is very small.

To enhance vascular visualisation, ICM is injected into the blood vessels through an automatic pump connected to the patient, and a significantly higher X-ray dose than standard screening images is employed to acquire high spatial resolution images (know as angiography imaging which produces a sequence of angiography images) [Patel et al., 2013]. An example angiography image showing ICM inside parts of the aorta is seen in Fig. 2.3.b. To visualize only the contrast flow and remove background structures, a mask image is acquired before the contrast injection ('a'),

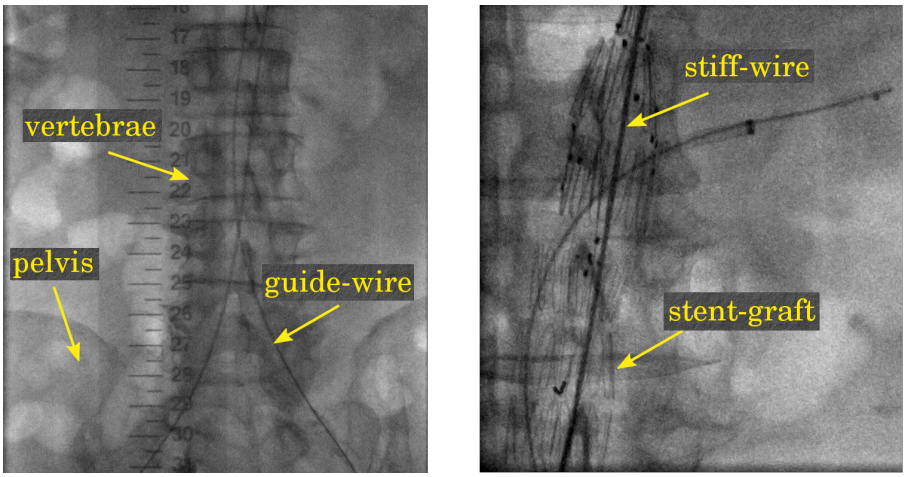

Figure 2.2: Example standard screening images using low dose X-ray. The real-time 2D images clearly show high contrast structures such as the interventional instruments and bony anatomy, but not vasculature.

and then subtracted from the subsequent angiography images resulting in a DSA image showing only the enhanced vasculature, such as the aorta shown in 'c'. More details about DSA imaging are given in Sec. 2.4.1.

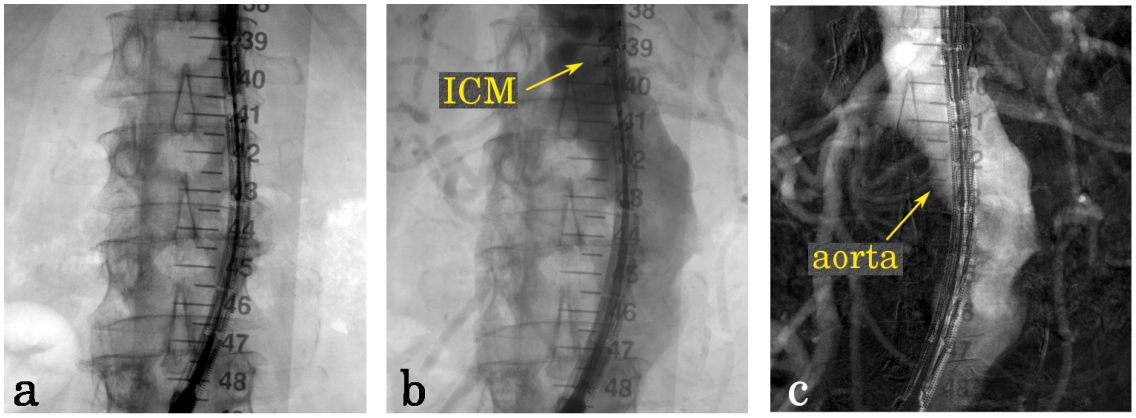

Figure 2.3: Enhancing vascular visualisation using iodinated contrast medium (ICM) and high dose X-ray. a) Contrast-free mask image, b) example angiography image showing ICM inside parts of the aorta, and c) the produced DSA image showing the enhanced aorta.

In order to reduce respiratory motion artefacts during DSA imaging, patients are asked to hold their breath if they are under regional or local anaesthesia, or the ventilator is switched off if patients are under general anaesthesia. The interventional team then step away (if not holding interventional instruments) from the patient's table to reduce occupational exposure due to the high radiation dose used

in DSA imaging. Producing a DSA image could take $\sim$ 1 min, and in some situations, DSA images have to be repeated (e.g. substantial motion artefacts or ICM pump not working).

ICM usage is routine during interventional procedures, nevertheless, it must be administered sparingly as the contrast medium is nephrotoxic and can cause renal failure [McCullough, 2008]. DSA was also reported to contribute most of the patient radiation dose (81%) during EIGS [Patel et al., 2013]. Moreover, a DSA image is only valid for the current interventional view, and once the C-arm is moved, the previous DSA image does not correspond to the new interventional view. Thus, during most procedures, DSA imaging will be repeated several times due to C-arm movement which could cause additional interruption to the clinical work-flow. In Sec. 2.4.1, more information is given about DSA imaging and its drawbacks.

2.3.2 Cone-beam computed tomography

Although fluoroscopy has the required advantages for EIGS, images still suffer from the absence of information about the dimension parallel to the beam. Clinicians still view 2D projection images, which simply integrate all information along the beam path. This often results in clinically relevant information being obscured by over- or under- lying anatomy.

With the arrival of large-area flat-panel digital detectors, modern fluoroscopy systems can now acquire multiple projections by a single semicircular rotation of the C-arm around the patient. These projections can then be reconstructed to produce CT-like 3D images. Because the X-ray beam in fluoroscopy systems is collimated into a cone rather than a fan (as in conventional CT), the technique is generically referred to as cone-beam computed tomography (CBCT) [Wallace et al., 2008].

CBCT offers images in multiple viewing planes, as opposed to conventional single-planar fluoroscopy or angiography, thus, it is now being offered by all major fluoroscopy manufacturers and is beginning to play a complementary role to fluoroscopy and angiography in EIGS [Siewerdsen et al., 2005].

However, the set-up time to acquire one CBCT image is approximately 5-10 min which could cause a large interruption to the clinical work-flow, especially if multiple acquisitions are required [Wallace et al., 2008]. This is because the 180°

C-arm rotation requires accurate centering of the patient, and clearing the large rotational path of any equipment to prevent possible collisions and to preserve surgical sterility. Repeated CBCT also involves a significant radiation dose [Bachar et al., 2007]. Moreover, the 3D nature of CBCT images requires some interaction from interventionists to scan through 2D sections to find the clinically relevant information to be displayed on the interventional screens. This could cause an additional interruption to the clinical work-flow.

For these reasons, CBCT is not a natural interventional modality, and is unlikely to be used repeatedly during EIGS interventions to aid guidance (e.g. CBCT was never used during the course of the interventions for any of the patients participating in this study). In addition, for high quality CBCT image reconstruction, the C-arm's precise position at each projection view is required. However, for flexible mechanical platforms such as the C-arm, issues of stability and gravity-induced mechanical flex can pose reconstruction challenges, thus, frequent geometric calibration is required to reduce associated artefacts [Siewerdsen et al., 2007].

2.3.3 Ultrasound

Dynamic (i.e. real-time) US imaging can provide continuous visualisation with no ionising radiation. Other advantages include mobility, cost effectiveness, compactness (with the vast majority of machines mounted on small wheeled carts), and ease of use (featuring hand-held probes which can be handled with high flexibility to image in a variety of planes). US transducers can also be inserted into vasculature using special catheters for direct access to target vessels (known as intravascular US).

However, unlike other modalities, US does not provide full sectional slices of the body, but only regional images with an effective viewing depth of about 20 cm on a typical medical system. This can cause inexperienced clinicians to lose orientation since acoustic windows (subject to the constraints of overlying bone and air structures) do not always allow image acquisition in typical anatomical planes. In these cases, it is difficult to avoid disorientation, particularly with 2D images, and clinicians must 'mentally' interpret the oblique views [Peters and Cleary, 2008].

In addition, the US probe must be held tightly against the skin at all times,

either by a clinician or an assistant, which leaves only one free hand for other tasks such as manoeuvring the interventional tools.

Another barrier to the interventional use of US is the difficulty in visualizing metal instruments. Often instruments are either not visualized or cause strong artefacts that make visualizing the precise relative position and orientation of instruments with respect to tissue very difficult [Huang et al., 2007]. This in turn can make fine navigation difficult because instrument contact with tissue is not clear, potentially leading to tissue damage [Perrin et al., 2009].

The most common EIGS interventions performed under US guidance are endovenous procedures for treatment of the great saphenous vein incompetence (e.g. varicose veins). Endovenous procedures were developed as a minimally invasive alternative to the conventional stripping surgery. During the procedure, catheters able to emit laser or radiofrequency waves are inserted under US guidance into the saphenous veins with the intention to ablate an incompetent superficial vein [Puggioni et al., 2005].

US is also used frequently to guide the initial common femoral artery access at the start of fluoroscopy guided EIGS in order to reduce the number of attempts, time to access, and vascular complications [Seto et al., 2010]. For this purpose, a needle steering device is attached firmly on the transducer to fix the needle's angle of entry to intersect the target vessel along a predicted route. The tip of the puncture needle is monitored continuously until it intersects the target vessel [Holm and Skjoldbye, 2000].

2.3.4 Magnetic resonance

MR has been advocated as a new and promising modality for EIGS since the early 1990s [Dumoulin et al., 1993, Kandarpa et al., 1993]. However, the adoption of endovascular interventions using MR has been slow. There is still much debate about the efficacy of intraoperative MR in terms of cost effectiveness, patient outcome, image resolution, and work environment compatibility [Peters, 2006].

MR combines various advantages compared to other imaging modalities. Unlike X-ray based imaging, MR allows the visualization of both blood vessels and adjacent soft-tissue without the use of ionizing radiation, and with low complication rate from

MR contrast media. Other advantages include excellent soft-tissue contrast, ability to acquire high quality anatomical images combined with functional information (e.g. blood flow velocities), and multiplanar 2D and 3D imaging of the vascular anatomy and catheter position in any desired imaging plane [Henk et al., 2005].

Nevertheless, one of the major limitations of MR is the high magnetic field which creates a hazardous work environment. The strength of the field increases rapidly towards the center of the magnet and is strong enough to pull-in any ferromagnetic objects with potentially fatal results. Patients with certain implants and devices (e.g. aneurysm clips and cardiac pacemakers) might be unsafe in the MR environment due to possible movement or excessive heating of these objects if they are made from ferromagnetic materials [Henk et al., 2005].

Standard interventional devices such as guide-wires and catheters are usually made of metallic alloys that may or may not be MR compatible. The ability of these devices to be clearly visualized is also dependent on the pulse sequences used. Furthermore, long conductive wires might operate as an antenna during radiofrequency excitation causing inductive heating around the wire, which is potentially harmful to the patient [Liu et al., 2000, Nitz et al., 2001]. This means that many interventional devices have to be redesigned solely for MR based interventions [Bartels and Bakker, 2003]. Developing safe yet visible interventional tools remains a challenge to interventional MR [Raman and Lederman, 2007].

Another major challenge facing interventional MR regarding magnet design is patient access. Diagnostic MR scanners were not designed for interventional use. The standard bore of the scanner is long and only slightly wider than the patient in order to create a homogeneous main magnetic field. This leaves very little space for instruments and for clinicians' hands and arms.

Open MR designs operating within the range of 0.2 - 1.0 Tesla have been developed for interventional purposes using large flat pole magnets. However, according to Bartels and Bakker [2003], vascular interventions require a field strength of at least 1.5 Tesla to acquire high spatial and temporal resolution. Developing the so-called 'double-doughnut' MR scanner which uses two vertical 1.5 Tesla magnets with a gap in between for easy patient access was a milestone in interventional MR [Schenck et al., 1995]. However, the field strength of 0.5 Tesla inside the gap is not

suited for vascular applications.

Since no MR scanner suitable for EIGS purposes is available yet [Bartels and Bakker, 2003], combined X-ray and MR systems (i.e. XMR) have been developed in a setup that enables quick patient transport between the two systems, with the first clinical trial for cardiovascular interventions reported by Razavi et al. [2003].

2.4 Advanced Guidance for EIGS Using Fluoroscopy

As described in Sec. 2.3.1, vasculature is not well visualized using standard fluoroscopy screening images. This is because the difference in attenuation coefficients between blood and surrounding soft-tissue is very small. In the following, I describe some of the main techniques developed to provide advanced vascular imaging guidance during interventional fluoroscopy.

2.4.1 Digital subtraction angiography (DSA) roadmaps

The gold-standard technique to visualize vasculature using fluoroscopy is to inject ICM into the blood vessels, then employ a significantly higher X-ray dose than standard fluoroscopy screening to visualize the opacified vessels of interest as contrast flows over time (i.e. angiography imaging as was highlighted in Sec. 2.3.1). A DSA image can then be produced by subtracting high contrast background objects from the angiography images as these objects will obscure lower contrast blood vessels containing dilute iodine.

Modern fluoroscopy machines have the capability to superimpose the produced DSA image directly onto live fluoroscopy images, thus, acting as a 2D roadmap for the interventionist to improve image guidance by providing a reference to navigate through vasculature in the absence of ICM.

Figure 2.4 illustrates the basic steps to produce a DSA roadmap which are:

1. A mask image is acquired before administration of ICM (‘a’).

2. ICM is injected intra-arterially and an angiography sequence showing the contrast flow over time is obtained.

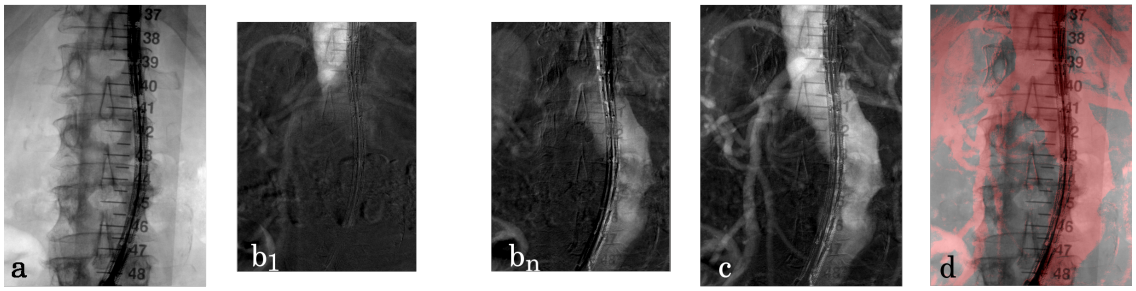

Figure 2.4: Basic principle to produce a digital subtraction angiography (DSA) roadmap. a) The mask image is subtracted (pixel by pixel) from all individual frames in the angiography sequence ($b_1 \sim b_n$). c) A DSA image is generated from the subtracted frames using the maximum intensity projection method. d) The DSA image is superimposed onto the live fluoroscopy image (in red colour).

3. All individual frames in the angiography sequence are subtracted, pixel by pixel, from the mask image to remove background high contrast structures ('b'$_1 \sim$ 'b'$_n$).

4. The subtracted frames are then used to generate a DSA image ('c'), using the maximum intensity projection method. In this method, only pixels with the highest intensity values throughout the subtracted frames are projected into a single image.

5. The DSA image is enhanced (e.g. contrast enhancement using display windowing techniques [Brody, 1982]) and superimposed onto the live fluoroscopy image to aid guidance ('d').

DSA motion artefacts

Although DSA imaging is still the gold-standard technique to enhance vascular visualization during fluoroscopy, a serious disadvantage of this technique is motion artefacts. If no soft-tissue motion exists between the mask and the subsequent angiography images, the DSA image will only show the iodinated vascular structures. However, when motion occurs between pre- and post- ICM injection images, the mask subtraction will not totally cancel out all background structures, and movement artefacts will appear in the DSA image, reducing its guidance quality.

Sources of motion artefacts include bowel gas and intestinal peristaltic motion

which may cause artefacts in DSA images of the abdominal region [Hillman et al., 1981]. Respiratory and cardiac motion may also cause motion artefacts in DSA images of the thoracic and abdominal regions [Boxt, 1983].

An example of motion artefacts in the produced DSA image can be clearly seen in Fig. 2.5 which shows a) the mask image, b) an example angiography image, and c) the produced DSA image. Bowel motion during ICM injection has caused substantial artefacts in the bottom half of the DSA image 'c'. Some blood vessels are substantially blurred-out as a result of the respiratory and cardiac motion (e.g. compare the vessel indicated by the red arrow between 'b' and 'c'). The stent-graft is also not totally cancelled-out after subtraction because of aortic pulsatile motion.

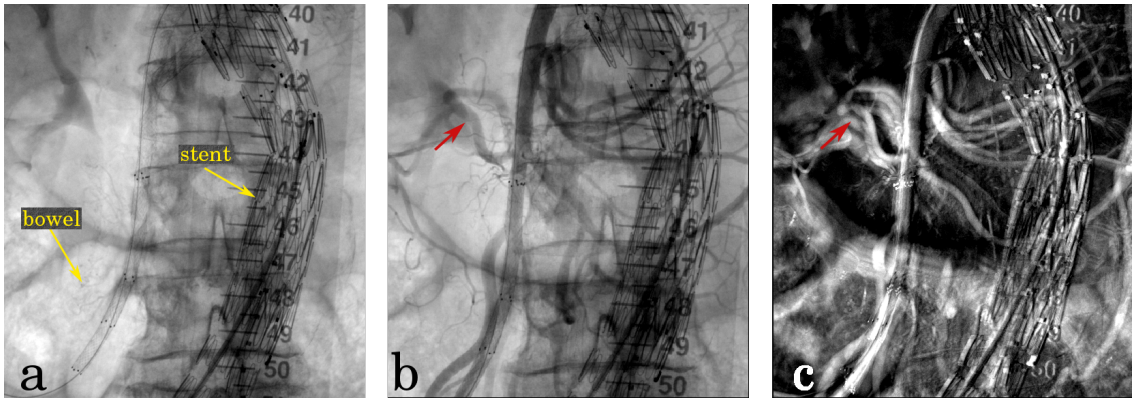

Figure 2.5: An example of motion artefacts in the produced DSA image. a) Mask image, b) an example angiography image, and c) the produced DSA image. Substantial artefacts are seen in the bottom half of 'c' as a result of bowel motion. Some blood vessels (e.g. indicated by the red arrow in 'c') are substantially blurred-out as a result of the respiratory and cardiac pulsatile motion, with the stent-graft not totally cancelled-out in 'c'.

Many techniques have been proposed to solve motion artefacts (see Meijering et al. [1999] for a full review). Early techniques attempted to reduce patient motion during exposure by using, for example, breath holding methods [Withers and Ashleigh, 1995]. Other techniques modify the acquisition system by taking advantage of a priori knowledge about the nature of patient motion, such as ECG gating where images are acquired during the same cardiac phase [Manhart et al., 2011].

Nevertheless, while these techniques help to reduce motion artefacts to some extent, patient motion always occurs. In such situations, motion artefacts may be

corrected after acquisition by means of image processing techniques. An example of these retrospective techniques is image registration where angiography images are processed in order to calculate a geometrical transformation that accounts for the changes caused by patient motion, and thus, brings the mask image and the angiography images into geometrical correspondence prior to subtraction [Meijering et al., 1999].

Additional DSA disadvantages

In addition to motion artefacts, DSA imaging has the following disadvantages which relate to ICM usage and X-ray nature:

i. A DSA roadmap is only valid for the current interventional view, and once the C-arm or the patient table is moved, the previous DSA roadmap does not correspond to the new interventional view. Therefore, during most procedures, DSA roadmaps are often repeated if accurate information on vasculature is required after C-arm movement. This increases ICM usage and the associated radiation dose.

ii. ICM is nephrotoxic and can cause acute kidney injury. ICM-induced acute kidney injury accounts for a significant number of cases of hospital-acquired renal failure [McCullough, 2008], and it was reported to be the third most common cause of hospital-acquired renal failure [Nash et al., 2002]. Patients with ICM-induced acute kidney injury are also at high risk of in-hospital complications, including a mortality rate of 20% [Seeliger et al., 2012]. This is likely to continue being one of the challenges for angiography imaging as chronic kidney disease and diabetes are becoming more prevalent in an ageing population.

iii. Radiation dose from DSA imaging was reported to contribute most of the patient radiation dose during endovascular interventions (81%), even though ICM was used as sparingly as possible [Patel et al., 2013]. This is due to the fact that angiography imaging requires a significantly higher radiation dose than standard fluoroscopy screening. With interventionists performing more and more complex procedures with longer screening times and more DSA imaging, there are growing concerns resulting from the increasing radiation exposure to both patients and the interventional team [Miller, 2009].

iv. DSA imaging uses projection X-ray. Therefore, enhanced 3D vasculature

is projected into a 2D image which could obscure clinically important information along the projection trajectory. An example is shown in Fig. 2.6 which shows a) a DSA image of the aorta produced from approximately an anterior-posterior (AP) view, and b) a surface rendering of the aorta produced from the CT data from a similar view to the DSA image. The indicated vessel's ostium in 'b' (red arrow) is inaccurately identified in 'a' (yellow arrow) because it is obscured by the aorta.

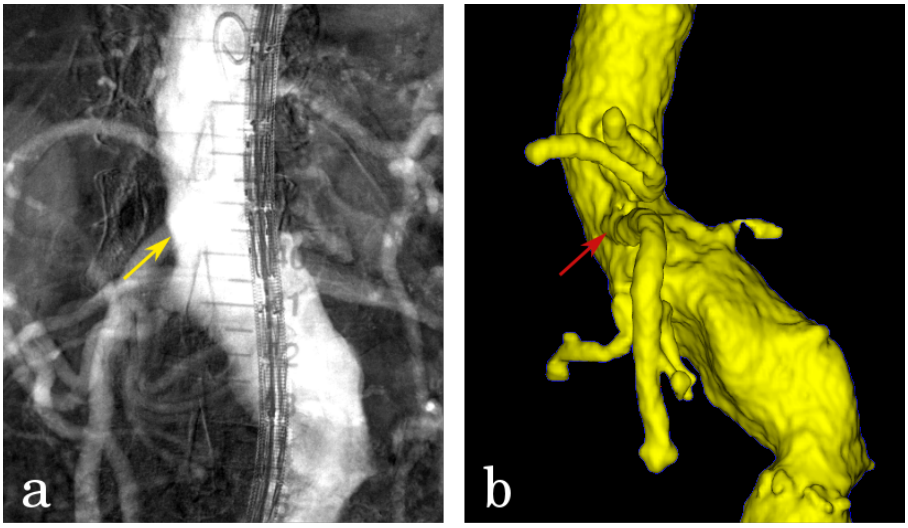

Figure 2.6: An example of vasculature overlap in the produced DSA image. a) A DSA image of the aorta produced from ∼AP view, and b) a CT surface rendering of the aorta also produced from ∼AP view. The vessel's ostium indicated by the red arrow in 'b' is inaccurately identified in 'a' (yellow arrow) because it is obscured by the aorta.

2.4.2 Preoperative CT/MR to fluoroscopy registration

Although C-arm fluoroscopy is still the main modality for guiding EIGS, it suffers from several drawbacks. Fluoroscopy lacks good soft-tissue visualization and can only depict blood vessels when filled with nephrotoxic ICM. Fluoroscopy also produces projection images which do not adequately depict complex 3D spatial relationships of vasculature, which is needed for navigation in complex procedures. On the other hand, CT and MR are more suited for pretreatment imaging and have better soft-tissue visualization and offer 3D images of vasculature.

By registering 3D preoperative data of CT [Weese et al., 1997] or MR [Hipwell et al., 2003] to the intraoperative 2D fluoroscopy image, important vascular

information inside the preoperative volume can be projected onto the fluoroscopy image. This provides interventionists with complementary information about the current position of their instruments relative to vasculature without injecting any contrast medium, leading to a better guidance, increased accuracy, and reduction in procedure time and ICM volume [Sailer et al., 2014].

In Fig. 2.7, clinically relevant vascular information (the renal ostium position) is projected from the surface of the registered CT aorta onto the fluoroscopy image to improve guidance.

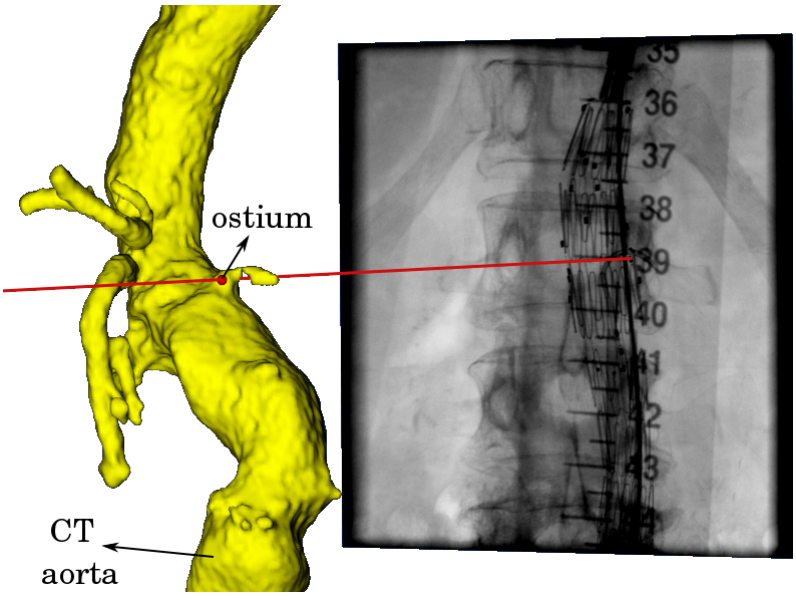

Figure 2.7: Example of CT to fluoroscopy registration. After registration, the position of the renal ostium on the surface of the CT aorta is projected into the fluoroscopy image to provide information about the current position of the ostium relative to instruments.

In order to use the 3D preoperative data for intraoperative guidance, it must be accurately aligned with the 2D intraoperative image, so that anatomical structures in both images correspond. This requires aligning the preoperative image coordinate system with the intraoperative image coordinate system, using what is known as 2D-3D image registration [Markelj et al., 2012].

The main limitation of image registration for EIGS procedures, however, is the intraoperative deformation of vasculature [Carrell et al., 2010, Sailer et al., 2014]. During endovascular procedures, vessel shape is subject to non-rigid motion and severe deformation that is imposed by the introduction of stiff endovascular

devices (see Sec. 2.2.1), such as delivery-systems and stiff-wires [Demirci et al., 2009]. Therefore, any rigid registration would decrease the accuracy of guidance in the deformed region. Non-rigid registration methods are still under investigation (see Markelj et al. [2012] for a recent review) but none are currently in regular clinical use.

More details are given about 2D-3D image registration in Sec. 3.3.

2.5 Case Study: Endovascular Aneurysm Repair (EVAR) Using Fluoroscopy

The case study presented in this thesis as an example of EIGS is EVAR of AAs.

EVAR procedures, being minimally invasive, have become increasingly popular. They involve a stent-graft placement across the aneurysm. The graft is composed of fabric and metal stents and comes mounted in a delivery-system. The delivery-system, which is known to cause the largest amount of deformation [Carrell et al., 2010], is inserted through the iliac arteries until the stent-graft is positioned at the top and bottom of the aneurismal segment. Once deployed, blood flows inside the stent-graft, removing pressure from the aneurysm wall.

EVAR is usually performed in the interventional radiology suite under general, regional, or local anaesthesia. Procedure duration can vary depending on the complexity of the aneurysm from as short as 90 min for a routine uncomplicated procedure, up to several hours for more complex ones [Gordon and Toursarkissian, 2014]. Hospital stay is significantly reduced (compared to open surgery) to one to two days. Two randomised trials that compared surgical and endovascular repair demonstrated a lower operative mortality rate for EVAR and less frequent complications than with conventional open surgery repair [Greenhalgh, 2004, Prinssen et al., 2004].

AA is defined as a dilation of the wall of the aorta and is usually described by its location. AAA is a dilation of the part of the aorta that is located in the abdomen and is further classified into three categories depending on its relationship to the renal arteries as illustrated in Fig. 2.8, where the labels in the figure match the following description:

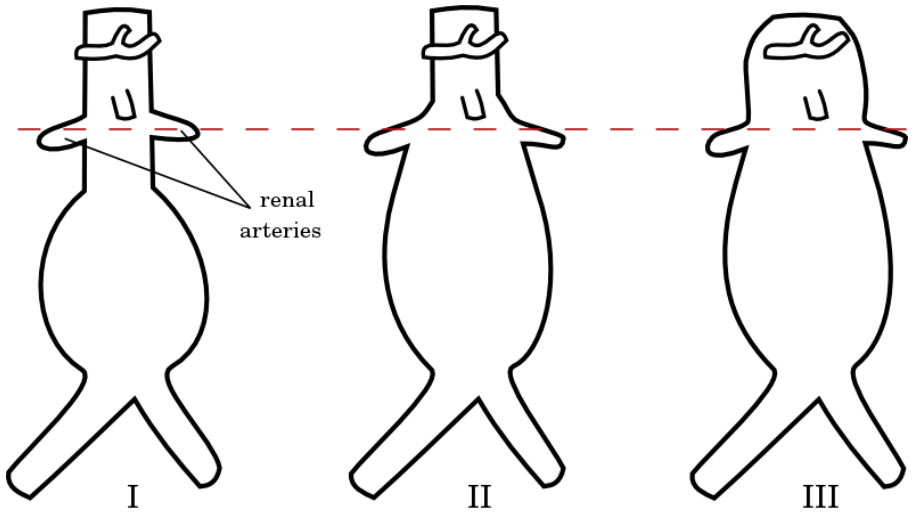

Figure 2.8: AAA classifications depending on the dilation location in relation with the renal arteries. Dilation is: i) below the renal arteries (infrarenal), ii) at the level of the renal arteries (pararenal), and iii) above the renal arteries (suprarenal).

i. Infrarenal AAA: dilation is below the renal arteries.

ii. Pararenal AAA: dilation is at the level of the renal arteries.

iii. Suprarenal AAA: dilation is above the renal arteries.

The diameter of a healthy infrarenal aorta varies with age, sex, and body weight [Bengtsson et al., 1996]. AAA is diagnosed if the infrarenal aorta is 3 cm in diameter or greater [Upchurch and Schaub, 2006]. Patients who have an infrarenal diameter $<$ 5.5 cm are at low risk of rupture, thus, intervention is not recommended [Anderson et al., 2013]. However, patients who have an infrarenal diameter $>$ 5.5 cm are at high risk of rupture [Robinson et al., 2013] and are candidates for EVAR [Brady et al., 2004]. Patients with ruptured AAA have an overall mortality rate between 65% and 85% [Thompson, 2003] and about half of deaths occur before reaching the surgical room [Wilmink et al., 1999].

AAA occurs primarily among people 65 years of age or older and is more prevalent in white people [Gordon and Toursarkissian, 2014]. Men are 5.6 times more likely to develop an AAA than women [Lederle et al., 2002]. The single most important risk factor for development and progression of AAA is tobacco smoking where smokers have been found to have 4 times higher prevalence than life-long non-smokers [Lindholt et al., 2001, Vardulaki et al., 2000].

AAAs are usually screened using abdominal US. However, if the US findings are not conclusive, an angiography CT scan is acquired [Gordon and Toursarkissian, 2014]. If the diameter of the infrarenal aorta is indicative of an intervention, an angiography CT scan is performed (or the existing scan is used) to determine the appropriate treatment plan depending on the category and complexity of the aneurysm.

In the case of infrarenal aneurysms, standard commercially available stent-grafts can be used for treatment, such as the one seen in Fig. 2.9.a. However, patients with complex anatomy such as short or angulated infrarenal aortic necks, or pararenal or suprarenal AAA are not suitable candidates for EVAR using standard stent-grafts as the ostia of the visceral vessels (renal, superior mesenteric, or celiac arteries) will be compromised.

It is estimated that 50% of patients with AAA have such complex anatomy [Ricotta and Oderich, 2008], and thus, cannot benefit from a standard endovascular repair. However, the introduction of fenestrated stent-grafts in the late 90s [Browne et al., 1999], has offered a new approach that made endovascular repair a possibility, even for complex cases. Fenestrated grafts are individually bespoke devices according to the locations of the visceral arteries acquired from the diagnostic CT scan. The graft has an opening (termed fenestration) for each of the visceral vessels involved as seen in Fig. 2.9.b, where the renal, superior mesenteric, and celiac arteries all have precise openings on the graft.

Deployment of fenestrated grafts requires a high level of precision to align the fenestrations with their target vessels (error $\leq$ 3 mm [Carrell et al., 2010]), and thus, is more complex than standard graft deployment. Misalignment could stop blood flow to vital organs and carries a high risk of renal failure, bowel ischaemia, and spinal cord ischemia [Gordon and Toursarkissian, 2014]. Fenestrated repairs are also associated with a significant risk of adverse renal events due to the large volumes of ICM used compared to standard repairs [Haddad et al., 2005, Scurr and McWilliams, 2007]. Further guidance complications might occur if the initial position of the partially-deployed stent-graft covers vessel ostia, thus, preventing contrast flow into the target vessels [Penney et al., 2011].

The required high accuracy during endovascular treatment of complex AAA,

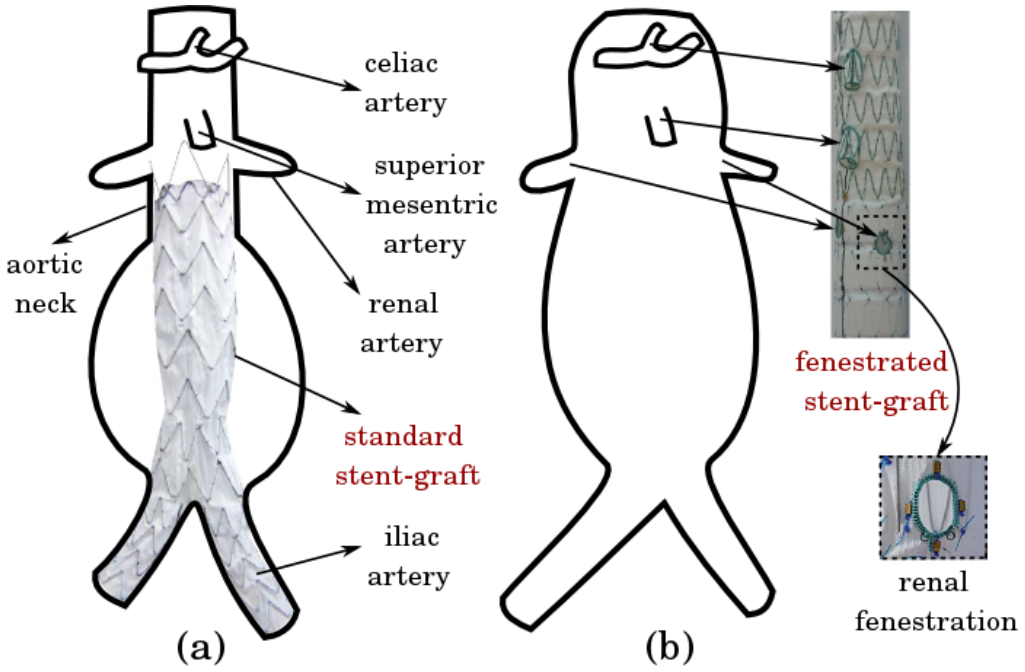

Figure 2.9: Standard versus fenestrated stent-grafts design. a) Standard commercially available stent-graft can be used for treatment of infrarenal aneurysms, however, in b) a fenestrated stent-graft is used for treatment of a suprarenal AAA, where the renal, superior mesenteric, and celiac arteries all have precise openings on the graft.

and the increased risk of ICM induced renal complications with the difficulties in visualising target vessels, have motivated this thesis to look into novel methods to improve image guidance accuracy, and to reduce ICM usage, and thus reduce contrast associated complications and radiation exposure.

2.6 Summary

This chapter has discussed the advantages and limitations of the currently available imaging modalities in the context of EIGS suitability, and it is clear that no single modality fulfils all the requirements for EIGS use.

C-arm fluoroscopy is still the primary modality for guiding vascular interventions due to its high availability, ability to visualize interventional devices with no artefacts and in real-time, fast image acquisition while maintaining the interventional work-flow, and high spatial resolution. The major drawback of fluoroscopy, however, is the lack of good soft-tissue visualization and the need for nephrotoxic ICM to depict blood vessels. CBCT uses the same C-arm platform to provide better

soft-tissue visualization with 3D imaging capability. However, CBCT greatly affects the clinical work-flow, and involves higher radiation exposure than fluoroscopy, and thus, is unlikely to be used repeatedly during vascular interventions, if used at all.

Complex vascular procedures, such as EVAR of AAAs using fenestrated grafts, require high accuracy and involve increased risk of ICM induced renal complications. I believe that such complex vascular interventions would benefit from novel techniques that offer better soft-tissue visualization with reduced ICM usage and radiation exposure, but still maintain the clinical work-flow. This thesis will investigate potential methods to enable this on standard fluoroscopy systems.

Chapter 3

Literature Review

Contents

In the first section of this chapter a basic overview of diagnostic DTS is given, with the required information for reconstruction and main limitation highlighted. In the second section, recent research on the use of DTS for interventional procedures rather than for diagnostic applications is discussed (which is often known as iDTS). This includes using iDTS to aid guidance during IGS and IGRT. The third section describes the main method employed and proposed in the literature for advanced guidance during EIGS using fluoroscopy. This is 2D-3D image registration. I highlight some of the differences between registration methods, and discuss the main limitation of the most widely used methods which use rigid registration.

3.1 Diagnostic Digital Tomosynthesis (DTS)

DTS is a form of limited angle tomography that uses conventional digital X-ray equipment to produce a 3D stack of cross-sectional slices of an object [Levakhina et al., 2013].

In the following, a basic overview of diagnostic DTS systems is given including the most commonly used imaging geometries and reconstruction algorithm. I also explain the required information for reconstruction, and the main limitation of DTS imaging. The main diagnostic DTS applications are also highlighted.

3.1.1 Overview

DTS involves acquiring a number of 2D projection images as the X-ray tube moves over a prescribed path. The total angular range of movement is often less than 40° [Dobbins III, 2009].

The term "tomosynthesis" was coined in a paper by Grant [1972] to refer to the ability to synthesize an infinite number of arbitrary tomograms after acquisition of a discrete number of images. However, problems with practical implementation at that time prevented clinical use of tomosynthesis as early devices required an X-ray film for each projection acquisition. This made the procedure time consuming and too cumbersome. Later on, commercially available fluoroscopy devices with

image intensifiers were used to acquire discrete projections instead of screen-films. However, noise and distortion associated with image intensifiers caused artefacts in reconstructed tomograms. Post-processing was also affected by the analogue nature of the imaging system (e.g. the use of analogue video cameras).

The situation changed substantially in the late 1990s, however, when digital flat-panel detectors capable of producing high quality digital images at fast readout rates were introduced [Dobbins III and Godfrey, 2003]. Currently, tomosynthesis is receiving an increased attention due to its ability to provide 3D information at lower dose, shorter acquisition time, and potentially lower cost than CT in specific clinical imaging situations where circular scan is unavailable (e.g. due to space limitations). Main applications include detecting breast microcalcifications and tumors, detecting chest pulmonary nodules, and dental or orthopaedic imaging [Levakhina et al., 2013].

3.1.2 Imaging geometry

Imaging geometries for DTS vary depending on the clinical application. Nevertheless, in all cases 2D projection images are acquired during a single motion of the X-ray tube over a prescribed path. Figure 3.1 shows the three most commonly used imaging geometries: a) parallel path, b) partial isocentric, and c) full isocentric [Dobbins III, 2009].

Parallel path geometry ('a') is usually used in chest and abdominal tomosynthesis where both the X-ray tube and detector move in parallel planes. Partial isocentric geometry ('b') is used in almost all current breast tomosynthesis where the detector moves in a plane (or remains stationary), while the X-ray tube moves in an arc above the detector. In full isocentric geometry ('c'), particularly involving C-arm devices, the tube and detector are locked together and rotate in a circular path around the patient who is approximately at the centre of rotation*.

* Semicircular isocentric motion used in CBCT is not considered one of the tomosynthesis techniques because it reconstructs a fully isotropic 3D image [Dobbins III, 2009].

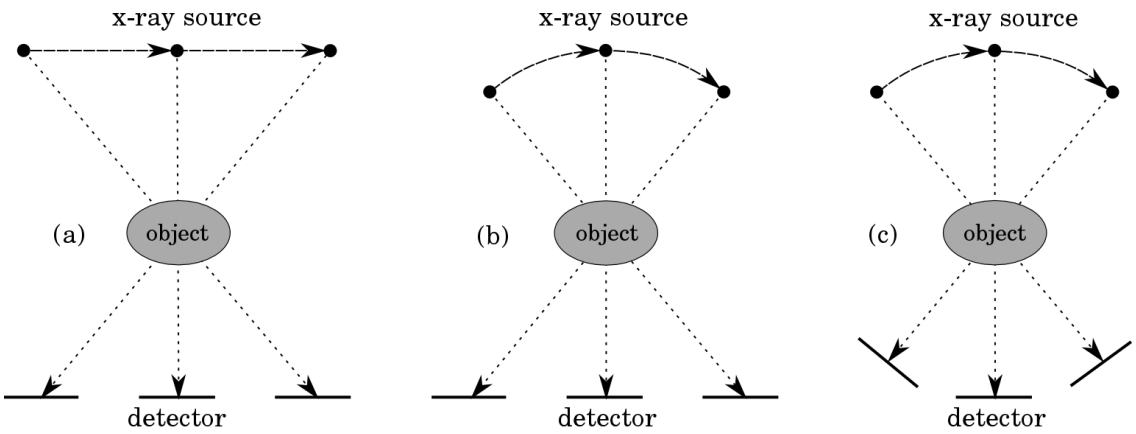

Figure 3.1: The three typically used imaging geometries in DTS. a) In parallel path geometry both the X-ray tube and detector move in parallel planes, b) in partial isocentric geometry the detector moves in a plane (or remains stationary), while the X-ray tube moves in an arc, and c) in full isocentric geometry both the tube and detector are locked together and rotate in a circular path.

3.1.3 The shift and add reconstruction algorithm

DTS is most commonly understood to mean reconstructing a stack of slices from the summation of a shifted finite number of 2D projection images acquired during a single pass of the X-ray tube. This is commonly referred to as the shift and add (SAA) method (Fig. 3.2).

The SAA method takes into consideration the fact that in the case of parallel path geometry (Fig. 3.1.a), magnification of objects is uniform at each X-ray tube position and is only dependant on their location above the detector and not on the tube or detector locations. Therefore, it is possible to shift each of the 2D projection images by a given amount and then add them together in such a way that structures in a chosen plane are brought into focus, while structures in other planes are blurred. By selecting the shift amount correctly, objects in different planes can be brought into focus.

This method is illustrated in Fig. 3.2, where the X-ray tube in 'a' has five positions to image an object which includes two planes of interest, one containing a circular object (plane A), and the second containing a triangular object (plane B). As the X-ray tube moves from one position to another, the relative projected locations of the circle and triangle change depending on their relative height above

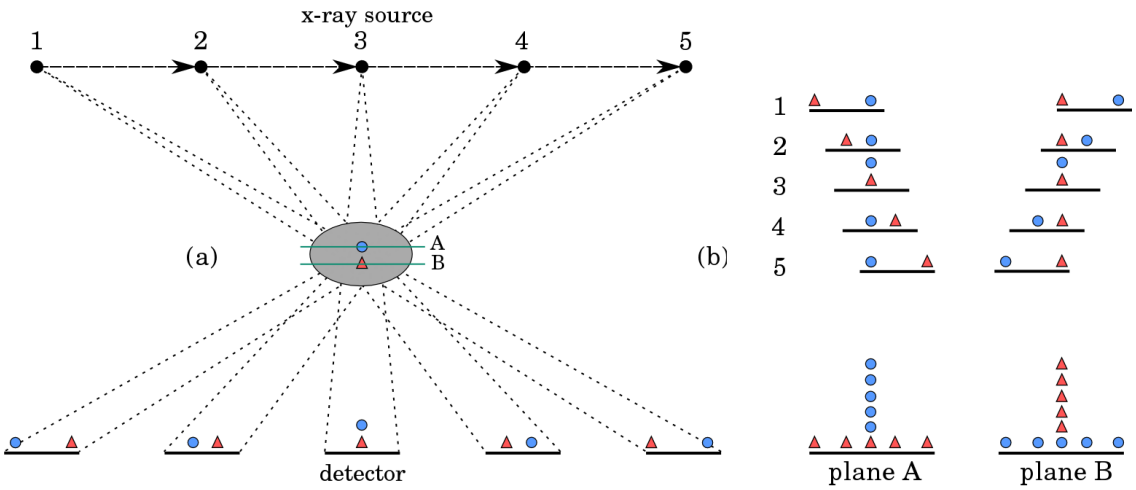

Figure 3.2: The shift and add reconstruction method in DTS imaging. a) As the X-ray tube moves from one position to another, the relative projected locations of the circle and triangle change. b) The five resulting projection images can be shifted and added so structures in either plane (A) or (B) are all made to line up exactly, and thus be in focus while structures in other planes are distributed over the image, and thus appear blurred.

the detector. The five resulting projection images seen in 'b' can be shifted and added so that structures in either plane (A) or (B) are all made to line up exactly, and thus be in focus, while structures in other planes are distributed over the image, and thus appear blurred.

Nevertheless, in partial isocentric geometry, the X-ray tube and detector do not move in parallel paths leading to variations in magnification [Niklason et al., 1997]. Moreover, in full isocentric geometry, the magnifications are uniform but the detector does not move on a path parallel to any plane in the patient [Kolitsi et al., 1992]. Therefore, in both isocentric geometries, more complex transformations of the 2D projection images must be performed to simulate parallel path geometry prior to SAA.

Due to its simplicity and little computational cost, most DTS reconstruction algorithms are based on the SAA method [Dobbins III, 2009]. However, two challenges have to be addressed to produce high quality DTS slices. In the following, I describe the challenges facing standard DTS slice reconstruction, and explain the main effect which limits image quality.

3.1.4 Required information for reconstruction

In standard diagnostic DTS equipment, a number of slices which are parallel to the detector plane* are usually reconstructed with uniform spacing depending on the clinical application. For example, when imaging the breast, a uniform spacing of about 1 mm is usually used [Skaane et al., 2012], whereas a wider uniform spacing of about 5 mm is usually used when imaging the chest [Dobbins III, 2009]. Therefore, prior to reconstruction, it is not possible to define a reconstruction plane to image specific regions of the patient's anatomy.

When performing SAA reconstruction, it is essential to align the constituent 2D projection images in such a way that structures of interest in a given plane are brought into focus. This requires precise knowledge of the source and detector position in order to determine the relative positions of the images, and thus, the amount of shift needed for each image.

In current tomosynthesis, the relative positions of the 2D projection images are solely determined by tracking the position of the X-ray tube as it travels around the patient using hardware in the imaging system. This requires sufficient mechanical stability and precision of the machine, which is ensured by frequent calibrations using dedicated equipment. In addition, patient motion should be considered during acquisition to ensure that the desired structures will be aligned properly after shifting the acquired images. However, if the patient moves slightly or if mechanical imprecision exists during acquisition, then blurring in the reconstructed slice can occur and low contrast objects would be reconstructed poorly, unless patient motion is corrected for [Dobbins III, 2009].

In order to address this positional imprecision in the imaging geometry, Webber et al. [1997] introduced a method known as tuned aperture computed tomography (TACT). In TACT, a set of fiducial markers are placed on the patient, and then projection images are acquired at a number of angles and orientations. By using the projected locations of the fiducial markers, the relative position of the acquired images can be calculated after taking into account the patient movement, and then

* In full isocentric geometry, the detector does not move on a path parallel to any plane in the patient. Therefore, DTS images are reconstructed in the view which is parallel to the imaging plane the rotation is centered around. For example, if the rotation is centered around the AP view, coronal DTS images are reconstructed; whereas if the rotation is centered around the lateral view, sagittal DTS images are reconstructed.

reconstructed in the required planes. The TACT approach has been applied to various clinical imaging tasks, however, the procedure to determine the desired slice position is time consuming as it requires identifying the locations of all fiducial reference points in each projected image, then drawing a line from each identified location to the centre of gravity, which is computed from the 2D distribution of all the identified locations. Moreover, attaching external fiducial markers to patients, unless it is already part of the clinical procedure, greatly complicates the image acquisition process.

3.1.5 Main limitation: out-of-plane clutter

The major problem of DTS is the data incompleteness, as only a limited number of projection images are acquired over a limited angular range around the patient. This results in image blurring and limited spatial resolution in the direction perpendicular to the imaging plane of the reconstructed volume (which will be referred to as the out-of-plane direction in this thesis) [Bliznakova et al., 2012, Levakhina et al., 2013].

A basic SAA reconstruction method (which is equivalent to basic back projection [Dobbins III, 2009]), would suffer from considerable blur artefacts from high contrast structures lying outside the plane of interest. This would lower the contrast and detectability of structures of interest, and can mask low contrast structures of interest like soft-tissue [Dobbins III and Godfrey, 2003]. This can be clearly seen in Fig. 3.2.b, where if the triangle represented high contrast bone, it would be distributed over the entire image and superimposed on the focused circle reducing its contrast, which in this example would be low contrast soft-tissue structures.

Several de-blurring algorithms have been investigated to correct for out-of-plane "clutter", and to enhance DTS image quality (a review of such algorithms can be found in Dobbins III and Godfrey [2003]). Currently, two categories of de-blurring algorithms are in use: filtered back projection (FBP) algorithms, and iterative reconstruction algorithms [Sechopoulos, 2013].

Iterative methods have excellent middle and high frequency noise properties and can reconstruct DTS images with superior quality and fewer artefacts compared to FBP, however, they are computationally intensive and time-consuming [Baker and Lo, 2011, Dobbins III et al., 2008]. On the other hand, FBP is computationally

fast with excellent low frequency noise properties, but the quality of the reconstruction depends greatly on the applied filter to the projection data before the back-projection is performed [Sechopoulos, 2013].

FBP is the de-blurring algorithm that is most commonly used by DTS manufacturers due to its computational efficacy. Nonetheless, optimizing de-blurring algorithms for out-of-plane noise removal is still under investigation, for example, to combine the excellent noise properties of iterative methods (at middle and high frequency) with the excellent noise properties of FBP (at low frequency) [Dobbins III, 2009].

3.1.6 Diagnostic applications

In the last decade DTS has been mostly used for diagnosis of breast lesions [Baker and Lo, 2011, Skaane et al., 2012, Teertstra et al., 2010] and pulmonary nodules in the chest [Galea et al., 2014, Tingberg, 2010].

For breast imaging, DTS improves the detectability of lesions as it provides 3D information instead of the 2D projection images provided by the current gold-standard breast screening modality, i.e. mammography. For chest imaging, DTS is used as an alternative to CT, which is the current gold-standard for detection and characterization of nodules in the lung. This is because DTS offers improved nodule detection without the cost or radiation dose associated with CT [Dobbins and McAdams, 2009, Lacout et al., 2012].

Further proposed applications include orthopedic imaging for joints and bone disease studies [Duryea et al., 2003, Flynn et al., 2007, Gomi et al., 2013, Shimao et al., 2008, Shiomi and Nishii, 2014], and dental imaging [Ogawa et al., 2010].

3.2 Interventional Digital Tomosynthesis (iDTS)

A promising area of research is the use of DTS for interventional procedures rather than for diagnostic applications (which is often known as iDTS).

In the following, I highlight the recent research on the use of iDTS. This includes using iDTS to aid guidance during IGS and IGRT.

3.2.1 Overview

iDTS takes advantage of the same source and detector configurations used in flat-panel C-arm systems to enable the acquisition of 3D data from a limited C-arm rotation instead of a full semicircle (i.e. CBCT).

By acquiring images over a limited arc (e.g. $20° \sim 90°$), iDTS can produce 3D data with a much lower image acquisition time, reconstruction time, and radiation dose compared to CBCT, as fewer images are acquired. Furthermore, iDTS causes much less interruption to the clinical work-flow, as clearing the rotational path of interventional devices to prevent collisions and preserve sterility is much easier for a small arc compared to CBCT. The trade-off, however, is reduced image quality (especially in the out-of-plane direction) and soft-tissue visibility [Bachar et al., 2007].

To date, the majority of iDTS research has been investigating this technique as a fast and low dose real-time 3D target localization tool in IGRT, for both external beam radiation therapy (EBRT) [Baydush et al., 2005, Godfrey et al., 2006, Wu et al., 2007, Yoo et al., 2009], and prostate brachytherapy [Lee et al., 2008, Tutar et al., 2003]. Recently, however, an iDTS prototype system has been suggested for the first time to aid IGS of the head, neck, sinus, and skull base by Bachar et al. [2007, 2009] and Siewerdsen et al. [2007]. The prototype was based on a mobile isocentric C-arm system which was modified to acquire 3D iDTS data of phantoms and head cadavers.

To my knowledge, iDTS has not yet been proposed to reconstruct patient-anatomy-specific 2D images to aid interventions in EIGS. Moreover, while current research proposes employing iDTS in IGS and IGRT by reconstructing 3D images, in fact, all proposed iDTS systems still employ the same technique used in diagnostic DTS systems, and thus, use mechanical tracking of the X-ray source which requires frequent geometrical calibration, and still suffer from the same main drawback: out-of-plane clutter.

3.2.2 iDTS for image-guided surgery

iDTS was recently proposed to aid IGS by Bachar et al. [2007, 2009] and Siewerdsen et al. [2007]. Taking advantage of the development of high performance flat-panel detectors, Siewerdsen et al. [2007] modified a mobile C-arm system (Siemens PowerMobil) to have multi-mode imaging functionality during IGS. Imaging modes included: fluoroscopy for real-time 2D guidance, iDTS for limited angle fast and low dose 3D imaging, and CBCT for semicircular isocentric 3D imaging.

Using phantoms and head cadavers only, Bachar et al. [2007, 2009] and Siewerdsen et al. [2007] demonstrated the potential for improved surgical performance during IGS of the head, neck, sinus, and skull base using iDTS. The studies employed a method for geometric calibration, and investigated image quality, acquisition and reconstruction times, and radiation dose for various acquisition arcs ($10° \sim 178°$).

Geometric calibration

In order to determine the relative positions of the acquired 2D projection images during the C-arm rotation, the modified system used the same technique employed in diagnostic DTS equipment, i.e. mechanical tracking of the C-arm head as it travels around the patient (see Sec. 3.1.4).

Nevertheless, C-arm systems are known to exhibit geometrical variations with the X-ray source and detector deviating more than 15 mm from a perfect circular orbit due to gravity-induced mechanical flex [Daly et al., 2008]. When these geometric variations in the source-detector orbit are not accurately corrected for during image reconstruction, the input images are misregistered, which can result in a loss of detail and image artefacts [Siewerdsen et al., 2005].

The modified C-arm system, therefore, adapted a geometrical calibration method using a dedicated phantom. The phantom consisted of two plane-parallel circles of ball-bearings, encased in a cylindrical tube to ensure that the geometrical variations are fully corrected for in the 3D reconstruction algorithm.

During their experiments, the geometric calibration was conducted on a monthly basis to provide sufficient 3D image quality. However, in clinical practice, frequent calibration will add to the time and resources required which increase the system complexity. Moreover, if patient motion during imaging exists, it would not be

corrected for during reconstruction (see Sec. 3.1.4).

Image quality

The modified C-arm system employed a FBP algorithm for 3D data reconstruction (see Sec. 3.1.5). Different iDTS angles ranging from a limited arc ($\theta_{arc} \sim 10°$) to a semicircular arc equivalent to CBCT ($\theta_{arc} \sim 178°$), were used to reconstruct 3D images. Only phantoms and head cadavers were used, therefore, the effects of intraoperative anatomical deformation that might take place during surgery were not evaluated in these studies.

In the head cadaver experiments, a number of surgical localization tasks (i.e. identification of landmarks in the reconstructed 3D images), were evaluated by a number of experienced observers to determine the image quality (in terms of spatial resolution, image noise, and artefacts). Tasks included identification of both high and low contrast features [Bachar et al., 2007].

Image quality was found to be a function of the iDTS angle. Smaller acquisition angles showed reduced in-plane image quality (due to features of interest being obscured by out-of-plane structures), and a lack of out-of-plane spatial resolution. Bony anatomy provided adequate in-plane visualization for guidance down to an angle of $\theta_{arc} \sim 45°$ with minimal interference from out-of-plane structures; however, soft-tissue in-plane visualization was poor and not clinically useful below $\theta_{arc} \sim 90°$ due to clutter from high contrast features outside the slice of interest. For all angles ($\theta_{arc} < 178°$), spatial resolution was highest in-plane, whereas the out-of-plane spatial resolution showed a significant decrease as the angle was reduced. Only an angle of $\theta_{arc} \sim 178°$ (i.e. CBCT equivalent) showed adequate spatial resolution for guidance, and good soft-tissue visualization in- and out-of-plane [Bachar et al., 2009].

Bachar et al. [2007] showed that the primary cause of image degradation when using a limited iDTS arc was the out-of-plane anatomical clutter, particularly from high contrast structures outside the slice of interest. Therefore, in order to maximize the in-plane soft-tissue visualization, θ_{arc} has to be maximized. The trade-offs however, are increased acquisition time and radiation dose, and increased interruption to clinical work-flow.

Image acquisition time, reconstruction time, and radiation dose

The rotational speed of the modified C-arm was fixed at $\sim 3°$ per sec, with a fixed read-out of 3.3 fps, thus the number of acquired projection images was equal to $1.12 \times \theta_{arc}$. Image acquisition and reconstruction times, and radiation dose at the isocenter using low dose mode were all found to be approximately linear with θ_{arc}. Moreover, the smaller angle reduced both the acquisition and reconstruction times (e.g. ~ 4 times faster for a $\sim 45°$ arc compared to a $\sim 178°$ CBCT arc). Similarly, since the radiation dose per projection was fixed, the dose to isocenter was reduced in proportion to the smaller angle (e.g. ~ 4 times reduction in dose for a $\sim 45°$ iDTS compared to a $\sim 178°$ CBCT arc). The trade-off, however, is reduced image quality, especially out-of-plane spatial resolution as discussed in the image quality section.

3.2.3 iDTS for image-guided radiation therapy

In recent decades, complex EBRT techniques using linear accelerators (Linac) have been often prescribed for curative treatment of cancer.

These techniques use a planning dataset to create 3D conformal dose distributions that closely match the targeted volume contour, the aim of which is to avoid adjacent healthy structures. However, for these techniques to be effective and to improve dose delivery precision, they require better targeting accuracy.

Targeting accuracy is usually largely affected by the patient setup uncertainty, which describes the variations in positioning the patient between the day of their planning session and the day of their treatment session. Targeting inaccuracy can also result from organ motion (e.g. caused by breathing), or from tissue deformation [Baydush et al., 2005]. Employing image guidance techniques for target localization during radiation therapy (i.e. IGRT), has proven to effectively reduce daily setup variations [Reiser and Glick, 2014].

Modern Linacs often have a kilovoltage X-ray source and digital flat-panel detector mounted to the Linac's gantry. The X-ray source and detector can be used to provide image guidance during treatment by acquiring 2D radiographic images, or 3D CBCT images [Godfrey et al., 2006, 2007]. The type of image guidance

employed depends on the target's relation to bony anatomy. If bony anatomy is sufficient to localize the target, 2D radiographic imaging is used. However, if the target is likely to move or deform in relation to bony anatomy, CBCT imaging for soft-tissue visualization is required [Reiser and Glick, 2014]. The CBCT images are then registered to the planning dataset in order to determine the amount the patient has to be shifted to accurately align the desired treatment fields with the planning fields.

In EBRT, 2D image guidance is fast and involves low dose, but it does not provide adequate information for localization using soft-tissues, as soft-tissue anatomy will be obscured by over- or under-lying high contrast anatomy when projected along the ray path onto a single plane. CBCT, on the other hand, provides a true 3D image with adequate soft-tissue information.

Nevertheless, CBCT involves a relatively high dose, which will significantly add to the patient total dose for a typical four to six weeks course of external beam treatment, especially in adjacent healthy tissue areas [Baydush et al., 2005]. Therefore, acquiring a daily CBCT dataset could be impractical for patients at high risk of developing second malignancies [Wu et al., 2007]. Another issue with CBCT is the long acquisition time due to gantry speed limitations, and the need to clear the gantry path to avoid potential collisions for large patients or patients with tumors at peripheral locations (e.g. breast) [Godfrey et al., 2006]. The long acquisition time of CBCT is especially problematic for target localization in areas affected by anatomical motion (e.g. thoracic and abdominal targets), where motion artefacts can severely corrupt soft-tissue information [Godfrey et al., 2007].

iDTS was recently proposed as an alternative to CBCT to provide 3D image guidance in EBRT. Potential advantages over CBCT include: reduced scanning time since it only uses projections over a partial arc, reduced daily patient dose to healthy anatomy due to the fact that it requires significantly fewer images, and elimination of potential collision problems [Baydush et al., 2005, Godfrey et al., 2006, Wu et al., 2007, Yoo et al., 2009]. Nevertheless, the proposed iDTS technique still uses mechanical tracking of the X-ray source, and suffers from out-of-plane clutter, as was described in more detail in the previous section.

Baydush et al. [2005] examined the feasibility of using iDTS for daily patient

setup verification in radiation oncology. Rather than acquiring designated iDTS scans, a 20° subset from a CBCT dataset of one subject was used to reconstruct two iDTS images, in the coronal and sagittal views. iDTS images were reconstructed using a modified FBP technique in the view parallel to the imaging plane the rotation was centered around. In addition, and for comparison purposes with the reconstructed iDTS images, a CT dataset was acquired for the same subject. Initial results using visual inspection of the iDTS images showed increased clarity and detail of in-plane anatomy. Results showed much promise for effective daily patient positioning verification with reduced patient dose and imaging time using iDTS acquisition.

Using 3 clinical cases from prostate, abdomen, and head-and-neck patients, Godfrey et al. [2006] illustrated the potential of iDTS for IGRT target localization. Using the FBP technique, iDTS images in the coronal and sagittal views were generated using 44° subsets from the CBCT projection data available for each case. To remove respiratory motion artefacts, a breath-hold iDTS acquisition was used and compared with free-breathing iDTS acquisition for some cases. Results showed iDTS images to be similar to coincident CBCT planes, even with an eight fold reduction in acquisition time and radiation exposure compared to CBCT. In addition, iDTS fast image acquisition (< 10 sec) allowed for removal of motion artefacts with a simple breath-hold strategy, thus improving soft-tissue visibility.

Wu et al. [2007] clinically evaluated iDTS as a daily imaging technique to measure the daily patient positioning variations based on bony anatomy. 65 CBCT imaging datasets from 10 head-and-neck cancer patients were collected. Subsets from CBCT projections were then used to reconstruct iDTS images in the coronal and sagittal views, using 40° and 20° scan angles for each view. Daily patient positioning variations were retrospectively measured using the obtained iDTS images, and were compared with CBCT results. In this clinical study, iDTS with 40° and 20° scan angles produced the same results for patient positioning. Minimal differences between iDTS-based and CBCT-based methods using bony anatomy were found. Mean differences were < 1.0 mm in all translation directions, and $< 0.4°$ in any of the three rotations. These findings suggested that iDTS is a very effective method for bony head-and-neck anatomy localization, and is comparable to CBCT

for daily patient positioning. Advantages include a fraction of the exposure needed for full CBCT rotation, and reduced restrictive gantry rotation clearance and a fast scanning time (< 10 sec).

A similar clinical study was employed by Yoo et al. [2009] to evaluate iDTS as a method for daily positioning verification of patients undergoing prostate EBRT. The study, however, included an examination of soft-tissue-based patient positioning in addition to bony anatomy. A total of 92 CBCT imaging datasets from 9 prostate cancer patients were analysed, together with the reconstructed iDTS images using CBCT subsets of 45° scan angles. As in the head-and-neck study, bony anatomy positioning verification with iDTS was found to be similar to the results achieved by CBCT. However, for soft-tissue-based positioning verification, sagittal iDTS alone was insufficient for positioning verification.

Even though iDTS research regarding IGRT has mainly focused on employing the technique as an alternative to CBCT for EBRT guidance, nevertheless, iDTS has also been proposed as an alternative to fluoroscopy imaging for radioactive seed localization during prostate implants to improve preoperative dose calculation in the operating room [Reiser and Glick, 2014].

While EBRT uses a Linac to "externally" irradiate the targeted volume; brachytherapy delivers the radiation treatment "internally" at a short distance from the targeted volume. Brachytherapy involves placing small radioactive seeds (3-20 mm in length) within the treatment volume, thus, delivering a high radiation dose to the implant volume while saving adjacent healthy tissues [Persons et al., 2000]. Similar to EBRT techniques, brachytherapy is a conformal method for delivering radiation therapy to the targeted volume. Therefore, to achieve the desired brachytherapy conformal dose distribution of the treatment plan, which ensures that a therapeutic dose is delivered to the prostate gland while sparing adjacent healthy structures, it is necessary to accurately localize the implanted seeds within the treatment volume [Tutar et al., 2003].

During prostate brachytherapy procedures, an insertion needle is used to implant the seeds under ultrasound and C-arm fluoroscopy guidance according to the treatment plan. However, variations between the pre- and intra-operative implant locations can be introduced due to various reasons (for example prostate motion or

swelling) [Tutar et al., 2003].

To overcome these deviations from the treatment plan, ultrasound and fluoroscopy (being both readily used for seed implantation guidance) were proposed for intraoperative correction of the preoperative treatment plan. However, methods for seed localization from a limited number of X-ray images require accurate segmentation and identification of each seed in each X-ray projection image. Identifying all implanted seeds (especially when seeds are completely overlapping) is difficult even when sophisticated segmentation and labelling methods are employed. Unidentified seeds are usually recovered manually, which interrupt the clinical work-flow, and sometimes requires extra X-ray images. Moreover, hidden seeds in X-ray images (up to 7%) are sometimes impossible to recover [Lee et al., 2008].

In contrast to projection-based seed localization methods, Tutar et al. [2003] developed a novel iDTS-based brachytherapy specific seed localization technique. The method allows automatic segmentation and localization of seeds in the iDTS reconstruction volume even when seeds are completely overlapping. Using only 7 projections over a 30° scan angle in a preliminary study, all 61 radiographically visible dummy seeds implanted inside a tissue-equivalent ultrasound phantom were successfully localized. However, as reported by Lee et al. [2008], if C-arm positional imprecision or calibration errors exist (especially when using portable C-arm systems), the method could miss locating true seeds.

In order to make iDTS-based seed localization more robust to potential positional and calibration errors of the C-arm, Lee et al. [2008] proposed using a fluoroscopy tracking fiducial (which creates a unique projection image from any direction) to estimate the C-arm position at each image. In an initial clinical trial using 2 patient datasets, all 61 and 66 seeds implanted into the prostate were successfully localized, using as few as 3 projection images acquired over a 10° scan angle centered about the AP direction. However, this method requires the specific fluoroscopy tracking fiducial to be available and attached to the needle insertion template, which can be cumbersome.

3.3 2D-3D Image Registration for Advanced Fluoroscopy Guidance

As discussed in Sec. 2.3.1, vasculature is not well visualized using standard low dose fluoroscopy imaging (i.e. fluoroscopy screening). This is because the difference in attenuation coefficients between blood and surrounding soft-tissues is very small.

In the following, I give a brief description of 2D-3D image registration, which is the main technique developed to provide advanced vascular imaging guidance during interventional fluoroscopy. I highlight the difference between registration methods based on the nature of the registration basis (i.e. extrinsic or intrinsic), and based on geometric transformation (i.e. rigid or non-rigid) [Markelj et al., 2012]. I also discuss the main limitation of rigid registration methods: intraoperative deformation.

3.3.1 Overview

The aim of 2D-3D image registration is to calculate the transformation between the 3D preoperative data coordinate system and the 2D intraoperative data coordinate system to aid guidance during an intervention (See Sec. 2.4.2).

In the case of EIGS, the preoperative data is usually an angiography CT volume, and the intraoperative data is usually fluoroscopy images. Once the transformation is calculated, a 3D rendering of the CT vasculature can be overlaid onto the 2D fluoroscopy images to help provide surgeons with real-time information about the current position of interventional devices relative to the preoperative spatial vasculature (as shown in Fig. 2.7 in Sec. 2.4.2 using an overly of the aorta).

3.3.2 Extrinsic Vs. intrinsic 2D-3D registration

Based on the type of features used to achieve dimensional correspondence, 2D-3D registration techniques can be classified into extrinsic and intrinsic methods [Markelj et al., 2012]:

Extrinsic methods use artificial structures (e.g. spherical markers), which are designed to be well visualized in both the 3D and 2D images.

Using extrinsic markers for registration is accurate and fast due to the limited

number of markers. However, it is inconvenient and invasive to the patient as the most accurate methods require surgery to implant the markers. Therefore, marker-based registrations are often only used to validate other registration methods because of their accuracy.

Intrinsic methods use anatomical structures for registration. They can be classified into two main types: feature-based and intensity-based.

Feature-based methods compare extracted features from both the 3D and 2D images for registration, which makes the algorithms fast because the amount of processed data is substantially reduced. However, the registration accuracy of feature-based algorithms depends directly on the segmentation accuracy. Moreover, accurate and automated feature extraction from complex interventional fluoroscopy images is very hard to achieve and errors can lead to misregistration. Intensity-based methods, on the other hand, compare the voxels and pixels values in the 3D and 2D data respectively, for registration. This typically makes the registration algorithms slower but no feature extraction is required.

3.3.3 Rigid Vs. non-rigid 2D-3D registration

Based on the nature of the spatial transformation, and its degrees of freedom, 2D-3D registration can be classified as rigid and non-rigid.

A large number of rigid 2D-3D registration methods have been proposed in the literature, compared to only a small number of non-rigid methods. This is because 2D-3D registration is by itself difficult (see Markelj et al. [2012] for a recent survey).

Rigid registration is generally applied when it is assumed that no spatial distortion of the targeted anatomy has occurred between the pre- and intra-operative images (i.e. images are assumed to achieve correspondence simply by rotating and/or translating one image with respect to the other) [Crum et al., 2004].

Figure 3.3 shows the ten degrees of freedom involved in rigid 2D-3D perspective projection transformation, which are also shown in Eqn. 3.1:

$$W = (c_s, l_s, k_1, k_2, \theta_x, \theta_y, \theta_z, X, Y, Z) \tag{3.1}$$

c_s and l_s are the 2D position on the imaging plane where the normal to the imaging plane goes through the X-ray source (which will be referred to as the

X-ray piercing point in this thesis). k_1 and k_2 are equal to the source to image distance (SID) divided by the image pixel sizes in the horizontal (u_{pix}) and vertical (v_{pix}) directions respectively (i.e. $k_1 = SID/u_{pix}$, $k_2 = SID/v_{pix}$). θ_x, θ_y, and θ_z represent the orientation, and X, Y, and Z represent the position of the CT coordinate system with respect to the fluoroscopy set coordinate system.

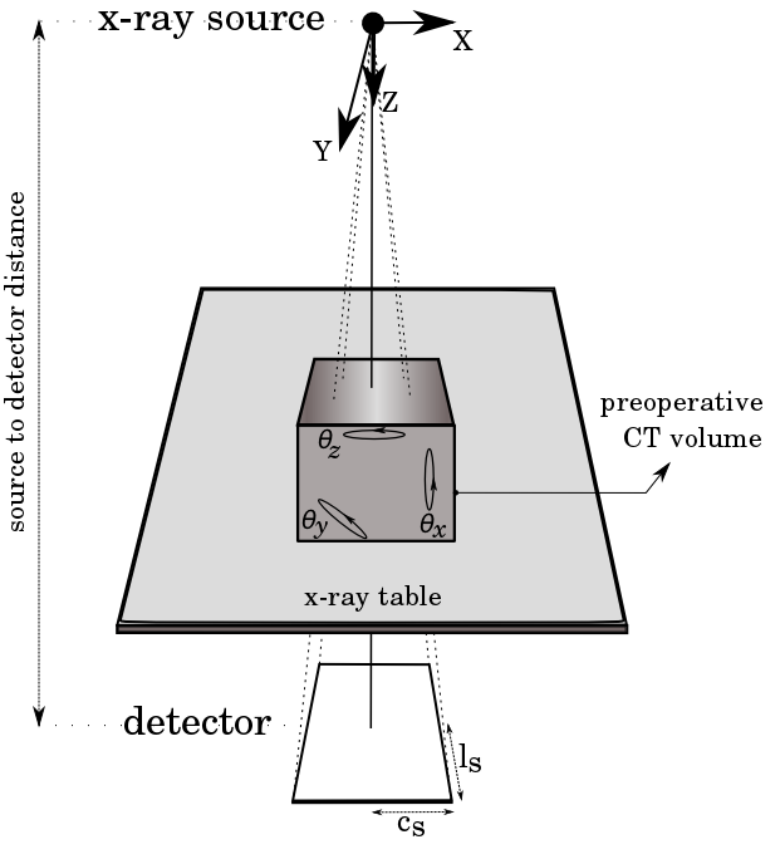

Figure 3.3: The ten degrees of freedom in rigid body perspective projection. c_s and l_s are the positions on the imaging plane where the normal goes through the X-ray source. k_1 and k_2 are the source to image distance divided by the image pixel sizes. θ_X, θ_Y, and θ_Z represent the imaged object orientation, while X, Y, and Z represent its position with respect to the fluoroscopy set coordinate system.

These parameters can be split into two sets of parameters:

- Intrinsic parameters $W_I = (c_s, l_s, k_1, k_2)$, which define the perspective projection geometry.
- Extrinsic parameters $W_E = (\theta_x, \theta_y, \theta_z, X, Y, Z)$, which determine the position and orientation of the imaged object.

Extrinsic parameters are either in-plane or out-of-plane. These terms are defined as follows:

- An in-plane translation is parallel to the imaging plane (i.e. X, Y), whereas; an out-of- plane translation is perpendicular to the imaging plane (i.e. Z).
- An in-plane rotation is about an axis perpendicular to the imaging plane (i.e. θ_z), while; an out-of-plane rotation is about an axis parallel to the imaging plane (i.e. θ_x, θ_y).

Intrinsic and extrinsic parameters can be combined to produce a projection transformation matrix $M(W)$, which is the product of three matrices (all represented as homogeneous coordinates): a 3×4 perspective matrix $P(c_s, l_s, k_1, k_2)$, a 4×4 rotational matrix $R(\theta_x, \theta_y, \theta_z)$, and a 4×4 translation matrix $T(X, Y, Z)$, as shown in Eqn. 3.2:

$$M(W) = P(c_s, l_s, k_1, k_2)R(\theta_x, \theta_y, \theta_z)T(X, Y, Z) \tag{3.2}$$

Matrix $M(W)$ is used to relate positions between the CT and the fluoroscopy image coordinate systems.

Non-rigid registration is employed when it is assumed that spatial distortion of the targeted anatomy has occurred between the pre- and intra-operative images (i.e. images are assumed to achieve correspondence by some localized stretching) [Crum et al., 2004].

Non-rigid registration has several clinical applications (e.g. correction of intra-operative deformation during IGS), nevertheless, developing non-rigid techniques is a challenging area of registration research as reported by Crum et al. [2004].

Crum et al. [2004] concluded that the two main challenges facing non-rigid registration are the computational cost, and the difficulties in validating the results. Their paper reported that non-rigid algorithms frequently take several hours to calculate the required transformation between images. In addition, post-registration measurements are usually required for validation. Similarly, Markelj et al. [2012] reported that extending the rigid registration approaches into non-rigid remains one of the most clear challenges facing 2D-3D registration.

3.3.4 Main limitation: deformation

As described in Sec. 2.4.2, the main limitation of rigid 2D-3D registration for EIGS, is the non-rigid intraoperative deformation of vasculature caused by the introduction of stiff interventional devices, which decreases the accuracy of any guidance in the deformed region [Carrell et al., 2010, Sailer et al., 2014].

Carrell et al. [2010] showed that the main source of errors in the employed rigid 2D-3D registration was aortic deformation caused by the presence of the delivery-system and stent-graft. In their paper, registration errors ≤ 3 mm were considered clinically acceptable (based on an average 6 mm diameter of a renal artery ostium). The paper found a strong correlation between the aortic neck angulation (see Fig. 2.9) and registration error. A clinically acceptable mean error of 2.56 mm was reported for aortas with a neck angulation $\leq 30°$. However, the rigid registration failed to give clinically acceptable errors when used in highly angulated aortas (mean error of 6.26 mm for aortas with neck angulation $> 30°$). These findings were explained by the fact that the delivery-system and stent-graft have limited flexibility and can exert large forces that cause the aorta to be straightened. Therefore, highly angulated aortas experience high degrees of aortic deformation resulting in clinically significant errors. Nevertheless, as mentioned in Sec. 2.5, complex aneurysms with highly angulated aortic necks benefit the most from EIGS.

Intraoperative soft-tissue deformation is a common problem for any method that employs rigid image registration of a preoperative anatomy. Non-rigid registration is required to address this problem. However, non-rigid registration methods to deform the preoperative vasculature to match the intraoperative scene during EIGS are still under investigation (e.g. Groher et al. [2010], Guyot et al. [2013], Liao et al. [2010], Raheem et al. [2010]).

3.4 Conclusions

This chapter described how iDTS has been proposed as an alternative to CBCT during IGRT and IGS procedures. The presented literature has shown the potential advantages of iDTS over CBCT which include: reduced scanning time and patient dose, and much less interruption to the clinical work-flow. Nevertheless, all

proposed methods still use mechanical tracking of the X-ray source which requires frequent geometrical calibration. Out-of-plane clutter is also still the main problem. Moreover, while proposed methods employ iDTS to reconstruct 3D images during IGRT and IGS procedures, surgeons during EIGS interventions view 2D images displayed on the interventional screens to guide their instruments through vasculature. Therefore, 3D iDTS images would require some interaction to find the clinically relevant information to be displayed which could cause an interruption to the clinical work-flow.

In addition, this chapter also described how 2D-3D image registration has been developed to provide advanced guidance during EIGS using fluoroscopy. However, the main limitation of rigid registration techniques is the non-rigid intraoperative deformation of vasculature. Developing non-rigid techniques is still a challenging area of registration research.

Employing rigid 2D-3D image registration to facilitate iDTS on a standard fluoroscopy system has not yet been proposed. This is the main aim of my thesis. Moreover, I aim to reconstruct patient-anatomy-specific 2D images with much reduced clutter to aid EIGS interventions. As these images are acquired intraoperatively, deformation will not be an issue, and they will show the intraoperative anatomy complete with any deformation.

Chapter 4

iDTS Facilitated by 2D-3D Registration on a Standard Fluoroscopy System

Contents

4.1 Introduction

As stated in the clinical background chapter, the primary modality used for EIGS is C-arm fluoroscopy. However, a major disadvantage of fluoroscopy is the inadequate soft-tissue visualization, thus the injection of ICM is required to enhance visualization of vasculature. Nevertheless, ICM is nephrotoxic and imaging during ICM injection was reported to contribute 81% to the patient radiation dose (see Sec. 2.4.1). Using the same C-arm platform, CBCT can acquire 3D images with better soft-tissue visualization than fluoroscopy. However, CBCT greatly affects the clinical work-flow, and involves much higher radiation exposure than fluoroscopy (see Sec. 2.3.2).

Complex EIGS procedures (where large volumes of ICM are used compared to standard procedures) could benefit greatly from novel techniques that offer better vascular visualization with reduced ICM usage and radiation exposure, but still maintain the clinical work-flow.

As explained in the literature review chapter, rigid 2D-3D image registration has been the main technique developed to improve EIGS by providing 3D preoperative overlays during procedures (see Sec. 3.3). However, current registration techniques cannot cope with non-rigid intraoperative vascular deformation in complex cases where it could be very beneficial (see Sec. 3.3.4). Moreover, the literature review also showed the potential advantages of iDTS over CBCT during IGRT and IGS procedures. Nevertheless, all proposed iDTS methods still employ the same technique used in diagnostic DTS systems (mechanical tracking of the X-ray source), and still suffer from out-of-plane clutter.

This chapter and the following experimental chapter (Ch. 5) are based on the work presented in Alhrishy et al. [2013], which was extended and submitted as a journal paper [Alhrishy et al., 2015a]. In this chapter, I propose employing an established 2D-3D rigid registration system to facilitate improved iDTS reconstruction using standard hardware during complex EIGS interventions. The proposed methods can automatically enhance specific clinical structures and can reduce out-of-plane clutter. The chapter begins by defining three coordinate systems to describe the 2D-3D registration geometry. An overview of the specific 2D-3D registration algorithm I use is then given. Finally, I give a detailed description of how the

registration algorithm enables patient-anatomy-specific iDTS reconstruction, with greatly reduced out-of-plane clutter, using images from a standard fluoroscopy system.

4.2 Coordinate Systems Definition

I define three coordinate systems which are going to be used throughout this thesis as shown in Fig. 4.1. The first two coordinate systems are related to the fluoroscopy machine; whereas the third is related to the preoperative CT volume as listed below.

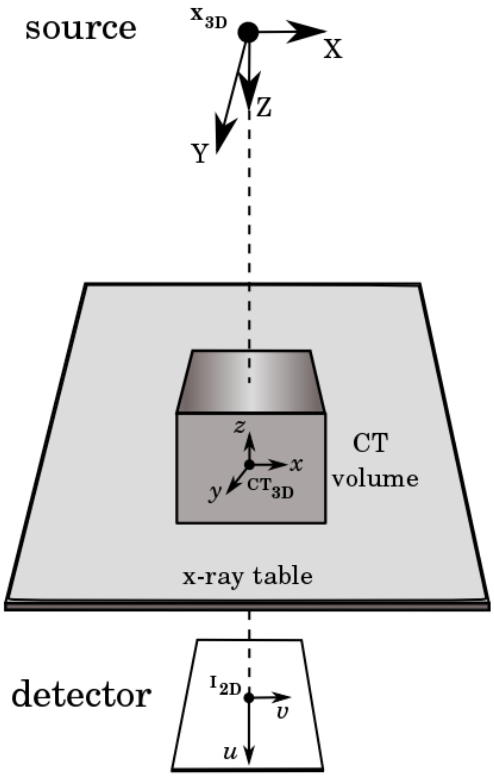

Figure 4.1: The 2D-3D registration geometry with the three defined coordinate systems: 1) $\mathbf{X}_{3D}$ for the 3D X-ray fluoroscopy machine, 2) $\mathbf{I}_{2D}$ for the 2D X-ray image, and 3) $\mathbf{CT}_{3D}$ for the 3D preoperative CT scan.

1. $\mathbf{X}_{3D}$: the 3D X-ray fluoroscopy machine coordinate system. This defines 3D positions with respect to the X-ray source. Coordinates in $\mathbf{X}_{3D}$ are denoted using the capital letters (X, Y, Z).

2. $\mathbf{I}_{2D}$: the 2D X-ray image coordinate system. This defines 2D positions in the X-ray image. Coordinates in $\mathbf{I}_{2D}$ are denoted by (u, v).

3. $\mathbf{CT}_{3D}$: the 3D preoperative CT scan coordinate system. This defines 3D positions in the preoperative CT scan. Coordinates in $\mathbf{CT}_{3D}$ are denoted using the small letters (x, y, z).

Using the defined coordinate systems, matrix $M(W)$ in Eqn. 3.2 can be said to relate positions (represented as homogeneous coordinates) between $\mathbf{CT}_{3D}$ and $\mathbf{I}_{2D}$, as shown in Eqn. 4.1, where λ is a scaling factor:

$$M(W)(x, y, z, 1)^T = \lambda(u, v, 1)^T \tag{4.1}$$

Alternatively, this can be expressed by using the 3×4 perspective matrix (P), the 4×4 rotational matrix (R), and the 4×4 translational matrix (T) such as:

$$PRT(x, y, z, 1)^T = \lambda(u, v, 1)^T \tag{4.2}$$

Matrix $M(W)$ can be used to project a 3D point in $\mathbf{CT}_{3D}$ onto a 2D point in $\mathbf{I}_{2D}$, or to transform a 2D point in $\mathbf{I}_{2D}$ onto a 3D line in $\mathbf{CT}_{3D}$.

4.3 Description of the 2D-3D Registration Algorithm

A large number of 2D-3D registration algorithms have been proposed in the literature for IGS [Markelj et al., 2012]. My methods use an established rigid registration algorithm, which was described and validated by Penney et al. [1998, 2011]. The novelty of this work lies in the use of this registration system to facilitate improved iDTS for image guidance during endovascular procedures, using standard hardware.

This registration system has been regularly used for elective EVAR cases at St Thomas' hospital (London, UK), as part of a clinical trial (National Research Ethics Service approval 09/H0707/64). The system aligns $\mathbf{CT}_{3D}$ with $\mathbf{X}_{3D}$ during interventions as was illustrated in Fig. 3.3.

The employed algorithm is intensity-based and uses a single vertebra from the preoperative CT volume to generate a digitally reconstructed radiograph (DRR) image (different vertebra can be used for registration depending on the region of interest (ROI)). The DRR image is then compared with the fluoroscopy image

using a gradient difference similarity measure. In the following, I briefly describe how the algorithm produces a DRR, the way the gradient difference measure works, and the strategy used for registration (detailed description can be found in Penney et al. [1998]). I also show how the registration system displays the results to the interventional team, and allows them to request some operations to be performed.

4.3.1 Production of digitally reconstructed radiographs (DRRs)

DRRs are reconstructed by casting rays through an automatically segmented single vertebra from the preoperative CT volume (by defining a rough bounding box around the vertebra). Each of these rays will go through a number of voxels. If the Hounsfield units (HUs) of these voxels are above a chosen threshold (200 HU), their values are integrated along each ray and projected onto an imaging plane. The threshold value is chosen experimentally to remove soft-tissue, but to leave as much bony detail as possible in the produced DRRs, therefore, DRR intensities should only include voxel values from vertebral bone.

The reason that DRRs are produced from only one segmented vertebra is to reduce the effect of vertebral column deformation, which occurs when the relative positions of the vertebrae are different between the CT and fluoroscopy images. Using a single rigid structure, such as one vertebra, reduces the effect of such deformation on the registration. In addition, the thresholding process makes sure that the registration will be only based on vertebral bone, and therefore, soft-tissue deformation is not an issue.

The resultant DRR image should resemble a radiograph, or if the intensities are inverted a fluoroscopy image. Figure 4.2 shows a DRR produced from a segmented L3 vertebra of a patient undergoing EVAR which resembles, if inverted, the fluoroscopy image of the same vertebra. However, differences still exist between the produced DRRs and the fluoroscopy images due to differences in the imaging modality and image formation. The algorithm tries to maximise the resemblance by a number of additional steps (see Penney et al. [1998] for more details).

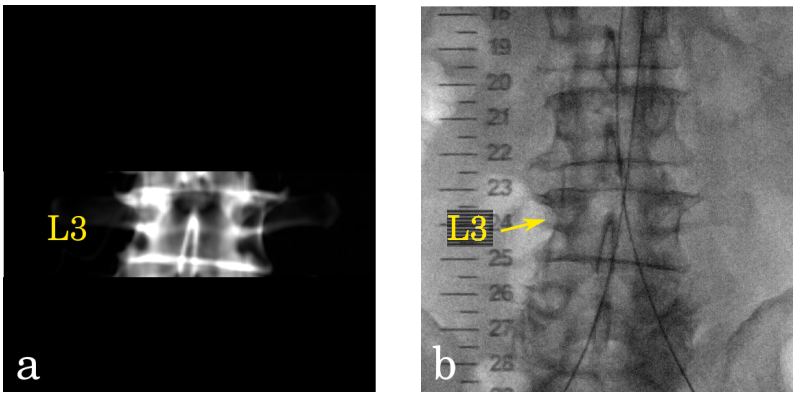

Figure 4.2: a) Digitally reconstructed radiograph (DRR) of an automatically segmented L3 vertebra from the preoperative CT volume of a patient undergoing EVAR. b) Fluoroscopy image of the same patient for the abdominal region with the L3 vertebra indicated.

4.3.2 Gradient difference similarity measure

The gradient difference similarity measure (G) is used to compare intensities in the produced DRR image $I_{DRR}(u, v)$, to intensities in the fluoroscopy image $I_{fl}(u, v)$, where (u, v) defines the location of a pixel to be in the column u and row v.

G is defined by Eqns. 4.3 & 4.4 as below:

$$G(s_V, s_H) = \sum_{u,v} \frac{A_V}{A_V + (I_{diffV}(u, v))^2} + \sum_{u,v} \frac{A_H}{A_H + (I_{diffH}(u, v))^2} \tag{4.3}$$

$$I_{diffV}(u, v) = \frac{\partial I_{fl}}{\partial u} - s_V \frac{\partial I_{DRR}}{\partial u}; \quad I_{diffH}(u, v) = \frac{\partial I_{fl}}{\partial v} - s_H \frac{\partial I_{DRR}}{\partial v} \tag{4.4}$$

Four gradient images: $\frac{\partial I_{fl}}{\partial u}$, $\frac{\partial I_{DRR}}{\partial u}$, $\frac{\partial I_{fl}}{\partial v}$, and $\frac{\partial I_{DRR}}{\partial v}$ are first created by applying horizontal (H) and vertical (V) Sobel templates over the I_{DRR} and I_{fl} images.

The vertical and horizontal gradient difference images I_{diffV} and I_{diffH}, respectively, are then calculated as in Eqn. 4.4, using the scaling factors s_V and s_H, which account for the differences between the produced DRR and the fluoroscopy image. The values of s_V and s_H are initially set to zero, and are then individually increased

by uniform steps until the maximum value of G is found. The step size is chosen to be equal to the ratio of the intensity ranges in both images divided by 100.

In Eqn. 4.3, A_V and A_H are constants, that are set to the variance of the pixel intensities in the respective (vertical and horizontal) gradient fluoroscopy images.

Using spine phantom images with features segmented from clinical fluoroscopy images overlaid, Penney et al. [1998] showed that the gradient difference similarity measure was able to register accurately and robustly, with no failures, even with the presence of soft-tissue structures and interventional instruments in the fluoroscopy image. The registration accuracy for all extrinsic parameters (except for Z) was found to be less than 0.5 mm or degrees (∼6.7 mm for Z), compared to accurate "gold-standard" registration values.

4.3.3 Registration strategy

When an image is acquired, several parameters are recorded in the DICOM header from the fluoroscopy system. The registration algorithm takes advantage of some of the image information available in the DICOM header (FoV, number of rows and columns, and SID) to calculate the four intrinsic parameter values (c_s, l_s, k_1, k_2), assuming that the X-ray piercing point is at the centre of the FoV. In addition, rotations of the C-arm (right/left-anterior-oblique (RAO/LAO) and cranial-caudal (CC) angulations), which are also provided in the DICOM header, are used to initialize the starting positions of the out-of-plane rotations (θ_x, θ_y).

Next, the starting positions of the in-plane translations (X, Y) are acquired using a graphical user interface, which shows the fluoroscopy image and the segmented CT vertebra surface on which the registration is based (e.g. L3 vertebra in Fig. 4.3.a). Using visual inspection, the user defines the corresponding vertebra in the fluoroscopy image by picking four points around the region of interest (yellow box in 'b'). Finally, the CT vertebra surface is manually translated inside the defined box and over the fluoroscopy vertebra to complete the process as seen in 'c'. The full process takes approximately twenty seconds.

The starting positions of the remaining extrinsic parameters (θ_z, Z) are provided manually ($\theta_z = 0$, and $Z = 800$mm), so that each extrinsic parameter would have a starting value.

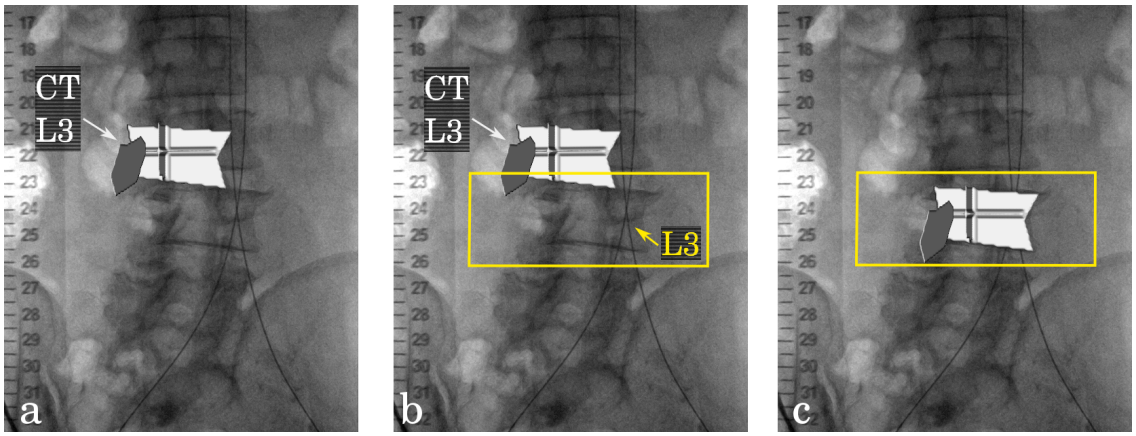

Figure 4.3: Defining the starting positions for the in-plane translation parameters using a graphical user interface. a) The fluoroscopy image and the segmented CT L3 vertebra surface. b) The corresponding L3 vertebra is visually identified in the fluoroscopy image, and a box is drawn around the chosen vertebra (yellow box). c) The CT vertebra surface is manually translated over the fluoroscopy vertebra and inside the yellow box to complete the process.

Using the acquired W_I values and the initial values for W_E, the algorithm produces a DRR which is compared to the fluoroscopy image to obtain the initial value of the similarity measure. The extrinsic parameters are then altered, one at a time, and a new DRR is produced at each new position in order to optimize the similarity measure (see Penney et al. [1998] for more details about the search strategy and optimisation process).

When the registration position is reached, the algorithm outputs the final W_E, which are used together with the acquired W_I to accurately position the CT volume with respect to $\mathbf{X}_{3D}$. Positions between $\mathbf{CT}_{3D}$ and $\mathbf{I}_{2D}$ can be then related using the transformation matrix $M(W)$ as in Eqn. 4.1.

4.3.4 Displaying the registration output

The system uses the final registration position to overlay a surface rendering of the aorta lumen and visceral vessels onto the current fluoroscopy image as shown in Fig. 4.4.a. The aorta and visceral vessels are produced from the CT volume using the semi-automatic segmentation option available in ITK-SNAP [Yushkevich et al., 2006].

The overlay is directly displayed to clinicians using one of the available screens in the interventional room. The system allows clinicians to request: fading in and out the surface overlay, rotating the surface to provide some 3D information (as in 'b' and 'c' views), picking a point on the surface to be back projected onto the fluoroscopy image (red point in 'b'), and picking a point on the fluoroscopy image to be projected onto a line through the surface (white line in 'c').

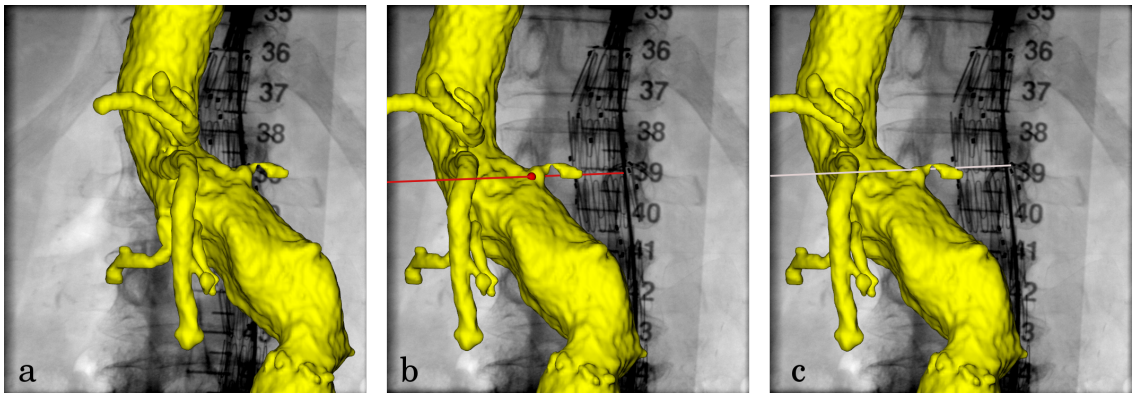

Figure 4.4: a) Overlaying a surface rendering of the CT aorta lumen and visceral vessels onto the fluoroscopy image using the registration final position. The surface can be rotated to provide some 3D information as seen in 'b' and 'c'. In addition, in b), a point on the surface is picked (red point) to be projected onto the fluoroscopy image; whereas in c), a point on the fluoroscopy image is picked to be back projected onto a line through the surface (white line).

Figure 4.4.a, where the surface has not yet been moved (rotated and/or translated) from its registration position, clearly demonstrates the intraoperative deformation of the aorta, which is caused by the interventional devices. Figure 4.5 illustrates this more clearly using the same images. The labelled devices in the fluoroscopy image 'a' have been highlighted in white color in the overlay image 'b', as follows: dashed line for the stiff-wire, and solid line for the edges of the stent-graft. The stiff-wire (dashed white line) has straightened the aorta causing large misalignment between the edges of the stent-graft (solid white line) and the edges of the aorta overlay, which decreases the accuracy of any guidance in the deformed region (as described in Sec. 2.4.2).

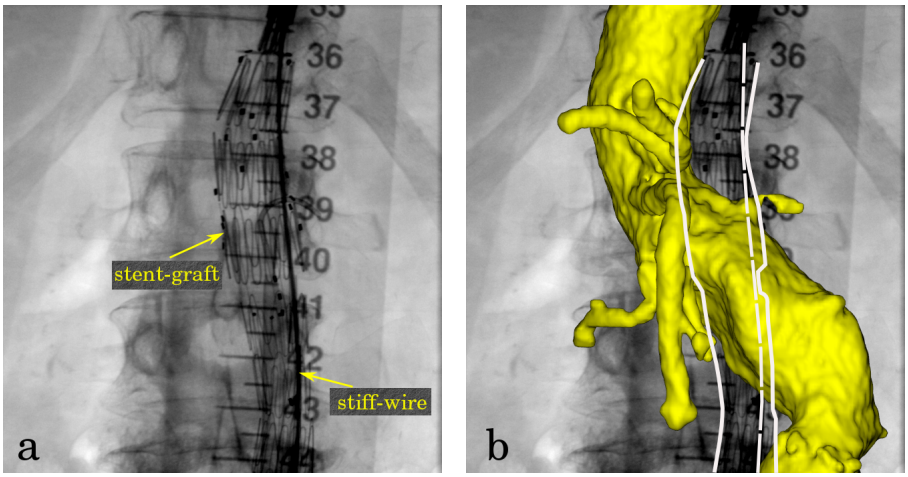

Figure 4.5: Demonstrating the intraoperative deformation of the aorta caused by interventional devices. a) The fluoroscopy image with a stiff-wire and stent-graft present. b) The overlay image with the stiff-wire highlighted as a white dashed line, and the stent-graft edges highlighted as a white solid line. The stiff-wire (dashed line) has deformed the aorta causing misalignment between the edges of the stent-graft (solid line) and the edges of the aorta overlay.

4.4 iDTS Using 2D-3D Registration

The novelty of this method lies in the use of the aforementioned 2D-3D registration system to facilitate improved iDTS reconstruction using standard fluoroscopy hardware, on patient-anatomy-specific surfaces and with reduced out-of-plane clutter. In the following, I detail how this can be achieved.

4.4.1 Using the 2D-3D registration algorithm to facilitate enhanced iDTS

Figure 4.6 shows the three ways in which the 2D-3D registration algorithm both enables and improves iDTS. This begins at the top with the input images: a) a small angle C-arm sweep to produce b) a set of intraoperative fluoroscopy images: $I_{fl_1}, \ldots, I_{fl_n}$, and c) a preoperative CT scan. These images are input into the 2D-3D registration algorithm which calculates 'sequentially' the transformation matrices, M_i, between the CT scan and each of the n fluoroscopy images i.e.:

$$M_i(x, y, z, 1)^T = \lambda(u, v, 1)_i^T \qquad , i = 1, \ldots, n \tag{4.5}$$

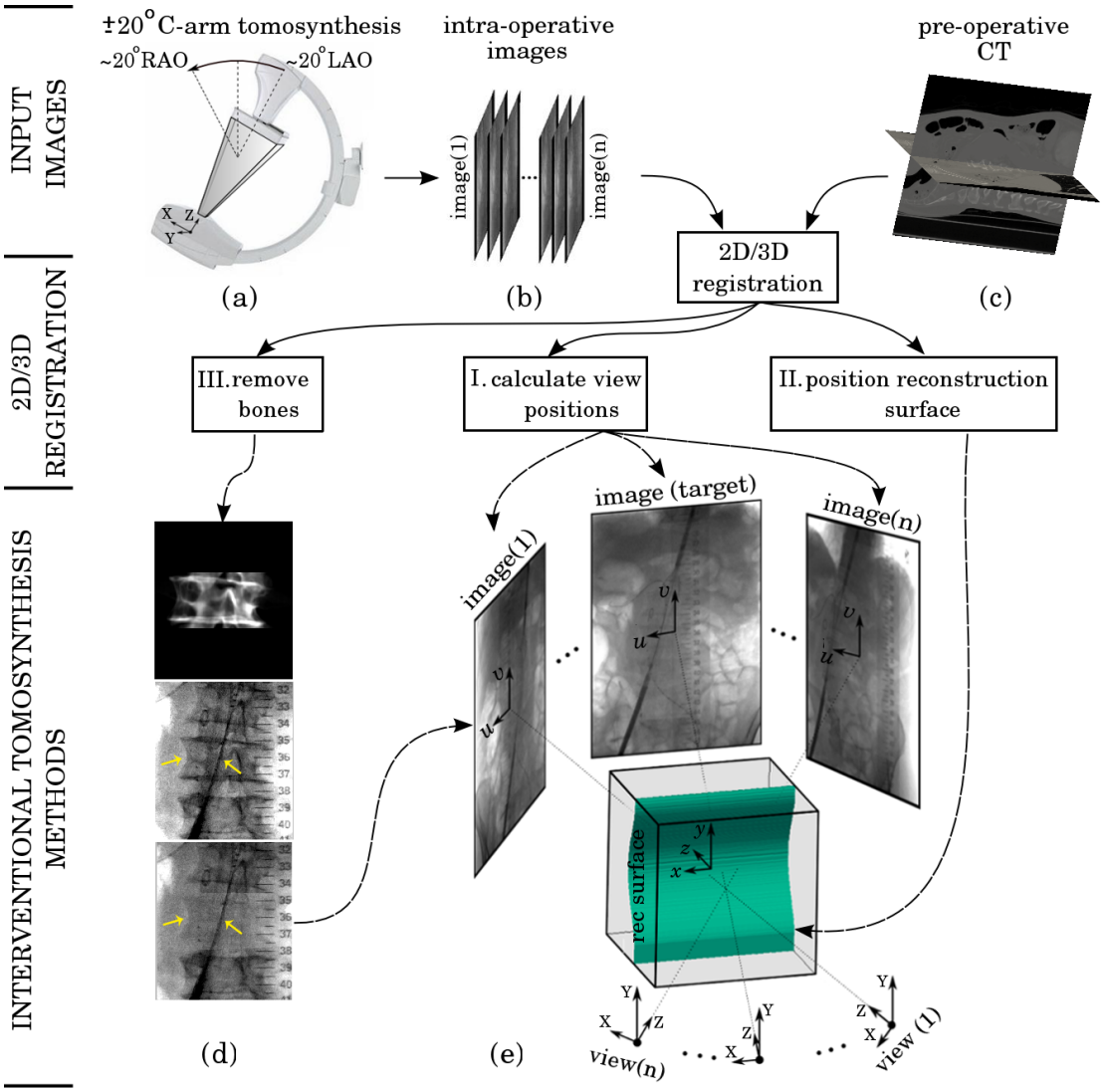

Figure 4.6: Flow diagram showing how the 2D-3D registration algorithm enables and improves iDTS. Top shows input images: a) a small angle C-arm sweep to produce b) intraoperative fluoroscopy images, and c) the preoperative CT volume. Middle and bottom show the 2D-3D registration which enables d) bone removal, and e) calculation of view directions and positioning of curved patient-anatomy-specific reconstruction surface.

Only the imaging parameters of I_{fl_1} are saved in the DICOM header, as images are acquired during a single motion of the C-arm (i.e. not stop and shoot). The information available in the I_{fl_1} header is used to specify the starting position for the first registration as was described in Sec. 4.3.3. The first registration output (PR_1T_1) is then used as a starting position for the second registration and so on, in a sequential order. This works robustly because the distance between any two

consecutive C-arm positions is within the search range of the registration algorithm.

The registrations provide the necessary information to carry out iDTS (as was described for standard DTS in Sec. 3.1.4), and enables a great reduction of clutter from bone. This is illustrated by the three boxes showing the subsequent stages to the 2D-3D registration in Fig. 4.6, where the Roman numerals labelling each box correspond to the following stages.

I. **Calculate view positions** of all input fluoroscopy images.

II. **Position reconstruction surface** with respect to any of the fluoroscopy images.

III. **Remove bones** from the fluoroscopy images prior to iDTS image reconstruction.

In the following, I describe in more detail the subsequent stages to the 2D-3D registration in the same order.

I. Calculate view positions

During the C-arm sweep, the extrinsic parameters (W_E, see Sec. 3.3.3) change depending on the current C-arm view position. The transformations $M_i = PR_iT_i$ can be used to determine the view positions of all input 2D images with respect to $\mathbf{CT}_{3D}$. Figure 4.7 shows an example of how θ_z values change with a C-arm sweep of approximatively 40° (from 20.07° LAO to 20.70° RAO). During the sweep, 114 fluoroscopy images of a phantom were acquired (the phantom experiment will be described fully in Sec. 5.2.1).

II. Position reconstruction surface

A patient-anatomy-specific plane can be preoperatively defined inside the CT scan. The transformations M_i can position this plane with respect to any of the fluoroscopy images, enabling reconstruction to occur on a patient-anatomy-specific plane.

In addition, I propose the use of curved patient-anatomy-specific reconstruction surfaces. It is rare that structures of clinical interest lie on flat planes. My aim

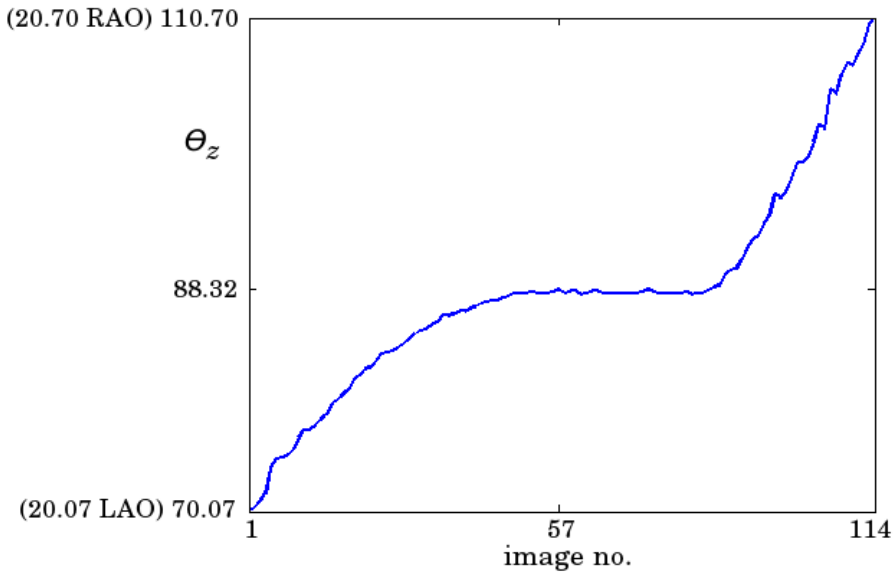

Figure 4.7: An example of how θ_z values change with a C-arm sweep of approximately 40°. 114 fluoroscopy images of a phantom were acquired as the C-arm rotated around the imaged object from 77.07° to 110.70°.

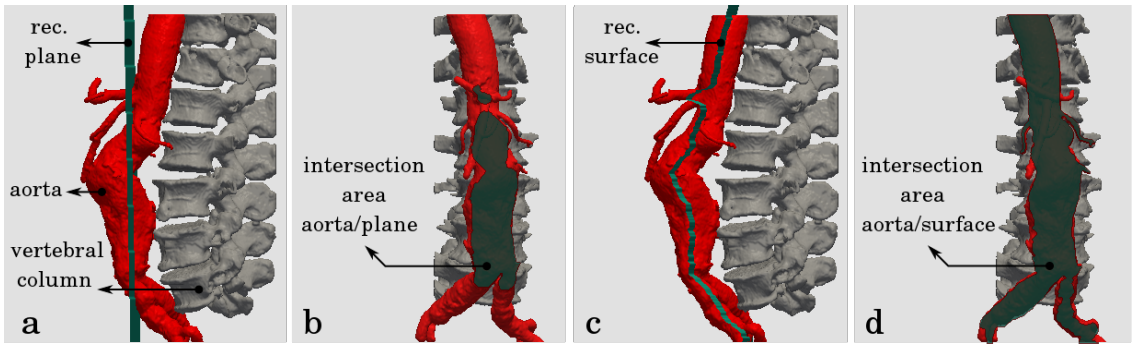

Figure 4.8: Illustration of the advantage of using a curved surface over a flat plane for iDTS reconstruction, where the aorta is the feature of clinical interest. a,c) Sagittal views showing a) a flat reconstruction plane intersecting the aorta, and c) a curved reconstruction surface along the aortic centreline. b,d) Anterior views showing b) a flat plane only intersecting with roughly half of the aorta, and d) a curved surface intersecting (and therefore can reconstruct) the entire aorta.

in iDTS is to produce 2D images with enhanced clinically relevant structures. As shown in Fig. 4.8, if the structure of clinical interest is the aorta, then only approximately half of its length could be included in a flat reconstruction plane ('a' and 'b'), whereas the use of a curved surface allows reconstruction of the entire length of the aorta ('c' and 'd').

III. Remove bones

High attenuation bony features are the largest cause of out-of-plane clutter, and will greatly reduce iDTS image quality (see Sec. 3.1.5). However, because the 2D-3D algorithm accurately registers a single vertebra between the CT and fluoroscopy images (see Sec. 4.3.1), I am able to subtract fluoroscopy intensities arising due to the vertebra, prior to iDTS image reconstruction. This has the potential to greatly reduce the effect of out-of-plane clutter from vertebral features.

My method uses the produced DRR at the current registration position for bone removal, which I call "deboning". Because a DRR is produced from an automatically segmented single vertebra from the preoperative CT (by defining a rough bounding box, and by only integrating HUs above 200), the DRR should contain only information from the CT vertebra.

The DRR vertebra intensities have an approximately linear relationship to the fluoroscopy vertebra intensities, thus a suitable scaling factor (s) should be included in the difference image I_{diff}, as in Eqn. 4.6, where $I_{fl}(u,v)$ and $I_{DRR}(u,v)$ are the fluoroscopy and DRR image intensities, respectively:

$$I_{diff}(u,v) = I_{fl}(u,v) - s \times I_{DRR}(u,v) \tag{4.6}$$

To determine the optimal scaling value s, I begin with a value of zero then increase s in fixed steps until a maximum value of the chosen similarity measure is found. The size of the step is chosen to be equal to the ratio of the maximum intensities in the two images divided by 50.

The pattern intensity similarity measure [Weese et al., 1997] is chosen to optimise the scaling factor because of its known robustness to differences between the two images, such as interventional devices, which introduce large differences in pixel intensity to a small number of pixels.

The pattern intensity operates on the difference image by using a circular mask of a fixed radius r. The mask is moved over I_{diff}, and at each position, the value of the central pixel under the mask (u,v) is compared to all the other pixels under the mask (i,j), as described in Eqns. 4.7 and 4.8, where the values of σ and r are 10 and 3, respectively, as per Weese et al. [1997]:

$$P_{r,\sigma}(s) = \sum_{u,v} \sum_{d^2 \leq r^2} \frac{\sigma^2}{\sigma^2 + (I_{diff}(u,v) - I_{diff}(i,j))^2} \tag{4.7}$$

$$d^2 = (u-i)^2 + (v-j)^2 \tag{4.8}$$

High pattern intensity values are achieved when I_{diff} has few features (i.e. pixel values in I_{diff} are very similar). This will occur when the value of s removes as many of the vertebral features as possible.

An example of removing a vertebra, such as L3, is shown in Fig. 4.9, where the produced DRR at the registration position 'a', is subtracted from a ROI around L3 in the fluoroscopy image 'b'. Features from the L3 vertebra can be seen to have been almost completely removed in 'c', leaving non-vertebra features (i.e. guide-wires) present.

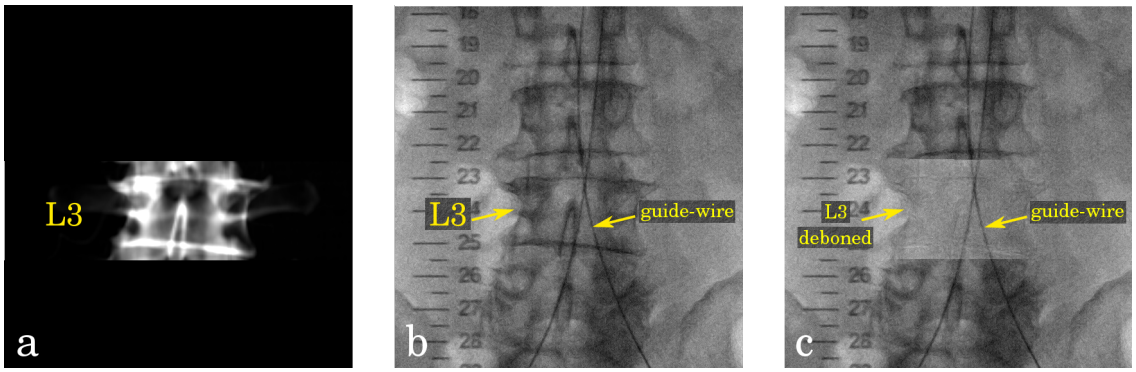

Figure 4.9: Vertebra removal using the produced DRR at the registration position prior to iDTS reconstruction. a) DRR of an automatically segmented L3 vertebra from the preoperative CT volume at registration position. b) Fluoroscopy image before, and c) after deboning L3.

Prior to iDTS image reconstruction, all of the vertebrae from each of the fluoroscopy images are subtracted using the process described above. This requires running the registration system for each of the vertebrae present in the fluoroscopy image to produce a DRR for each vertebra. iDTS image reconstruction is then carried out using these deboned fluoroscopy images such as the one shown in Fig. 4.10.b.

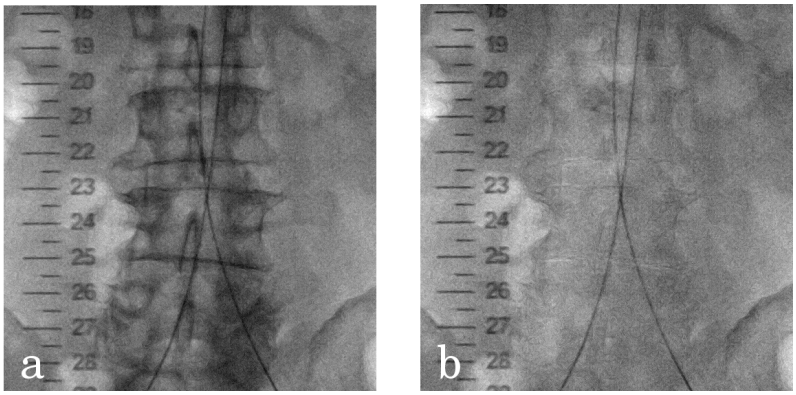

Figure 4.10: Removing all vertebral bone using the produced DRR at each vertebra registration position prior to iDTS reconstruction. a) A fluoroscopy image before, and b) after removing all vertebral bone to produce a deboned image.

4.4.2 iDTS reconstruction process

In Sec. 4.4.1, I explained how the 2D-3D registration can facilitate iDTS on a standard fluoroscopy system. In this section, the detailed reconstruction process of iDTS is given, step by step, as shown in Fig. 4.11, where the Roman numerals in the figure correspond to the following steps:

I. Segmenting a reconstruction surface (S_{rec}) from the preoperative CT. The surface should be chosen to contain structures of clinical interest to be enhanced (i.e. targeted vasculature).

II. Selecting a target image (I_T). This image is the fluoroscopy view the clinicians wish to use to guide their instruments. It could be chosen from one of the sweep images, or, after the sweep, the C-arm could be rotated back to the chosen clinical view and a single image is acquired and would be designated as the target image (I_T). In this latter case I_T should be contained within the range of the sweep images.

III. Carrying out 2D-3D registration between the CT scan and each input fluoroscopy image using the registration algorithm as described in Sec. 4.4.1. This allows spatial positioning of the fluoroscopy images in relation to the segmented CT reconstruction surface (Sec. 4.4.1.I and II), and deboning the fluoroscopy images prior to reconstruction (Sec. 4.4.1.III).

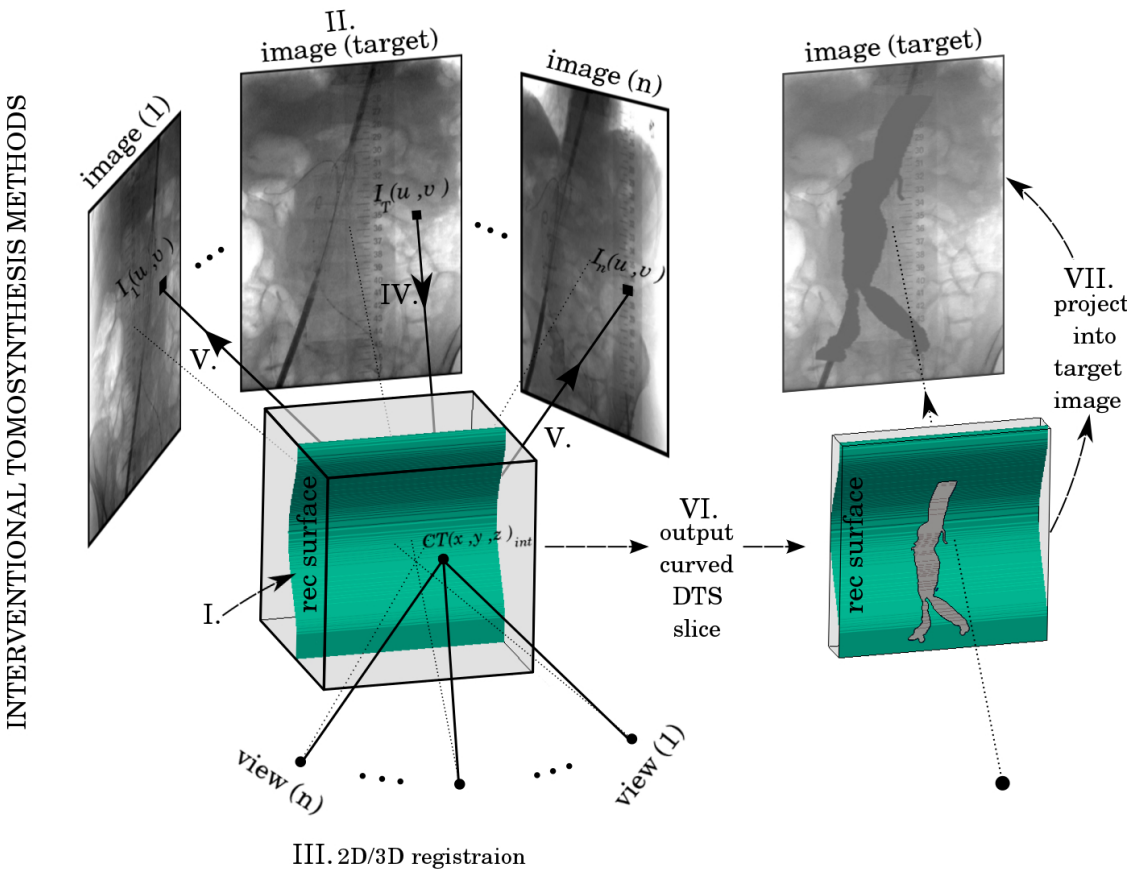

Figure 4.11: iDTS reconstruction process shown for one of the target image pixels: $I_T(u, v)$. A ray is back projected from $I_T(u, v)$ into the reconstruction surface using M_T. The 3D interception position $CT(x, y, z)_{int}$ is then projected into each fluoroscopy image in turn using the transformations M_i. The intensity at each 2D interception position $I_{fl_1}(u, v), \ldots, I_{fl_n}(u, v)$ is mapped back onto the reconstruction surface at $CT(x, y, z)_{int}$. The process is repeated for all target image pixels and the intensity values from all fluoroscopy images at each 3D interception position are averaged to calculate the intensity value of the curved iDTS slice. These intensity values, which contain additional clinical information, are then projected into the target fluoroscopy image to aid guidance.

IV. Back projecting rays from the target image pixels $I_T(u, v)$ using M_T, and calculating the 3D positions in $\mathbf{CT}_{3D}$, where the rays intercept the reconstruction surface $CT(x, y, z)_{int}$. This is defined as in Eqn. 4.9, where $\mathcal{F}_T$ calculates the interception of a line projected from the 2D target image I_T with the 3D reconstruction surface S_{rec}. Function $\mathcal{F}_T$ will take on different forms depending upon how the surface S_{rec} is defined. An analytic solution exists if S_{rec} is a

flat plane. I use an iterative method to allow a wide range of possible surfaces to be used.

$$\mathcal{F}_T(u, v, M_T, S_{rec}) = (x, y, z, 1)^T_{int} \tag{4.9}$$

V. Projecting rays from the 3D interception positions to each of the other fluoroscopy images in turn, to acquire the 2D interception position in $\mathbf{I}_{2D}$ (i.e. $I_{fl_1}(u, v), \ldots, I_{fl_n}(u, v)$). This is done using the transformations matrices M_i (i.e., $M_i(x, y, z, 1)^T_{int} = \lambda(u, v, 1)^T_i$).

VI. The intensity at each 2D position in the target image is mapped back onto the patient-anatomy-specific reconstruction surface at the corresponding 3D interception position. Then, the intensity values from all fluoroscopy images at each 3D interception position are averaged to produce a curved patient-anatomy-specific iDTS slice.

VII. Finally, in order to allow effective use of this new information, the reconstructed slice is projected onto the target image being used to guide the operation. This automatically produces an enhanced fluoroscopy image which shows additional information of the clinical features of interest in the FoV the clinicians are using. This can be expressed as in Eqn. 4.10:

$$I_{Tomo}(u, v) = \frac{1}{n} \sum_{i=1}^{n} I_i \Big(M_i \Big(\mathcal{F}_T(u, v, M_T, S_{rec}) \Big) \Big) \tag{4.10}$$

4.5 Discussion

This chapter concentrated on the use of iDTS during EIGS interventions, and I have designed methods that enable image acquisition and display which fit with the clinical work-flow. The ability to include a preoperative CT scan with the intra-operative imaging has the potential to enable more targeted image reconstruction and display. The CT scan can be segmented preoperatively using methods which due to algorithm time, or required amount of manual interaction, would not be appropriate during surgery. Preoperative segmentation of the aortic centreline is already part of routine planning for complex EVAR procedures. This then enables

intraoperative image reconstruction to automatically extract the clinically useful information. In addition, my proposed method to project reconstructed 3D iDTS information back into a 2D image enables the clinicians to continue operating with their preferred fluoroscopy view, and the process requires no clinician interaction which could interrupt the clinical work-flow.

4.6 Conclusions

In this chapter, I presented novel methods to enable improved iDTS on a standard fluoroscopy system. The proposed methods take advantage of a well established 2D-3D registration system which has been developed to improve EIGS, but suffers from intraoperative vascular deformation. By using this registration system, accurate iDTS reconstruction does not require mechanical tracking of the C-arm position any more, consequently, frequent calibration to maintain geometrical accuracy is also not required. Moreover, the registration system allows subtraction of vertebral bone from images prior to reconstruction which should greatly reduce clutter. Finally, rather than reconstructing a 3D iDTS volume which requires intraoperative input from surgeons to find the clinically relevant information and potentially interrupting the clinical work-flow, my proposed methods will automatically reconstruct a patient-anatomy-specific 2D image and display it to clinicians in their preferred fluoroscopy view.

In the next chapters, experiments are carried out to examine my methods using datasets acquired from a phantom and four patients undergoing complex EVAR of the AAA.

Chapter 5

Investigation into Vascular Enhancement Using iDTS with No Iodinated Contrast

Contents

5.1 Introduction

This chapter will investigate the proposed methods of improved iDTS using datasets from a phantom and four patients. The 2D-3D registration system described in Sec. 4.3 will be employed to reconstruct patient-anatomy-specific 2D iDTS images with much reduced clutter as detailed in Sec. 4.4. The chapter begins by explaining the method by which datasets were acquired. Experiments carried out using the acquired datasets are then described. Finally, results are presented and discussed.

5.2 Data and Experiments

Experiments were carried out using data from an abdominal spine phantom, and from 4 patients who underwent a complex EVAR procedure of the AAA (as presented in the case study in Sec. 2.5). Patient data was processed offline (i.e. not during the procedure), and was approved by the national research ethics committee (09/H0707/64), with informed patient consent. No attempt was made to select particular patient cases based on image quality or amount of intraoperative aortic deformation.

Each dataset had:

1. A preoperative diagnostic CT scan, acquired on a variety of machines depending on the referring hospital.

2. Intraoperative fluoroscopy screening images (i.e. low dose X-ray), acquired by rotating the C-arm approximately 40° RAO/LAO (from $\sim$ 20° RAO to $\sim$ 20° LAO). The phantom and the first 3 patient datasets were acquired on a Siemens FP20 system, while the 4th patient dataset was acquired on a Philips Allura Xper FD20 system as the operations moved operating theatre. The acquired screening images were sampled to obtain approximately one image per one degree of rotation (approximately 40 images for the 40° RAO/LAO sweep). An example of fluoroscopy image sampling for the phantom data is shown in Fig. 5.1. The graph on the left side plots the corresponding acquisition angle θ_z for each fluoroscopy image (114 images were acquired by rotating the C-arm from 20.07° LAO to 20.70° RAO). The right side graph

shows the same plot, but after sampling the fluoroscopy images to include approximately one image per one degree of rotation (out of 114 fluoroscopy images, only 40 images were sampled).

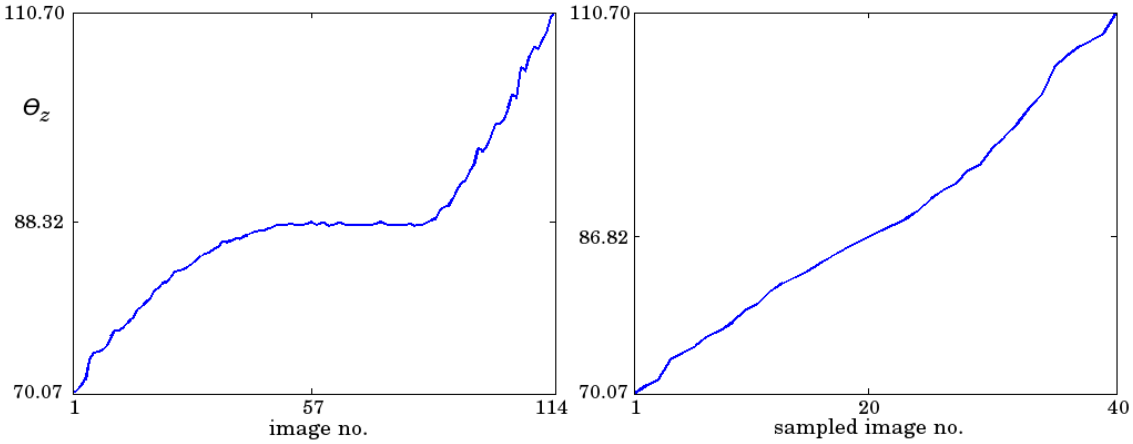

Figure 5.1: An example of fluoroscopy image sampling for the phantom data, which was acquired by a C-arm sweep of approximately 40°. In both graphs the corresponding acquisition angle θ_z for each fluoroscopy image is plotted, before (left side) and after (right side) image sampling to include approximately one image per one degree of rotation (out from 114 fluoroscopy images in the left side graph, only 40 images were sampled in the right hand graph).

For each dataset, two iDTS images were reconstructed from approximately an AP view (i.e. chosen target image had ∼AP view), as described in Sec. 4.4.2:

1. The first iDTS image was reconstructed using the ∼ 40 sampled standard screening images (which will be called standard iDTS).

2. The second iDTS image was reconstructed using the ∼ 40 sampled screening images, but after removing the vertebral bone as described in Sec.4.4.1.III (which will be called deboned iDTS (de-iDTS)).

5.2.1 Phantom experiment

The used phantom consisted of a pelvis and five lumber vertebrae encased in homogeneous acrylic resin, which is approximately equivalent to soft-tissue in the diagnostic X-ray energy range (Fig. 5.2.a and 'b'). The CT scan of the phantom was

acquired with a voxel size of $1.094 \times 1.094 \times 1.487\,\text{mm}^3$. The fluoroscopy screening images of the phantom were acquired with image dimensions of 1024×1024 pixels, pixel sizes of $0.372 \times 0.372\,\text{mm}^2$, frame rate of 30 fps (the highest frame rate available), and FoV of 48 cm.

Two phantom experiments were carried out:

1. The first experiment investigated the ability of iDTS to enhance instruments and features, such as catheters and calcium deposits on the aortic wall. For this purpose and prior to fluoroscopy acquisition, the following was attached to the anterior surface of the phantom: a catheter and three pieces of synthetic rubber compound (Blu-Tack) to represent calcium in the aortic wall, as seen in Fig. 5.2.a.

2. The second experiment investigated the ability of iDTS to enhance vasculature without ICM injection (i.e. to detect the outline of the aorta). For this purpose and prior to fluoroscopy acquisition, a thin layer of synthetic rubber compound in the shape of an AAA was placed on the anterior surface of the phantom in an anatomically realistic superior-inferior position, as seen in Fig. 5.2.b.

For both experiments, the anterior surface of the CT volume illustrated in Fig. 5.2.c in a green colour, was used as the reconstruction surface. Moreover, to illustrate the advantage of using a curved surface over a flat plane for reconstruction, the flat plane shown in Fig. 5.2.d in a green colour was also used for reconstruction for the first experiment. The flat plane only intersects part of the anterior surface of the phantom.

5.2.2 Experiment with patient data

Each patient's standard diagnostic CT scan was used. These had voxel sizes which ranged from $0.683 \times 0.683 \times 0.7\,\text{mm}^3$ to $0.974 \times 0.974 \times 1\,\text{mm}^3$. The fluoroscopy screening images of all patients were acquired with image dimensions of 1024×1024 pixels, pixel sizes of $0.372 \times 0.372\,\text{mm}^2$, and FoV of 48 cm. The highest frame rate available was used to acquire patient datasets. This was 30 fps for the first 3 patient

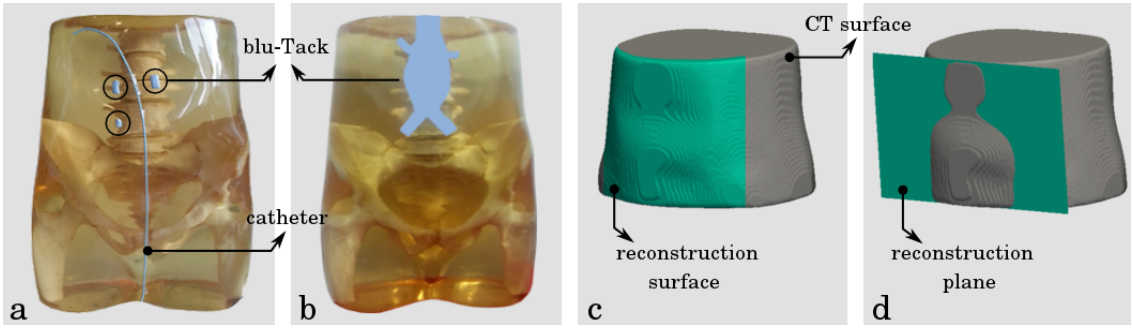

Figure 5.2: Phantom experiments illustration for iDTS reconstruction. a) and b) An anterior view of the used phantom with: a) a catheter and 3 pieces of synthetic rubber compound (Blu-Tack) to represent calcium, and b) one piece of synthetic rubber compound in the shape of an AAA. c) and d) A 3D rendering of the CT surface with: c) a reconstruction surface including the CT anterior surface, and d) a reconstruction plane intersecting part of the CT anterior surface.

datasets, and 15 fps for the 4th patient dataset as a different fluoroscopy set was used when the operations moved operating theatre.

For each patient, the aorta was segmented using a semi-automatic method in ITK-SNAP [Yushkevich et al., 2006]. The reconstruction surface was then defined by picking points along the midline of the aorta, iliac and renal arteries, and then producing a surface using thin-plate-spline interpolation [Rohr et al., 1999]. An example of such a surface can be seen in Fig. 5.3, from two different views: AP ('a'), and lateral ('b'). This surface was chosen to enhance blood vessels of interest: the aorta, renal and iliac arteries, and aortic calcium if present.

5.2.3 Validation experiments

As described in Sec. 5.2, for each dataset, standard and deboned iDTS images were reconstructed from ∼AP view using ∼ 40 screening images acquired by a ∼ 40° RAO/LAO C-arm sweep.

For comparison with images which are also taken from a single view position, the following two images were used for each dataset:

1. The target image (I_T).

2. A high contrast image (I_{HC}) which required an equivalent amount of radiation as iDTS, but was acquired from a single view point (i.e. no rotation) and from

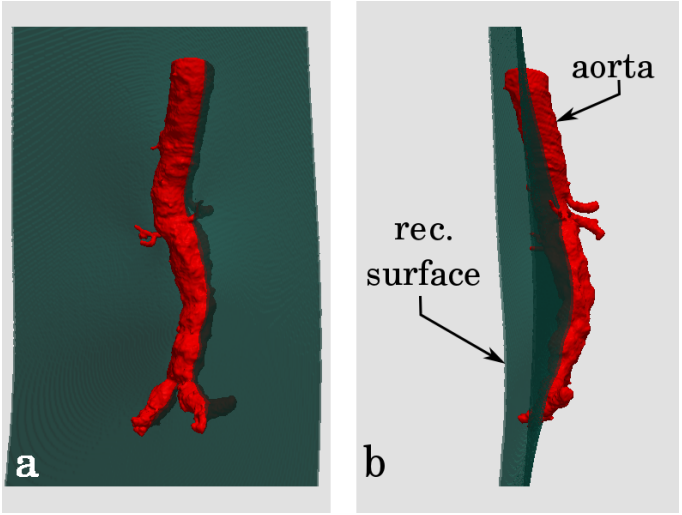

Figure 5.3: Illustration of the surface used for iDTS reconstruction from two different anatomical views: a) anterior-posterior (AP), and b) lateral. The surface was defined along the aorta using thin-plate-spline interpolation.

approximately an AP view. For the phantom experiments, a specific set of images were acquired for this purpose. For the patient experiments, a set of screening images acquired as part of the routine intervention, at a time point close to when the iDTS sweep was taken, were used. In both cases, $\sim$ 40 images were saved and averaged to produce I_{HC}.

Using signal difference to noise ratio (SDNR)

For the phantom dataset, signal difference to noise ratios (SDNRs) were calculated using three profile lines (PLs) through the three pieces of synthetic calcium in the first experiment.

The SDNR value, which measures a feature's detectability in the reconstructed image, was calculated as defined by Wu et al. [2004] in the following equation:

$$SDNR = \frac{\bar{I}_{FG} - \bar{I}_{BG}}{\sigma_{BG}} \tag{5.1}$$

where $\bar{I}_{FG}$ and $\bar{I}_{BG}$ are the mean normalized intensities of automatically delineated foreground (i.e. feature of interest), and background PL regions, respectively, and σ_{BG} is the standard deviation of background intensities.

For each SDNR calculation, I_T, I_{HC}, iDTS, and de-iDTS were all input into a developed program which:

1. Allowed the user to manually place a PL inside de-iDTS. Foreground and background regions were then automatically determined using the full width half maximum method.

2. Automatically placed PLs inside I_T, I_{HC}, and iDTS, at the same position of the manually placed PL inside de-iDTS.

3. Calculated SDNR along the PL inside each image using Eqn. 5.1.

In addition, the program automatically performed three calculations for each PL: one directly on the PL, and two others with the PL shifted vertically by ±3 pixels as illustrated in Fig. 5.4. Averaging the three SDNR values for each PL increased the consistency of the SDNR calculations.

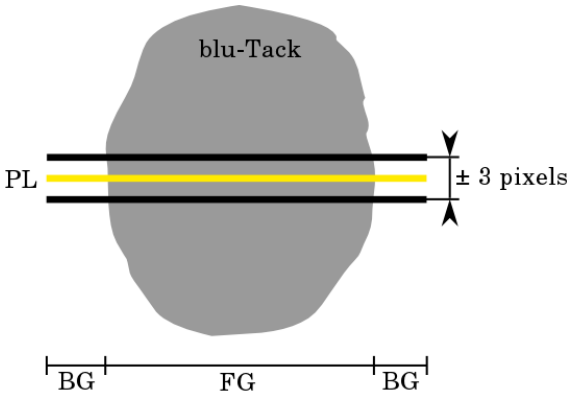

Figure 5.4: Method to calculate SDNR using a profile line (PL) across the synthetic calcium (blu-Tack). Using the FWHM, foreground (FG) and background (BG) regions were determined. For each PL, three calculations were made, one directly on the PL and two others with the PL shifted vertically by ±3 pixels.

Using preoperative overlays

For patient datasets, features enhanced in the iDTS images were visually compared with the validation images: I_T and I_{HC}. In addition, CT surface rendering of enhanced features were overlaid onto the iDTS images as described in Sec.4.3.4. Two types of CT features were overlaid: 1) the surface of the aorta and visceral vessels, and 2) the aortic calcification. The overlay was initially achieved using the transformation provided by the registration system for I_T (i.e. M_T). However, due to intraoperative deformation of the aorta (caused by the stiff interventional

instruments), a manual adjustment process (in-plane translation) was required to accurately match the overlay with the iDTS features (see Sec.4.3.4). This illustrates one possible use of iDTS images: to provide additional intraoperative information on the position of soft-tissue structures to update a rigid body registration.

5.3 Results

For each dataset, I show:

a) The target image (I_T).

b) The high contrast image (I_{HC}).

c) The iDTS image reconstructed using the curved surface.

d) The de-iDTS image reconstructed using the curved surface and after bone removal.

For the phantom dataset, I also present the SDNR values and percentage improvements in SDNR compared to I_T. In addition, I show the standard and deboned iDTS images reconstructed using a flat plane, and present recalculated SDNR values and percentage changes in SDNR compared to the curved surface results.

5.3.1 Phantom results

Figure 5.5 shows the phantom results using the curved reconstruction surface illustrated in Fig. 5.2.c.

Results for the first experiment (catheter and synthetic calcium) are shown in the top row. The high contrast catheter can be clearly seen in all images. The low contrast synthetic calcium cannot be clearly distinguished from the overlying vertebrae in I_T ('a') nor I_{HC} ('b'), whereas the synthetic calcium is clearly visible in both the iDTS ('c') and de-iDTS ('d') images (indicated with yellow circles).

Similar results are observed for the second experiment (aneurysm-shaped synthetic rubber compound) shown in the bottom row. The outline of the synthetic aorta is not visible in I_T ('a') nor I_{HC} ('b'), but can be clearly seen in the iDTS

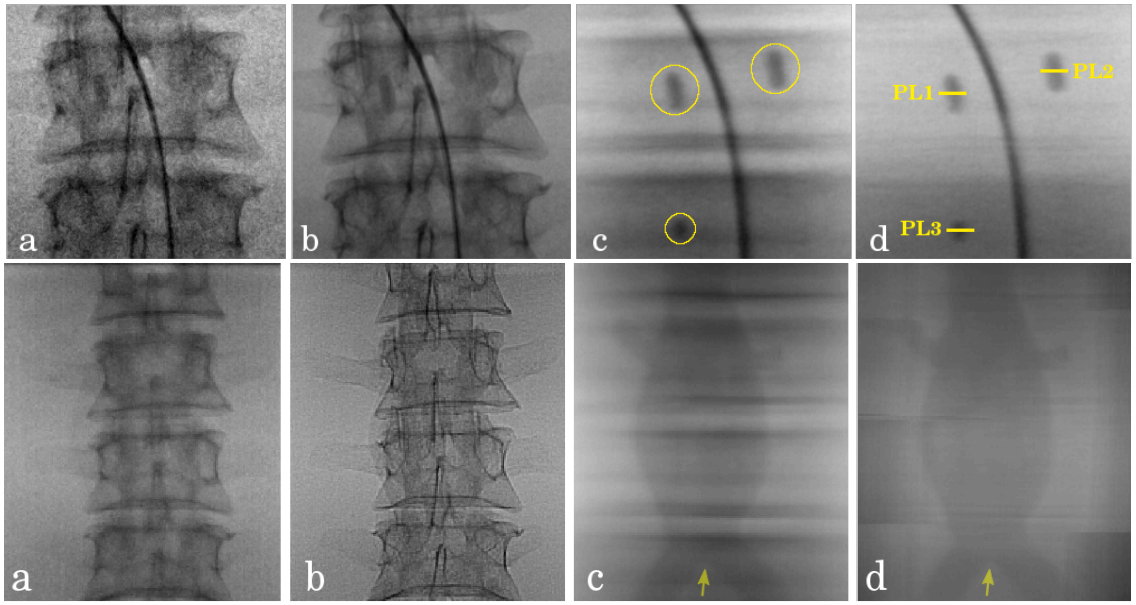

Figure 5.5: Validation images: a) I_T and b) I_{HC}, and the reconstructed iDTS images: c) iDTS and d) de-iDTS from the phantom first experiment (top row) and the second experiment (bottom row). In the top row, circles indicate synthetic calcium and the yellow lines indicate the PLs positions. In the bottom row, yellow arrows indicate aortic bifurcation.

('c') and de-iDTS ('d') images. The aortic bifurcation can also be seen in 'c' and 'd' (indicated with yellow arrows).

The effect of the deboning process can clearly be seen in the results from both experiments by comparing the standard 'c' and deboned 'd' iDTS images. The horizontal bands in 'c' are clutter caused by the high contrast vertebra edges, these are almost totally removed by the deboning process, as shown in the de-iDTS results 'd'.

Table 5.1 lists SDNR results, and percentage improvements in SDNR compared to I_T, calculated on the PLs shown in Fig. 5.5.d (top row), which were through synthetic calcium. The averaged percentage improvements are presented in bold text. An averaged improvement of 203.53% is seen for I_{HC} as random noise was averaged. Both iDTS and de-iDTS images show substantial averaged improvements of 2315.9% and 2563.16% respectively, for the low contrast synthetic calcium, and the further improvement due to the deboning method is clearly seen.

To illustrate the advantage of using a curved surface over a flat plane for reconstruction, the flat plane shown in Fig. 5.2.d was also used to reconstruct standard

Table 5.1: Calculated SDNR with percentage improvements compared to I_T in brackets, for the three PLs shown in Fig. 5.5.d. Averaged percentage improvements are presented in bold text.

	I_T (a)	I_{HC} (b)	iDTS (c)	de-iDTS (d)
PL1:SDNR (improvement %)	0.19 (-%)	0.78 (+310.58%)	5.33 (+2705.26%)	5.45 (+2768.42%)
PL2:SDNR (improvement %)	0.11 (-%)	0.22 (+100%)	3.43 (+3018.18%)	5.53 (+4927.27%)
PL3:SDNR (improvement %)	0.19 (-%)	0.57 (+200%)	4.59 (+2315.9%)	5.06 (+2563.16%)
avg. improvement %	**-**	**+203.53%**	**+2679.78 %**	**+3419.62%**

and deboned iDTS images for the first experiment (catheter and synthetic calcium), as shown in Fig. 5.6.

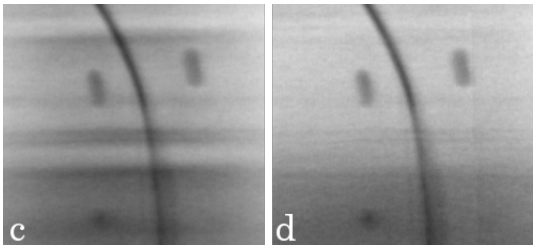

Figure 5.6: iDTS reconstruction results from the phantom first experiment using the flat plane shown in Fig. 5.2.d: c) iDTS and d) de-iDTS.

SDNR values were then recalculated for the de-iDTS image only, using the same positions of PLs 1, 2, and 3 shown in Fig. 5.5.d (top row). Table 5.2 shows the calculated SDNR values using a curved reconstruction surface (same as presented in Tab. 5.1.d), the recalculated SDNR values using the flat reconstruction plane, the percentage change in SDNR value after using the flat plane, and the distance between each piece of synthetic calcium and the flat plane. The distance between the synthetic calcium and the curved reconstruction surface can be assumed to be negligible because the synthetic calcium is attached to the anterior surface of the phantom, and this surface was used for reconstruction.

There is only a small change in SDNR values recalculated over PLs 1 and 2 (the

Table 5.2: Recalculated SDNR values for the de-iDTS image reconstructed using the flat plane shown in Fig. 5.2.d, and the percentage change in SDNR value compared to using the curved surface with the shortest distance from the centre of gravity of each piece of synthetic calcium to the flat plane in mm.

	de-iDTS (d)			
	curved surface	flat plane	change %	distance from plane
PL1:SDNR	5.45	5.31	-2.64%	1.09 mm
PL2:SDNR	5.53	5.91	+6.87%	1.09 mm
PL3:SDNR	5.06	2.93	-42.09%	9.85 mm

two top pieces of synthetic calcium, as shown in Fig. 5.5.d top row) because in this region, the flat and curved planes are within 1 mm. However, for the lower piece of synthetic calcium (PL 3), where the flat plane is approximately 10 mm away from the synthetic calcium, a large decrease in SDNR (-42.09%) can be seen.

Those results are backed up by visual inspection of Fig. 5.6, where the two top pieces of synthetic calcium look similar to images 'c' and 'd' in Fig. 5.5 top row, whereas the lower piece of synthetic calcium is blurred in the case of the flat plane compared to the curved surface result.

5.3.2 Patient results

Figures 5.7, 5.8, 5.9, and 5.10 show the patient dataset results using the curved reconstruction surface defined as illustrated in Fig. 5.3.

For each patient I show: the validation images I_T ('a') and I_{HC} ('b'); the iDTS ('c') and de-iDTS ('d') images; and the CT surface rendering of enhanced features: aorta and visceral vessels ('e'), and aortic calcium ('f').

In patients 1 and 2, almost no features from the aorta are visible in images I_T and I_{HC}; whereas in the iDTS image, and more so in the de-iDTS image, the aorta outline and some calcium are enhanced, as shown by comparison with the CT overlay images.

In patients 3 and 4, which had increased calcium in the aorta, some areas of the aorta outline can be seen in images I_T and I_{HC}. The aorta is most noticeable in regions where the outline is not obscured by bony anatomy. However, the iDTS

image, and again more so for the de-iDTS image, are able to clearly show the aortic outline over most of their length, and are hardly affected by overlying bony features.

It should be noted that the aortic outline visible in the iDTS images is the entire aorta (i.e. aorta lumen plus thrombus), whereas in a DSA image, only the aorta lumen (i.e. where the contrast flows) would be visible. The aortic outline is visible because its linear attenuation coefficient is larger than that of the surrounding connective tissues. Calcium deposits in the aorta increase this difference between linear attenuation coefficients, and so improve visualisation.

5.3.3 iDTS imaging time

Time for image acquisition and reconstruction can be split into four main steps:

1. The $\sim$ 40° RAO/LAO sweep, which took 8.23 sec on average. However, setup time and explaining the procedure to the radiographer resulted in image acquisition times of up to one minute. This is expected to be reduced greatly if the process became more routine.

2. The 2D-3D registration has been optimised to work on GPUs. Registrations were performed on a computer with two NVidia GTX 690 graphic cards with each card containing two GPUs, and took 1.25 sec per registration. Therefore, the registration process for $\sim$ 40 images was around 50 sec for each vertebra (registrations for all vertebra in each image for bone removal were run in parallel). The latest graphics cards would reduce this time.

3. Removing one vertebra took around 0.5 sec. Thus, the bone removal process for $\sim$ 40 images was around 20 sec for each vertebra (bone removal for all vertebra in each image was run in parallel).

4. The iDTS reconstruction process was around 20 sec. Because relatively simple calculations are required and because the process can be highly parallelized, speed improvements are possible.

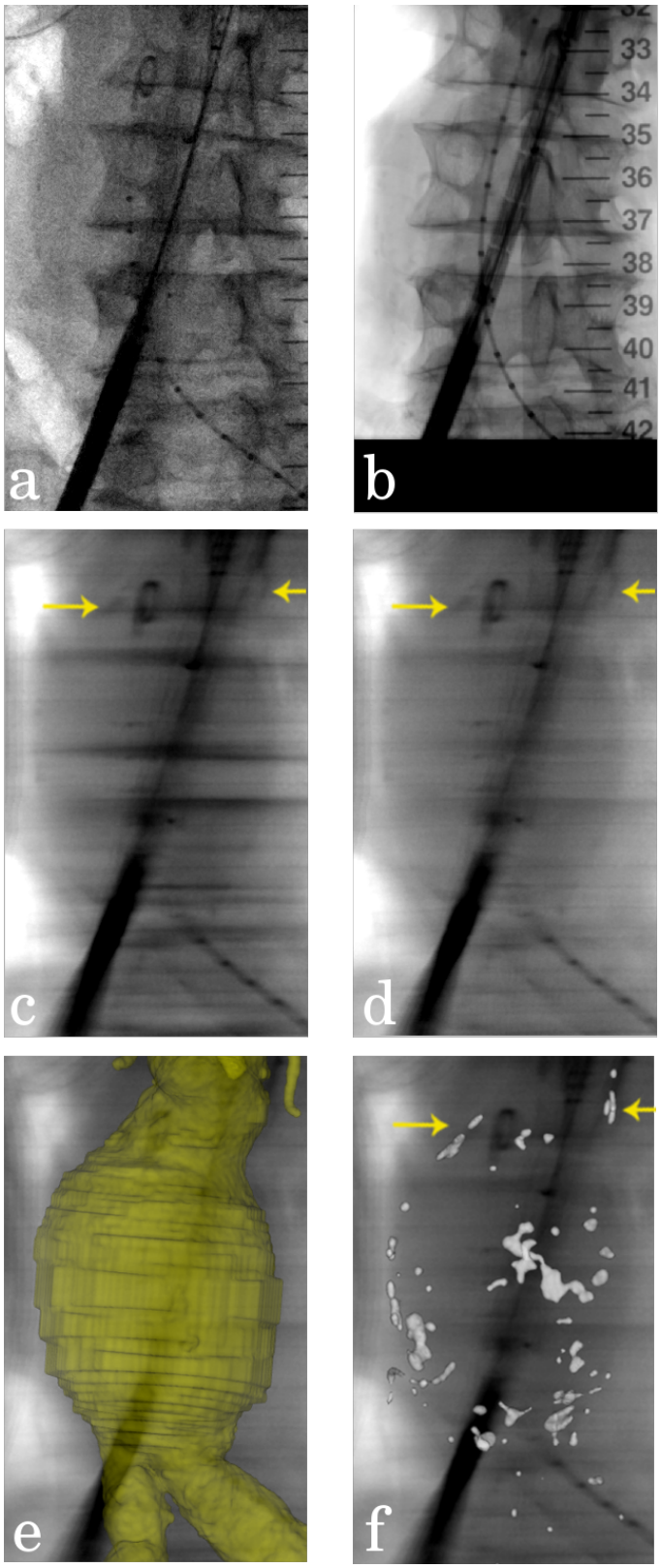

Figure 5.7: iDTS reconstruction results from patient 1 experiment: a) I_T, b) I_{HC}, c) iDTS, d) de-iDTS, e) AAA overlay, and f) calcification overlay onto the de-iDTS image. Arrows indicate calcium deposits.

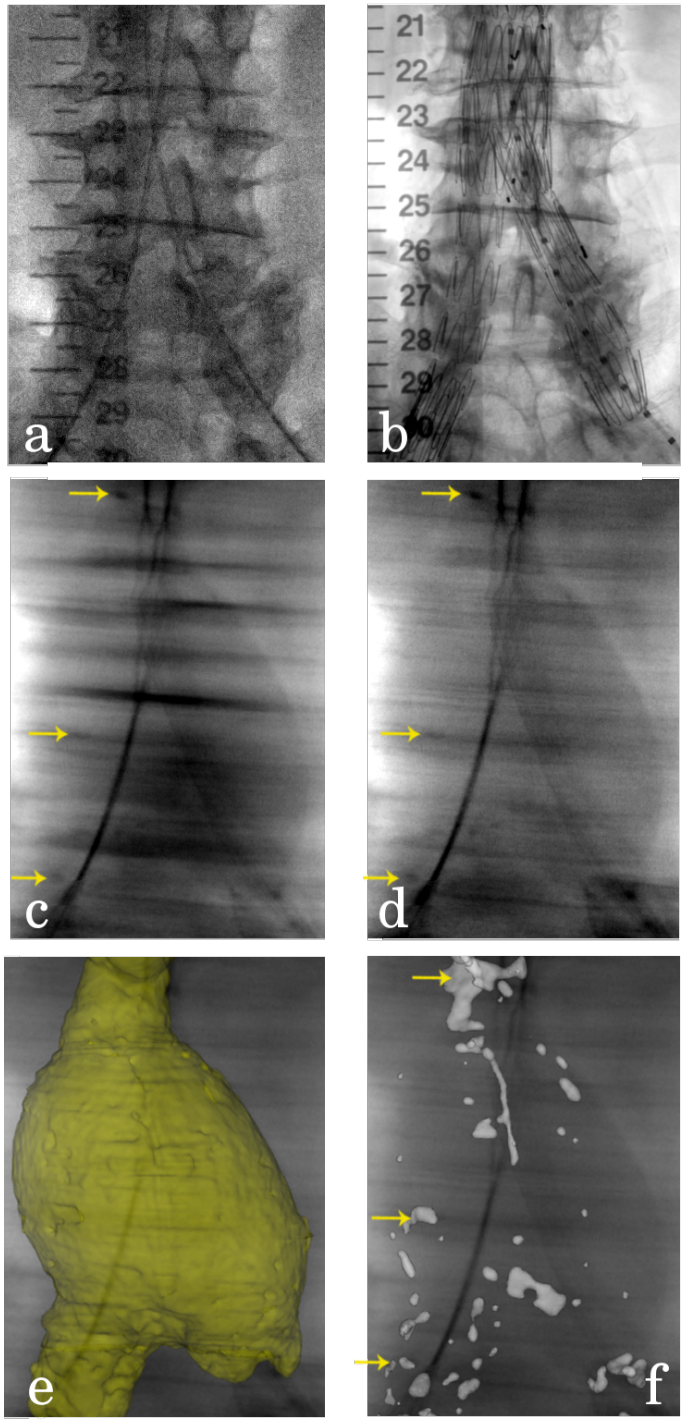

Figure 5.8: iDTS reconstruction results from patient 2 experiment: a) I_T, b) I_{HC}, c) iDTS, d) de-iDTS, e) AAA overlay, and f) calcification overlay onto the de-iDTS image. Arrows indicate calcium deposits.

5.3.4 iDTS radiation exposure

Exposure values were recorded by the fluoroscopy system and saved in the DICOM header as the image area dose product (dGy.cm^2). In Tab. 5.3, I report the exposure

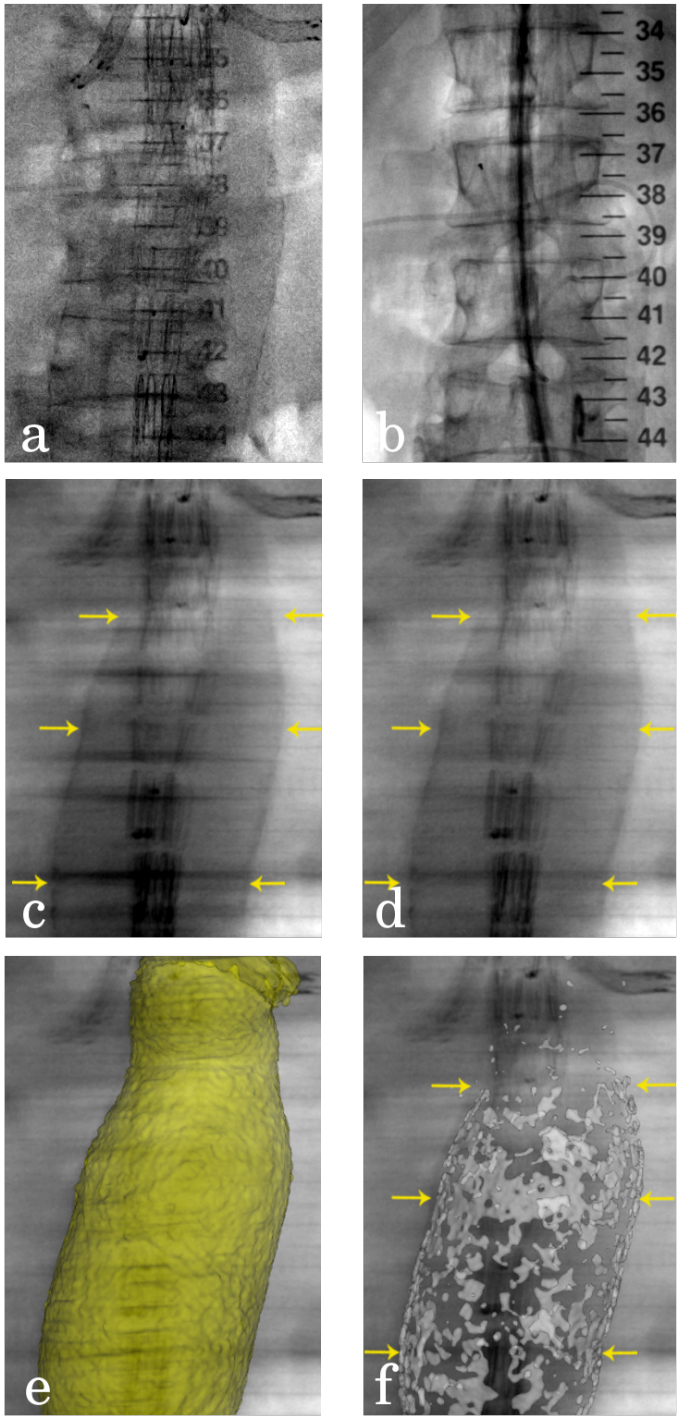

Figure 5.9: iDTS reconstruction results from patient 3 experiment: a) I_T, b) I_{HC}, c) iDTS, d) de-iDTS, e) AAA overlay, and f) calcification overlay onto the de-iDTS image. Arrows indicate calcium deposits.

value from the iDTS sweep for patients 1, 2 and 3 (patient 4 exposure value was not available). Reported iDTS radiation exposure is for all frames (i.e. not just the sampled $\sim$ 40 frames). For comparison, I also report the exposure from a mean DSA

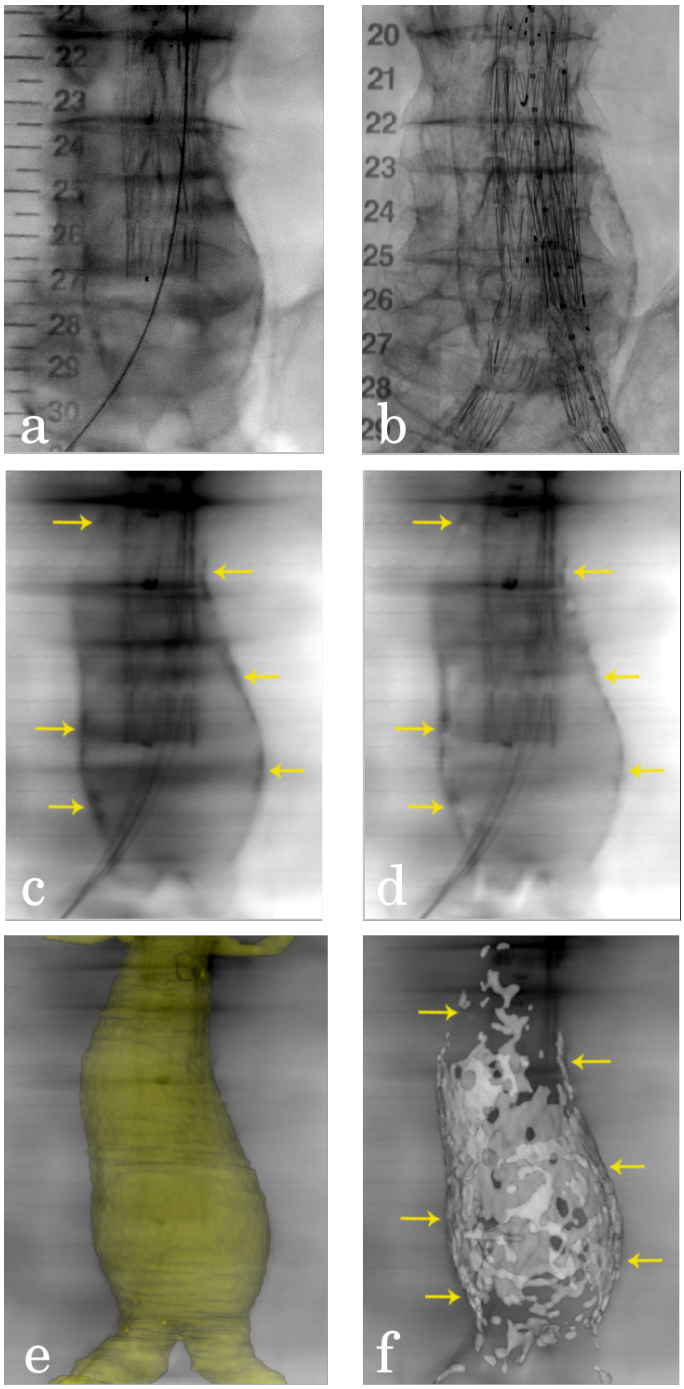

Figure 5.10: iDTS reconstruction results from patient 4 experiment: a) I_T, b) I_{HC}, c) iDTS, d) de-iDTS, e) AAA overlay, and f) calcification overlay onto the de-iDTS image. Arrows indicate calcium deposits.

sequence for patients 2 and 3 (as for these patients iDTS and DSA were acquired with the same FoV), and present the percentage decrease in exposure between DSA and iDTS. The results clearly show that iDTS images involve much lower radiation exposure than DSA images with an averaged decrease of 93.96% for iDTS imaging.

Table 5.3: Radiation exposures for the DSA image and the iDTS sweep for patients 1, 2, and 3, with percentage decrease. Averaged values are presented in bold text.

	DSA (dGy.cm^2)	iDTS (dGy.cm^2)	decrease %
Pat 1: exposure	-	8.65	-%
Pat 2: exposure	98.28	5.03	-94.88%
Pat 3: exposure	93.46	3.68	-96.06%
avg. exposure	**95.87**	**5.79**	**-93.96%**

5.4 Discussion

The development of a novel interventional imaging technology capable of vasculature enhancement is challenging. Low ICM usage, low radiation dose exposure, minimal interruption to the clinical work-flow, and short acquisition and reconstruction times are all key requirements for an effective interventional modality (see Sec. 2.2.2).

At first glance my proposed method appears counter intuitive as a high quality CT scan is required to produce a lower quality de-iDTS image. However, the high quality CT scan is already available as a part of the routine planning for the procedure, and although the de-iDTS is of lower "image quality", it is far superior in terms of the position of the patient's vasculature in relation to interventional instruments during the procedure.

I have presented a novel technique: "interventional digital tomosynthesis facilitated by 2D-3D image registration", which can be directly implemented on existing fluoroscopy systems. The small C-arm sweep of $\sim 40°$ took less than one minute for image acquisition. Therefore, disruption to the clinical work-flow was very low compared to CBCT imaging, and is probably equivalent to that of DSA imaging.

DSA imaging is routine in endovascular procedures and the greatly increased opacity of the ICM enables much smaller vascular structures to be seen than my proposed de-iDTS method. However, as shown by the patient results (Figs. 5.7, 5.8, 5.9, and 5.10), de-iDTS was able to enhance the aortic outline and calcium deposits; and this was achieved using no injection of ICM and with much reduced radiation dose (see Tab. 5.3). I propose that de-iDTS could find a role alongside DSA imaging, replacing DSA imaging where appropriate (i.e. observing large scale features such

as the aortic outline), while using DSA for critical points in the procedure, and to see small structures.

Moreover, as mentioned in Sec. 5.3.4, the reduction in radiation exposure compared to DSA imaging reported in Tab. 5.3, was calculated for all frames acquired during the C-arm sweep (i.e. not just the sampled $\sim$ 40 frames). However, if my technique became incorporated with fluoroscopy systems where only one image per one degree of rotation is acquired, further reduction in dose is possible. Table 5.4 shows similar numbers to Tab. 5.3, however, the reported iDTS radiation exposure is only for the sampled $\sim$ 40 frames (i.e. iDTS_{40}). A further 4.06% reduction in radiation exposure can be clearly seen (from -93.96% to -98.02%).

Table 5.4: Radiation exposures for the DSA image and the sampled fluoroscopy images only, for patients 1, 2, and 3. Averaged values are presented in bold text.

	DSA (dGy.cm^2)	iDTS_{40} (dGy.cm^2)	decrease %
Pat 1: exposure	-	1.35	-%
Pat 2: exposure	98.28	1.14	-98.84%
Pat 3: exposure	93.46	3.20	-96.58%
avg. exposure	**95.87**	**1.90**	**-98.02%**

The proposed method requires very little setup and only involves a small angle sweep of the C-arm ($\sim$ 40° RAO/LAO). The relative positions between each of the 2D sweep images is calculated using 2D-3D registration. Therefore, the new method is able to work with any fluoroscopy system, and does not require mechanical tracking of the C-arm nor frequent calibration. This is particularly important in C-arm systems which are known to exhibit gravity-induced mechanical flex. If information on C-arm position was available then this could be used to speed up the registration process.

A second potential use of de-iDTS imaging is to provide intraoperative information on the position of the aorta to enable non-rigid 2D-3D image registration. As described in Sec. 5.2.3, the preoperative CT overlays shown in 'e' and 'f' in Figs. 5.7, 5.8, 5.9, and 5.10, needed manual adjustment after the rigid registration to accurately match features of interest in the de-iDTS images. This was needed to account for aortic deformation caused by the stiff interventional instruments (see

Sec. 2.4.2). Repeated de-iDTS images could be taken throughout the procedure, which could provide information to a 2D-3D non-rigid registration algorithm to increase the accuracy of IGS.

Intraoperative deformation can occur between the vertebra on which the registration is based and the position of the reconstruction surface. This may cause errors in the position of the reconstruction surface. For a large structure such as the aorta, which is not expected to undergo large deformations (usually less than 10 mm as reported by Carrell et al. [2010]), deformation is not expected to be a major problem because even after deformation, a reconstruction surface based on preoperative anatomy should still intercept the aorta. However, for visualisation of smaller clinical structures, which move by a larger amount, deformation could result in use of a reconstruction surface a long distance from the intraoperative position of the clinical structure. This would reduce the contrast of the reconstructed clinical structure.

The bone removal process will subtract information segmented from the CT and rigidly registered to the fluoroscopy images. I use a very simple segmentation process, simply a bounding box around the vertebra and then an intensity threshold to produce a DRR (see Sec. 4.3.1). DRR intensities should only include voxel values from vertebral bone. However, if non-vertebral intensities are included, then these will also be subtracted by the method, and so will not be visible in the de-iDTS image. If these non-vertebra features do not move in a rigid body relationship with the vertebra then artefacts could occur. Further investigations will reveal whether these are important issues. If so, a first step for a solution would be to investigate using more sophisticated segmentation algorithm such as Klinder et al. [2009].

5.5 Conclusions

In conclusion, a novel method to enhance vasculature using de-iDTS during interventional procedures has been presented. The method employs a 2D-3D image registration system to enable production of de-iDTS images on standard interventional equipment, with much reduced out-of-plane clutter, and on a patient tailored reconstruction surface. Phantom numerical results showed a 3419.62% SDNR

improvement compared to standard fluoroscopy. Results from phantom and four patient datasets showed the method's ability to automatically enhance structures of clinical interest: the aorta outline and aortic calcium, without the use of ICM, and with an average percentage decrease of 93.96% in radiation dose compared to DSA imaging.

On the other hand, DSA imaging enables much smaller vascular structures to be enhanced than my proposed de-iDTS method. In the next chapter, I will investigate extending the current proposed methods to be able to enhance small aortic vasculature, such as the renal ostia, by injecting a small amount of ICM during the C-arm sweep.

Chapter 6

Investigation into Vascular Enhancement Using iDTS with a Reduced Amount of Iodinated Contrast

Contents

6.1 Introduction

In the previous chapter (Ch. 5), de-iDTS was able to enhance the aortic outline and calcium deposits without the injection of any ICM, and with much reduced radiation dose compared to DSA imaging (see Tab. 5.3). However, in the presented clinical results (see sec. 5.3.2), de-iDTS was not able to enhance the renal ostia which is often the clinically relevant feature.

This chapter is an extension to Ch. 5, in which the 2D-3D registration system described in Sec. 4.3, is also employed to reconstruct patient-anatomy-specific 2D de-iDTS images with much reduced clutter. However, in this chapter, I propose injecting ICM during the C-arm sweep for further vascular enhancement, especially for visualizing small vascular structures, such as the renal ostia. The ICM volume I propose to be injected is much smaller than that used for standard DSA imaging (e.g. 10-30% the amount of ICM used in standard DSA imaging).

All experiments in this chapter were carried out using 40 CT-based synthetic fluoroscopy images to simulate a 40° C-arm sweep (i.e. one image per one degree of rotation). Simulated contrast was then added in different amounts before de-iDTS reconstruction. Methods for generating synthetic images were developed to avoid injecting additional nephrotoxic ICM volumes during procedures for the purpose of this thesis, which would not be ethically acceptable. I also developed methods to produce realistic contrast enhanced synthetic fluoroscopy images. These images were used in experiments to investigate how useful a small contrast injection during the de-iDTS sweep would be to enhance small vascular structures.

6.2 Generation of Realistic Contrast Enhanced Synthetic Fluoroscopy Images

As mentioned in Sec. 4.3.1, DRRs are produced by casting rays through the CT volume and integrating HUs of voxels along each ray. The HU of a CT voxel is related to the linear attenuation coefficient of that voxel (i.e. μ) by Eqn. 6.1, where μ_w is the linear attenuation coefficient of water:

$$HU = 1000 \times \frac{\mu - \mu_w}{\mu_w} \tag{6.1}$$

The process of casting rays through a CT volume to produce a DRR image resembles the process of projecting X-ray through a medium to produce a fluoroscopy image. Assuming a monoenergetic beam of X-ray, the relationship between the intensity of the incident X-ray on the image detector ($I_{detector}$), and the linear attenuation coefficient of the travelled medium is described by Lambert-Beer law stated in Eqn. 6.2, where I_0 is the initial X-ray intensity, and z is the distance travelled through the medium which has a linear attenuation coefficient of $\mu(z)$:

$$I_{detector} = I_0 e^{-\int_0^z \mu(z)dz} \tag{6.2}$$

By combining Eqn. 6.1 and Eqn. 6.2, we can relate the intensity of the incident X-ray on the image detector, to the integral of Hounsfield units along the ray path, such as:

$$I_{detector} = I_0 e^{-\int_0^z \left(\frac{HU(z)\mu_w}{1000} + \mu_w\right)dz} \tag{6.3}$$

Typically, the intensities of $I_{detector}$ are logarithmically transformed prior to image processing and visualization [Hensel et al., 2007]. This transformation compensates for the exponential photon attenuation seen in Eqn. 6.2, so that the final image intensities are proportional to the travelled medium thickness. Moreover, DSA imaging requires the intensities of $I_{detector}$ to be logarithmically transformed [Brody, 1982, Kruger et al., 1981, Tobis et al., 1983], therefore, I assume a logarithmic relationship between the final fluoroscopy image I_{fl} and the incident X-ray on the image detector $I_{detector}$, as shown in Eqn. 6.4:

$$I_{fl} \propto log(I_{detector}) \tag{6.4}$$

Eqn. 6.3 and Eqn. 6.4 can be combined to produce Eqn. 6.5, which shows that the fluoroscopy image intensities are linearly related to the integral of Hounsfield units along the ray path:

$$I_{fl} \propto \log(I_0) - \mu_w z - \frac{\mu_w}{1000} \int_0^z HU(z)dz \tag{6.5}$$

Therefore, I can assume that the relationship between the fluoroscopy image intensities and the produced DRR values at the registration position is linear, as in Eqn. 6.6:

$$I_{fl} = a.DRR + b \tag{6.6}$$

Nevertheless, the above equations assume that the CT and fluoroscopy images are both acquired using the same X-ray spectrum, which is not usually true. For example, all the CT scans mentioned in Sec. 5.2 were acquired at a peak voltage of around 120 KeV, whereas the sweep fluoroscopy images were acquired at a peak voltage of around 88 KeV. Therefore, since the linear attenuation coefficient is dependent on the X-ray spectrum for each material, the ratio of the linear attenuation coefficient of bone (μ_{bone}) to soft-tissue (μ_{tissue}) will vary depending on the peak voltage used. The ratio of μ_{bone} to μ_{tissue} at 120 KeV is lower than the ratio at 88 KeV, as a result, the produced DRR image will have a lower bone to soft-tissue contrast, compared to the fluoroscopy image. Thus, the difference between the CT and fluoroscopy X-ray spectra has to be accounted for in order to produce a realistic synthetic fluoroscopy image using the generated DRR at the registration position.

To account for the X-ray spectrum differences, I took a similar approach to Walsum et al. [1997], which involves segmenting the CT volume into bone, soft-tissue, and vessels, before generating three DRR images, one for each segmentation. Therefore, Eqn. 6.6 can be extended to include the DRRs produced from all segmentations, as shown in Eqn. 6.7:

$$I_{fl} = a_{bone}.DRR_{bone} + a_{tissue}.DRR_{tissue} + a_{contrast}.DRR_{vessels} + b \tag{6.7}$$

Equation 6.7 can be solved using linear least square fitting, however, because the fluoroscopy image contains no ICM, $a_{contrast}$ will have zero value. To calculate how much simulated contrast has to be added to produce a realistic effect in the synthetic angiography images, I solve Eqn. 6.7 using an angiography image for the linear fitting instead of a fluoroscopy image, which allows calculation of $a_{contrast}$ coefficient, such as in Eqn. 6.8:

$$I_{angio} = a_{bone}.DRR_{bone} + a_{tissue}.DRR_{tissue} + a_{contrast}.DRR_{vessels} + b \tag{6.8}$$

Image generation process

Figure 6.1 shows an overall illustration of the developed method to generate CT-based synthetic images from one view position. The process can be split up into the five following steps (where the Roman numerals labelling each step correspond to the labelled boxes in the figure):

I. 2D-3D registration: the preoperative CT volume (1st row) was registered to the angiography image I_{angio} (4th row), using the 2D-3D registration system described in Sec. 4.3 (i.e. calculating the transformation M_{angio}, which determines the view position of I_{angio} with respect to $\mathbf{CT}_{3D}$). The angiography image was chosen to allow later calculation of $a_{contrast}$.

II. CT-segmentation: the CT volume was segmented into 3 segmentations: CT_{bone}, CT_{tissue}, and $CT_{vessels}$ (2nd row), using the semi-automatic segmentation option available in ITK-SNAP [Yushkevich et al., 2006]. For CT_{bone}, only voxels with HU value ≥ 200 were included (voxels with HU value < 200 were set to zero). For CT_{tissue}, only voxels with HU value < 200 were included (voxels with HU value ≥ 200 were set to zero). $CT_{vessels}$ only included the aorta in the segmentation.

III. DRR production: 3 DRRs were produced (one from each segmentation) at the registration position: DRR_{bone}, DRR_{tissue}, and $DRR_{vessels}$ (3rd row). All DRRs were generated as described in Sec. 4.3.1 (i.e. by casting rays through the CT segmentation using the transformation M_{angio}, and integrating HU

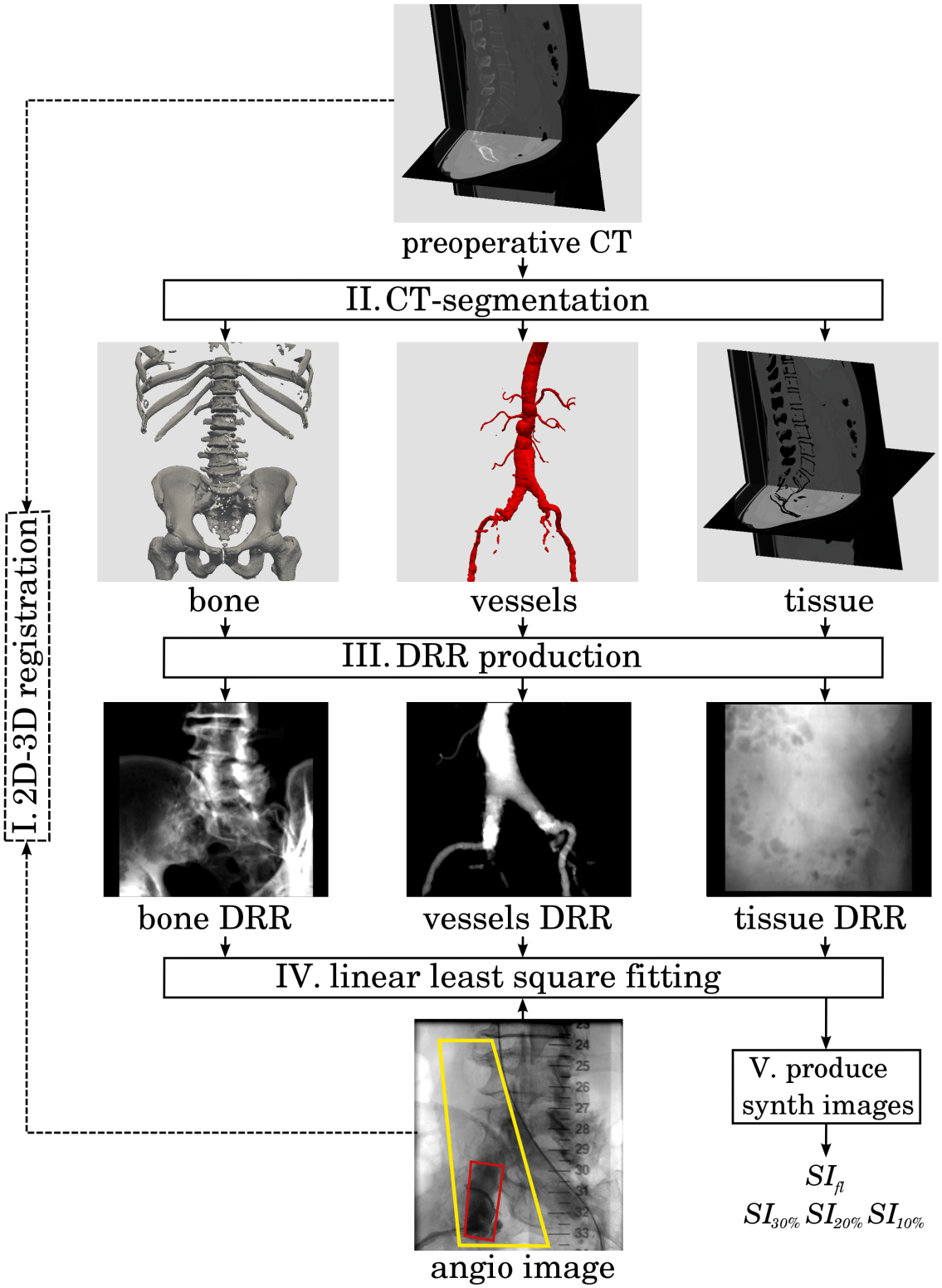

Figure 6.1: Illustration of the employed method to produce synthetic images. The CT is registered to the angiography image, and then segmented into 3 segmentations which are used to produce 3 DRRs at the registration position. The DRRs and angiography image are all input into a linear least square fitting program to calculate the required linear coefficients.

values along the ray path). However, all voxel values along the ray path were integrated for each segmentation instead of choosing a threshold value as in Sec. 4.3.1.

IV. Linear least square fitting: DRR_{bone}, DRR_{tissue}, $DRR_{vessels}$, and I_{angio} were all input into a linear least square fitting program to solve Eqn. 6.8. The developed program allowed the user to place two interactive polygon masks within I_{angio}. The first mask was used to choose ROI_1 where ICM was most homogeneous (marked with red lines), and the second mask was used to choose ROI_2 which included ROI_1, bone, and soft-tissue, but no interventional devices (marked with yellow lines). Eqn. 6.8 was then solved by employing ROI_1 and ROI_2 as follows:

$$I_{angio}^{roi2} = a_{bone}.DRR_{bone}^{roi2} + a_{tissue}.DRR_{tissue}^{roi2} + a_{contrast}.DRR_{vessels}^{roi1} + b \quad (6.9)$$

V. Produce synthetic images: the generated DRR images and the calculated coefficients were combined, as shown in Eqns. 6.10, to produce the following 4 synthetic images (example images are shown in Fig. 6.2):

1. One synthetic fluoroscopy image: SI_{fl} ('a'), where $a_{contrast} = 0$ was used.
2. Three synthetic angiography images: $SI_{30\%}$ ('b'), $SI_{20\%}$ ('c'), and $SI_{10\%}$ ('d'), where 30%, 20%, and 10% of the value of $a_{contrast}$ was used to simulate 30%, 20%, and 10% the amount of the ICM used in standard DSA imaging, respectively.

$$\begin{aligned} SI_{fl} &= a_{bone}.DRR_{bone} + a_{tissue}.DRR_{tissue} + b \\ SI_{30\%} &= a_{bone}.DRR_{bone} + a_{tissue}.DRR_{tissue} + 0.3 \times a_{contrast}.DRR_{vessels} + b \\ SI_{20\%} &= a_{bone}.DRR_{bone} + a_{tissue}.DRR_{tissue} + 0.2 \times a_{contrast}.DRR_{vessels} + b \\ SI_{10\%} &= a_{bone}.DRR_{bone} + a_{tissue}.DRR_{tissue} + 0.1 \times a_{contrast}.DRR_{vessels} + b \end{aligned} \quad (6.10)$$

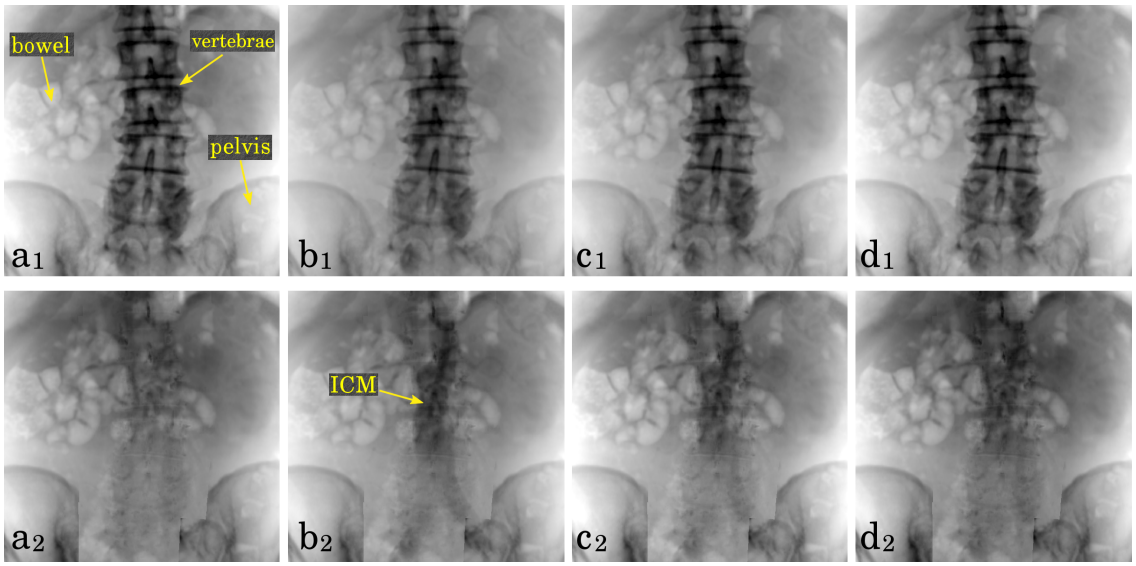

Figure 6.2: An example of the produced synthetic images (top row): a) SI_{fl}, b) $SI_{30\%}$, c) $SI_{20\%}$, and d) $SI_{10\%}$. Images were deboned to show the simulated ICM (bottom row). After deboning, the simulated ICM can be seen in 'b2', slightly seen in 'c2', and hardly seen in 'd2', as the amount of simulated ICM decreased from 30% to 10%.

Moreover, the calculated linear coefficients a_{bone}, a_{tissue}, and $a_{contrast}$, can be used to produce synthetic images from other view positions. This can be achieved by generating new DRRs at the required view position as described in step III, and then combining the DRRs with the calculated linear coefficients as described in step V to produce a new set of SI_{fl}, $SI_{30\%}$, $SI_{20\%}$, and $SI_{10\%}$.

6.3 Introducing Soft-Tissue Motion

Soft-tissue motion occurs during interventional procedures. Sources of such motion depend on the location of the treatment region. In the abdominal region for example, sources of motion include the intestinal peristaltic motion and respiratory motion (which cause DSA imaging artefacts in the abdominal region as discussed in Sec. 2.4.1).

For realistic simulation of the synthetic dataset, soft-tissue motion was introduced to the synthetic images (i.e. SI_{fl}, $SI_{30\%}$, $SI_{20\%}$, and $SI_{10\%}$) at each view position in the simulated 40° C-arm sweep, before de-iDTS reconstruction. This was accomplished by deforming the generated DRR_{tissue} image at each view posi-

tion by different amounts before using Eqn. 6.10 to produce the synthetic images.

Nevertheless, the generated DRR_{tissue} image showed bone silhouette in addition to soft-tissue (Fig.6.3.a). This was because voxels with HU value ≥ 200 (i.e. bone) were set to zero in CT_{tissue}. In order to remove the bone silhouette from the DRR_{tissue} image before deformation, the following steps were taken:

1. A soft-tissue mean HU (i.e. $\overline{HU}_{tissue}$) was calculated from a homogeneous region in CT_{tissue}, such as the liver.

2. Voxels with HU value ≥ 200 (i.e. bone) in CT_{tissue} were set to $\overline{HU}_{tissue}$ instead of zero.

3. A new DRR_{tissue} was generated from the new CT_{tissue}, which does not show the bone silhouette, as seen in Fig.6.3.b.

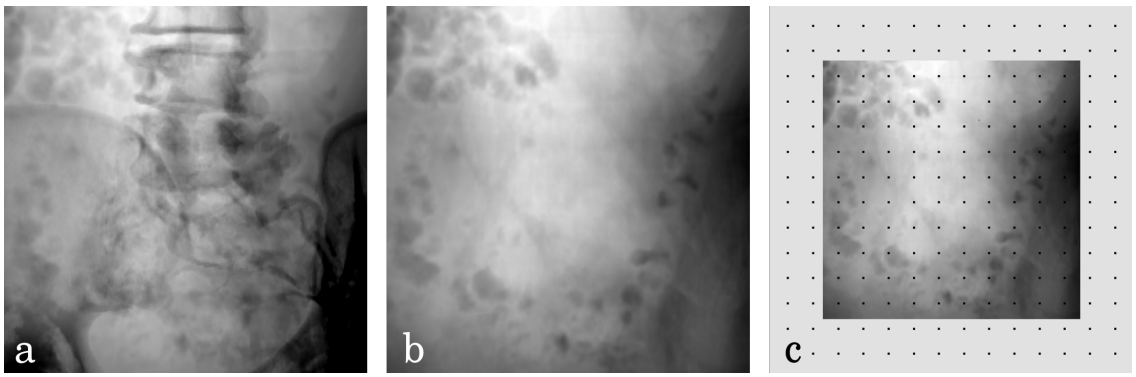

Figure 6.3: The generated DRR_{tissue} where the voxels with HU value ≥ 200 (i.e. bone) in CT_{tissue} were: a) set to zero, and b) set to $\overline{HU}_{tissue}$. c) The B-spline grid overlaid into 'b'.

Deformation method

A random smooth vector field generated from a uniform cubic B-spline grid was used to deform the newly generated DRR_{tissue} (Fig.6.3.b). Only deformation caused by the intestinal peristaltic motion in the abdominal region was simulated. The B-spline grid spacing (i.e. distance between control points as seen in Fig.6.3.c), and the maximum magnitude of deformation were both determined from an angiography sequence (described in the employed data in Sec. 6.5.1), as follows.

The grid spacing (s), was chosen to be equal to the average diameter of features from the large intestine visible in the angiography sequence. The magnitude of the random motion, determined by the B-spline coefficients, was chosen to be equal to the average magnitude of bowel motion, as calculated from the angiography sequence.

The bowel motion cycle observed in the angiography sequence was around 4 sec on average (i.e. the time taken for a landmark in the bowel to return to the starting position was ∼4 sec). A 40° C-arm sweep to acquire 40 images took around 8 sec on average as reported in Sec. 5.3.3. Therefore, 2 cycles of motion deformation were introduced throughout the 40 generated DRR_{tissue} at the 40 simulated view positions (i.e 1 cycle of motion for every 20 DRR_{tissue}). The resulting simulated bowel motion was visually consistent with motion observed from the employed patient's data.

6.4 Adding Quantum-Noise

As mentioned in Sec. 2.3.1, X-ray is usually used in low dose mode to acquire fluoroscopy images as exposure times can be long during interventional procedures. The low dose helps to reduce the radiation exposure for both the patient and the interventional team, especially for complex cases with longer exposure times. As a result, however, final screening images are formed from a very limited number of incident X-ray photons, which causes the primary source of noise in these images to be Poisson noise, also known as "quantum-noise" [Cerciello et al., 2012]. Quantum-noise would still exist at high dose imaging because of the quantum nature of X-ray (i.e. the number of photons reaching the detector during the exposure time will vary even under static setup). However, by increasing the dose, photon fluctuations decrease as the average number of photons reaching the detector increases [Chan et al., 1990].

Other sources of noise exist in the imaging system, these include for example electronic noise, quantization noise, and noise originating from radiation scatter [Chan et al., 1990]. Nevertheless, quantum-noise is the most dominant source of noise in low dose X-ray imaging, thus, other sources of noise can be ignored [Hensel

et al., 2007].

Assuming that the incident X-ray photons follow a Possion distribution, the probability of receiving n_d incident photons at the detector can be described by Eqn. 6.11, where λ is the mean rate of photon arrival [Hensel et al., 2007]:

$$p(n_d) = \frac{\lambda^{n_d}}{n_d!} e^{-\lambda} \tag{6.11}$$

Prior to de-iDTS reconstruction, quantum-noise was added to the synthetic images produced in the previous section (i.e. SI_{fl}, $SI_{30\%}$, $SI_{20\%}$, and $SI_{10\%}$ with soft-tissue motion) at each view position in the simulated 40° C-arm sweep. For this purpose, instead of adding artificial noise to the images, Poisson noise was generated directly from the images, where each pixel intensity was interpreted as the mean of a Poisson distribution (i.e. what the pixel intensity would be if it was randomly produced from a Poisson distribution with a λ equal to the pixel intensity).

6.5 Data and Experiments

In the following, I firstly explain how clinical data was employed to generate the synthetic images to simulate a 40° RAO/LAO sweep. I then describe the experiments conducted with the synthetic dataset. Finally, I describe the validation experiments used.

6.5.1 Employed data

In order to generate the synthetic dataset to simulate a 40° RAO/LAO sweep (i.e. one set of SI_{fl}, $SI_{30\%}$, $SI_{20\%}$, and $SI_{10\%}$ per one degree of rotation as shown in Fig. 6.4), the following data from the second patient described in Sec. 5.2 (who underwent a complex EVAR procedure of the AAA) was employed:

1. The preoperative diagnostic CT scan, which had voxel sizes of $0.77 \times 0.77 \times 0.8\,\text{mm}^3$.

2. An angiography sequence acquired with image dimensions of 1024×1024 pixels, pixel sizes of $0.216 \times 0.216\,\text{mm}^2$, frame rate of 1 fps, 10 frames, and a FoV of 32 cm. The angiography sequence was used to produce an angiography

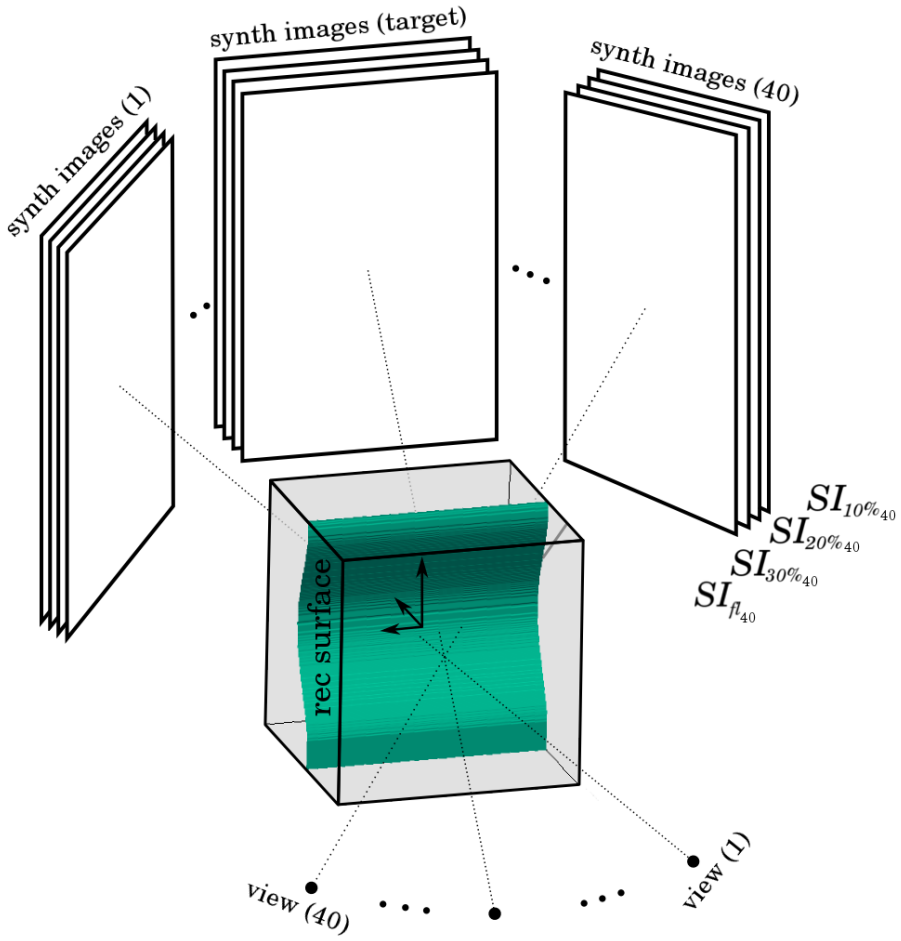

Figure 6.4: The produced synthetic dataset to simulate a 40° RAO/LAO sweep. Four synthetic images were produced at each view position: one synthetic fluoroscopy image (SI_{fl_i}), and three synthetic angiography images with added synthetic contrast to simulate 30%, 20%, and 10% of the ICM amount used in standard DSA imaging ($SI_{30\%_i}$, $SI_{20\%_i}$, and $SI_{10\%_i}$ respectively).

image by employing the minimum intensity projection method, where only pixels with the lowest intensity values throughout the sequence frames were projected into a single image.

3. The 40 view positions of the C-arm (i.e. $M_i = PR_iT_i$, $i = 1, \ldots, 40$), which were calculated by the 2D-3D registration between the sampled fluoroscopy images of the C-arm sweep, and the CT volume (see Sec. 4.4.1).

The CT scan and the produced angiography image were first used to calculate the linear coefficients a_{bone}, a_{tissue}, $a_{contrast}$, and b, by following steps I,II,III, and IV described in the image generation process in Sec. 6.2. Then, for each of the 40 view positions of the C-arm, new DRRs were generated at the current view position (step III in the image generation process), and then combined with the calculated linear coefficients to produce SI_{fl}, $SI_{30\%}$, $SI_{20\%}$, and $SI_{10\%}$ (step V in the image generation process).

6.5.2 Experiments with the synthetic dataset

The curved surface defined in Sec. 5.2.2 (by picking points along the midline of the segmented aorta, iliac and renal arteries, and then producing a surface using thin-plate-spline interpolation), was used for reconstruction as described in Sec. 4.4.2. No iDTS images without bone removal were reconstructed as the beneficial effect of the deboning process (see Sec. 4.4.1) was clearly seen in the previous chapter's results (Sec. 5.3).

Four de-iDTS images were reconstructed from approximately an AP view (i.e. the chosen target image has ∼AP view):

1. The first de-iDTS image was reconstructed using the 40 SI_{fl}, which will be called de-iDTS0%.

2. The second, third, and fourth de-iDTS images were reconstructed using the 40 $SI_{30\%_i}$, 40 $SI_{20\%_i}$, and 40 $SI_{10\%_i}$, which will be called de-iDTS30%, de-iDTS20%, and de-iDTS10%, respectively.

de-iDTS images were reconstructed before and after adding soft-tissue motion and quantum-noise, as illustrated in Fig. 6.5, which shows an overall diagram of the

performed experiments.

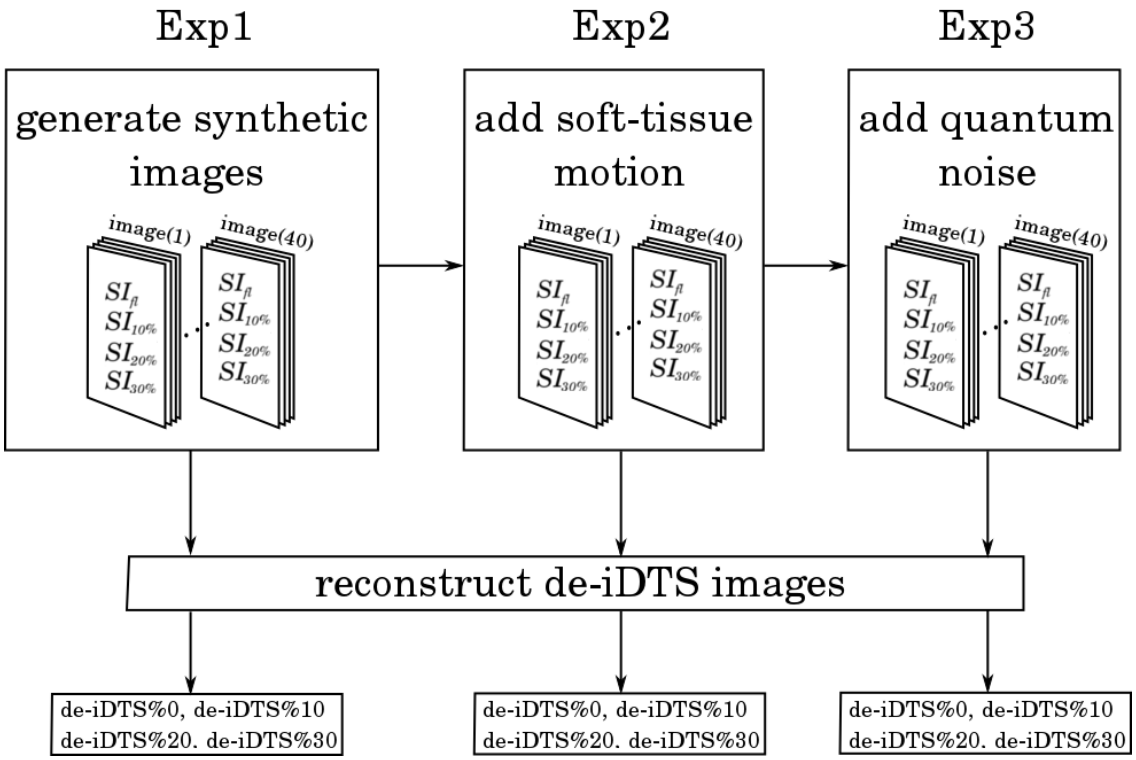

Figure 6.5: An overall diagram of the performed experiments to reconstruct de-iDTS images. For each experiment, the produced synthetic images to simulate a 40° RAO/LAO sweep were used to reconstruct four de-iDTS images: de-iDTS0%, de-iDTS30%, de-iDTS20%, and de-iDTS10%.

6.5.3 Validation experiment

As described in the previous section, for each experiment, the produced synthetic dataset to simulate a 40° RAO/LAO sweep was used to reconstruct four de-iDTS images from approximately an AP view: de-iDTS0%, de-iDTS30%, de-iDTS20%, and de-iDTS10%.

For comparison with images which are also taken from a single view position, the following two images were used (one set for each experiment):

1. The synthetic fluoroscopy target image ($SI_{fl_{(T)}}$), which does not include any simulated ICM.

2. A synthetic DSA image ($SI_{DSA_{(T)}}$), which was also produced at the target view position.

$SI_{fl_{(T)}}$ was already available in the synthetic dataset produced for each experiment. However, $SI_{DSA_{(T)}}$ had to be produced for each experiment as follows.

Producing synthetic DSA images

For the first experiment, 10 synthetic angiography images (same number of angiography frames reported in the employed data) with a 100% simulated contrast were produced at the target view position using Eqn. 6.12. A minimum intensity projection was then used throughout the 10 $SI_{100\%_{(T)}}$. Finally, the minimum intensity angiography image was subtracted, pixel by pixel, from $SI_{fl_{(T)}}$ (mask image as it contains no ICM) to generate $SI_{DSA_{(T)}}$.

$$SI_{100\%_{(T)}} = a_{bone}.DRR_{bone_{(T)}} + a_{tissue}.DRR_{tissue_{(T)}} + a_{contrast}.DRR_{vessels_{(T)}} + b \quad (6.12)$$

In order to add soft-tissue motion to $SI_{DSA_{(T)}}$ for the second experiment validation, the same deformation method explained in Sec. 6.3 was used. This included deforming the 10 $DRRs_{tissue_{(T)}}$ (without the bone silhouette) by different amounts before using Eqn. 6.12 to produce 10 $SI_{100\%_{(T)}}$ with motion deformation. 2.5 cycles of motion deformation were introduced throughout the 10 $DRRs_{tissue_{(T)}}$ (as the angiography sequence reported in the employed data took 10 sec). The 10 $SI_{100\%_{(T)}}$ with motion deformation were then minimum intensity projected and subtracted from $SI_{fl_{(T)}}$ to produce $SI_{DSA_{(T)}}$ with peristaltic motion artefacts.

For the third experiment validation, quantum-noise was added to each of the 10 $SI_{100\%_{(T)}}$ (which had soft-tissue motion) using the same method described in Sec. 6.4. The 10 $SI_{100\%_{(T)}}$ were then minimum intensity projected and subtracted from $SI_{fl_{(T)}}$ to produce $SI_{DSA_{(T)}}$ with peristaltic motion and quantum-noise artefacts.

Using signal difference to noise ratio (SDNR)

For each experiment, SDNRs were calculated using two PLs across clinically relevant locations: the left and right renal ostia.

For each SDNR calculation, $SI_{DSA_{(T)}}$, de-iDTS30%, de-iDTS20%, and de-iDTS10% were all input into the same program described in Sec. 5.2.3, which allowed manual placement of the PL. The manually placed PL was positioned inside $SI_{DSA_{(T)}}$, then the same position was used to place PLs inside the rest of the images. Moreover, three calculations for each PL (which increased the consistency of the SDNR calculations) were made: one directly on the PL, and two others with the PL shifted horizontally by ±3 pixels as illustrated in Fig. 6.6.

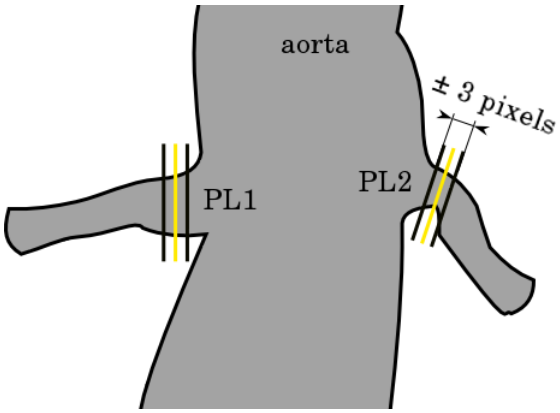

Figure 6.6: Method to calculate SDNR using a profile line (PL) across the renal ostia. For each PL, three calculations were made, one directly on the PL and two others with the PL shifted horizontally by ±3 pixels.

6.6 Results

As explained in the image generation process in Sec. 6.2, an angiography image (I_{angio}) was employed to calculate the required linear coefficients by using the linear least square fitting method. The coefficients were then used to produce a set of synthetic images (SI_{fl}, $SI_{30\%}$, $SI_{20\%}$, and $SI_{10\%}$) at the I_{angio} view position. Figure 6.7 demonstrates the linear relationship between images I_{angio} ('a') & SI_{fl} ('b') for the ROI marked with the yellow lines. The ROI was chosen not to include any interventional devices nor ICM in I_{angio}.

Using the employed data described in Sec. 6.5.1, 40 sets of synthetic images (one set at each view position) were produced before de-iDTS reconstruction. In the following results sections, and for each experiment, I show:

- An example of the produced synthetic images at the target view position.

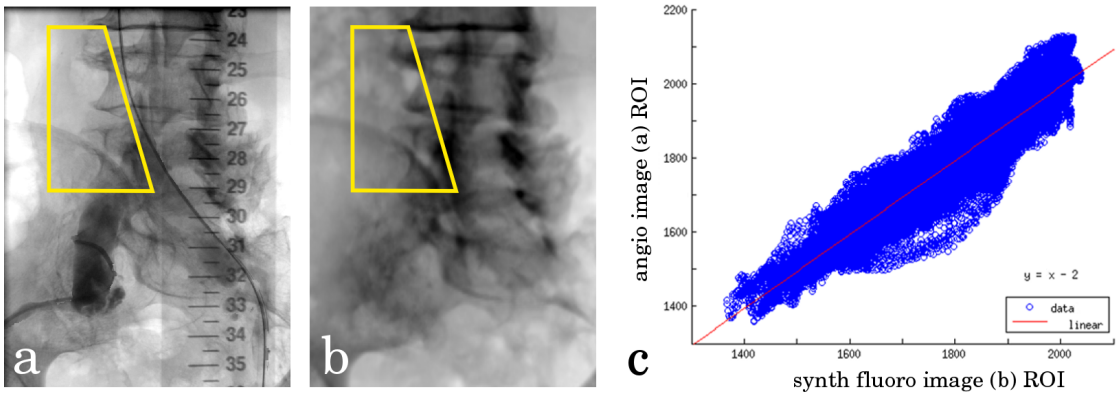

Figure 6.7: A scatter plot between: a) the angiography image (I_{angio}) which was employed to calculate the required linear coefficients for simulation, and b) the produced synthetic fluoroscopy image (SI_{fl}) at I_{angio} view position. The scatter plot shows the data values inside the ROI marked with the yellow lines, and it shows the calculated best fit line.

This includes: a) $SI_{fl_{(T)}}$, b) $SI_{30\%_{(T)}}$, c) $SI_{20\%_{(T)}}$, and d) $SI_{10\%_{(T)}}$, before (top row) and after (bottom row) deboning.

- The validation synthetic images which were produced at the target view position: a) $SI_{fl_{(T)}}$, and b) $SI_{DSA_{(T)}}$, and the four de-iDTS images: c) de-iDTS0%, d) de-iDTS30%, e) de-iDTS20%, and f) de-iDTS10%, which were reconstructed from an ∼AP view.

In addition, the SDNR values (calculated across the two PLs shown in Fig. 6.6), for all the experiments are presented and plotted for comparison.

6.6.1 Simulation and reconstruction results using contrast enhanced synthetic fluoroscopy images

Figure 6.8 shows the produced synthetic images at the target view position, before (top row) and after (bottom row) deboning. The simulated ICM in 'b1', 'c1', and 'd1' cannot be distinguished from the overlaying high contrast vertebrae. However, after removing the vertebral bone as shown in the bottom row, the simulated ICM can be seen in 'b2', slightly seen in 'c2', and hardly seen in 'd2', as the amount of simulated ICM decreased from 30% to 10%.

Figure 6.9 shows the validation synthetic images produced at the target view

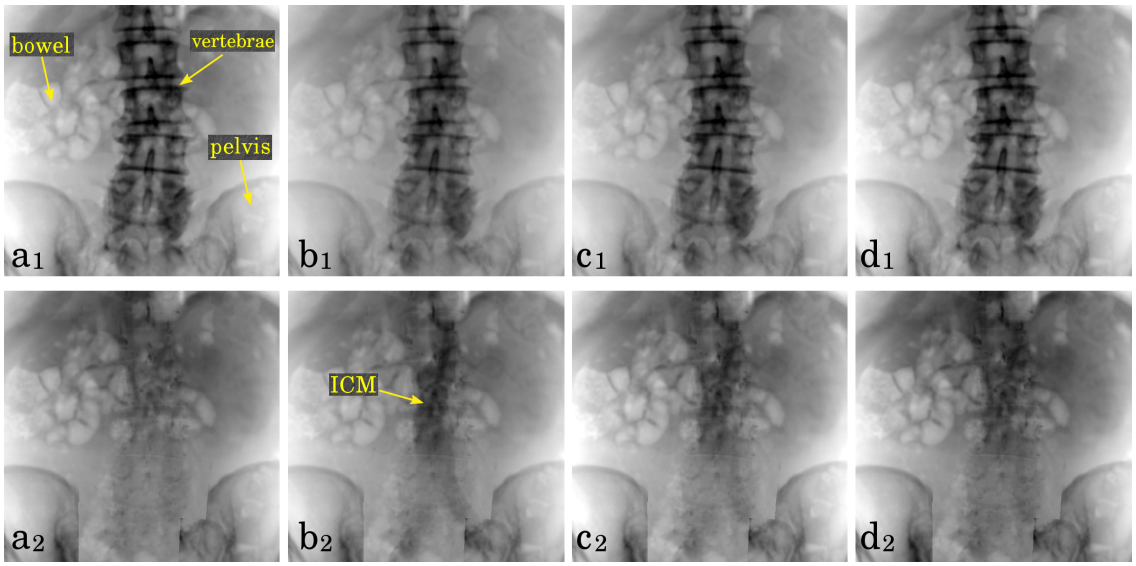

Figure 6.8: The produced synthetic images at the target view position for the first experiment: a) $SI_{fl_{(T)}}$, b) $SI_{30\%_{(T)}}$, c) $SI_{20\%_{(T)}}$, and d) $SI_{10\%_{(T)}}$, before (top row) and after (bottom row) deboning. After the deboning process, the simulated ICM can be seen in 'b2', slightly seen in 'c2', and hardly seen in 'd2', as the amount of simulated ICM decreased from 30% to 10%.

position, and the reconstructed de-iDTS images from an ∼AP view using the curved surface defined in Sec. 5.2.2. In addition, for images 'b', 'c', 'd', 'e', and 'f', the region inside the yellow box is magnified to examine the renal ostia.

In 'a', no features from the aorta are visible. 'b' shows the ICM enhanced aorta, with the renal ostia and bifurcation clearly visible. The background structures are completely subtracted in 'b' as no soft-tissue motion existed. The reconstructed image 'c' shows parts of the aortic outline and some calcium (marked with arrows), but not the renal ostia nor the bifurcation. However, in 'd', 'e', and 'f', the entire aortic outline can be clearly seen with the renal ostia, bifurcation, and some calcium. In 'f', nevertheless, the renal ostia and bifurcation are much less visible as the simulated ICM decreased to 10%.

6.6.2 Simulation and reconstruction results after introducing soft-tissue motion

Figure 6.10 shows the same synthetic images illustrated in Fig. 6.8. However, in Fig. 6.10, soft-tissue motion was introduced to the synthetic images as described in

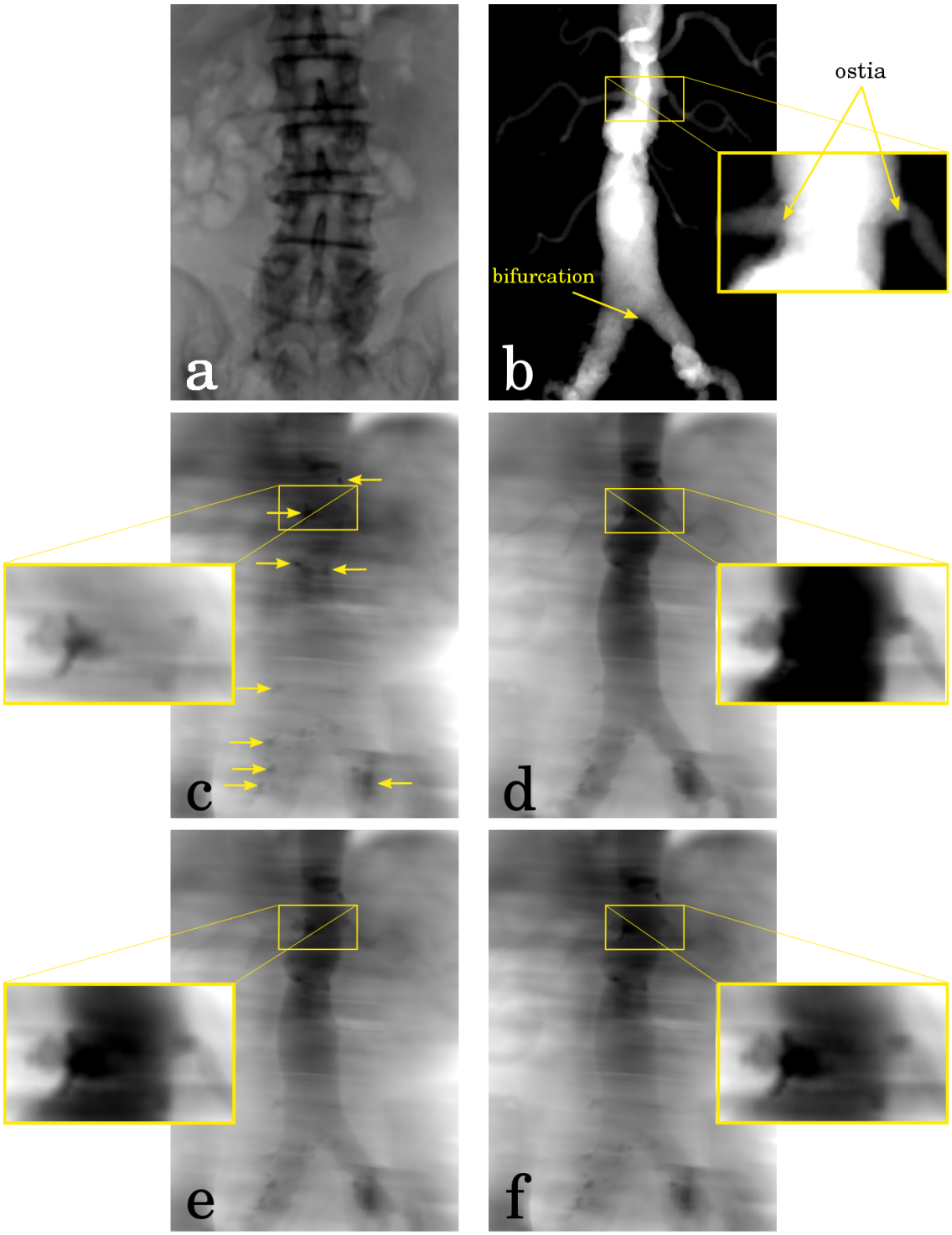

Figure 6.9: The validation synthetic images: a) $SI_{fl_{(T)}}$, b) $SI_{DSA_{(T)}}$, and the reconstructed de-iDTS images from an ∼AP view for the first experiment c) de-iDTS0%, d) de-iDTS30%, e) de-iDTS20%, and f) de-iDTS10%. The region inside the yellow box is magnified to examine the renal ostia. Arrows in 'c' indicate calcium deposits.

Sec. 6.3. An example of soft-tissue deformation can be clearly seen in 'a1', where the outline of part of the bowel is highlighted after (yellow contour), and before (red

contour) introducing deformation. The yellow and red contours are not aligned due to soft-tissue motion.

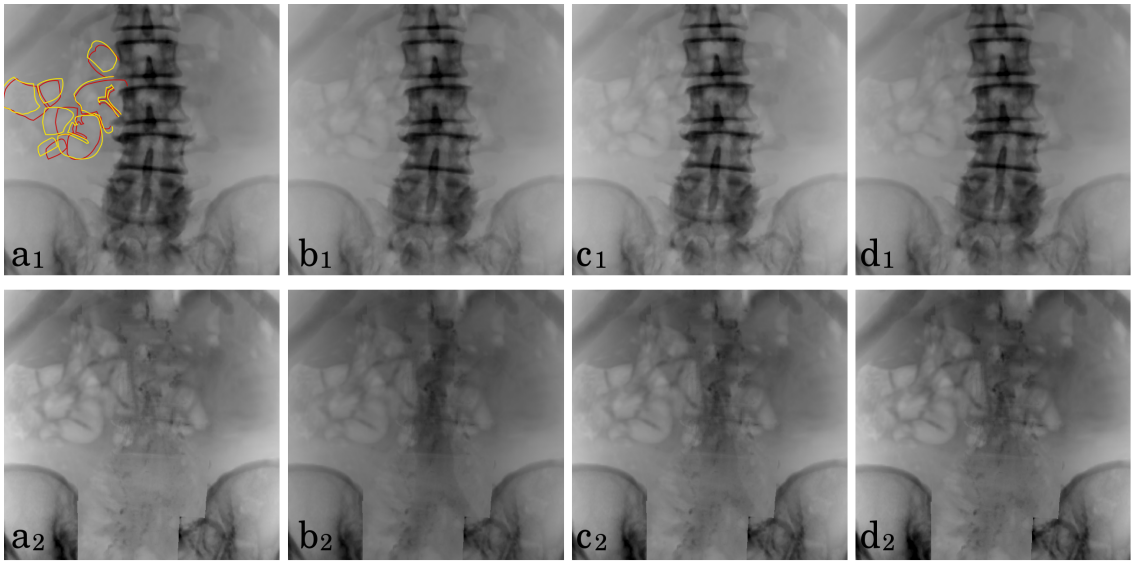

Figure 6.10: The produced synthetic images at the target view position for the second experiment: a) $SI_{fl_{(T)}}$, b) $SI_{30\%_{(T)}}$, c) $SI_{20\%_{(T)}}$, and d) $SI_{10\%_{(T)}}$, before (top row) and after (bottom row) deboning. The shown images are similar to the ones shown in Fig. 6.8. However, the shown images include soft-tissue motion. To illustrate motion deformation, in 'a1', the outline of part of the bowel was highlighted before (red contour), and after (yellow contour) introducing deformation. The contours are clearly not aligned due to soft-tissue motion.

Figure 6.11 shows the same images illustrated in Fig. 6.9. However, in Figure 6.11, soft-tissue motion was introduced to the synthetic images before producing $SI_{DSA_{(T)}}$, and reconstructing the de-iDTS images. Results are similar to the images shown in Fig. 6.9. However, in 'b', background structures are not completely subtracted due to soft-tissue motion. This resulted in motion artefacts which reduced the image quality and made the ostia less visible in 'b'. In addition, the renal ostia in 'f' can be hardly seen.

6.6.3 Simulation and reconstruction results after adding quantum-noise

Figure 6.12 shows the same synthetic images illustrated in Fig. 6.10 which included soft-tissue motion. However, in Fig. 6.12, quantum-noise was also added to the

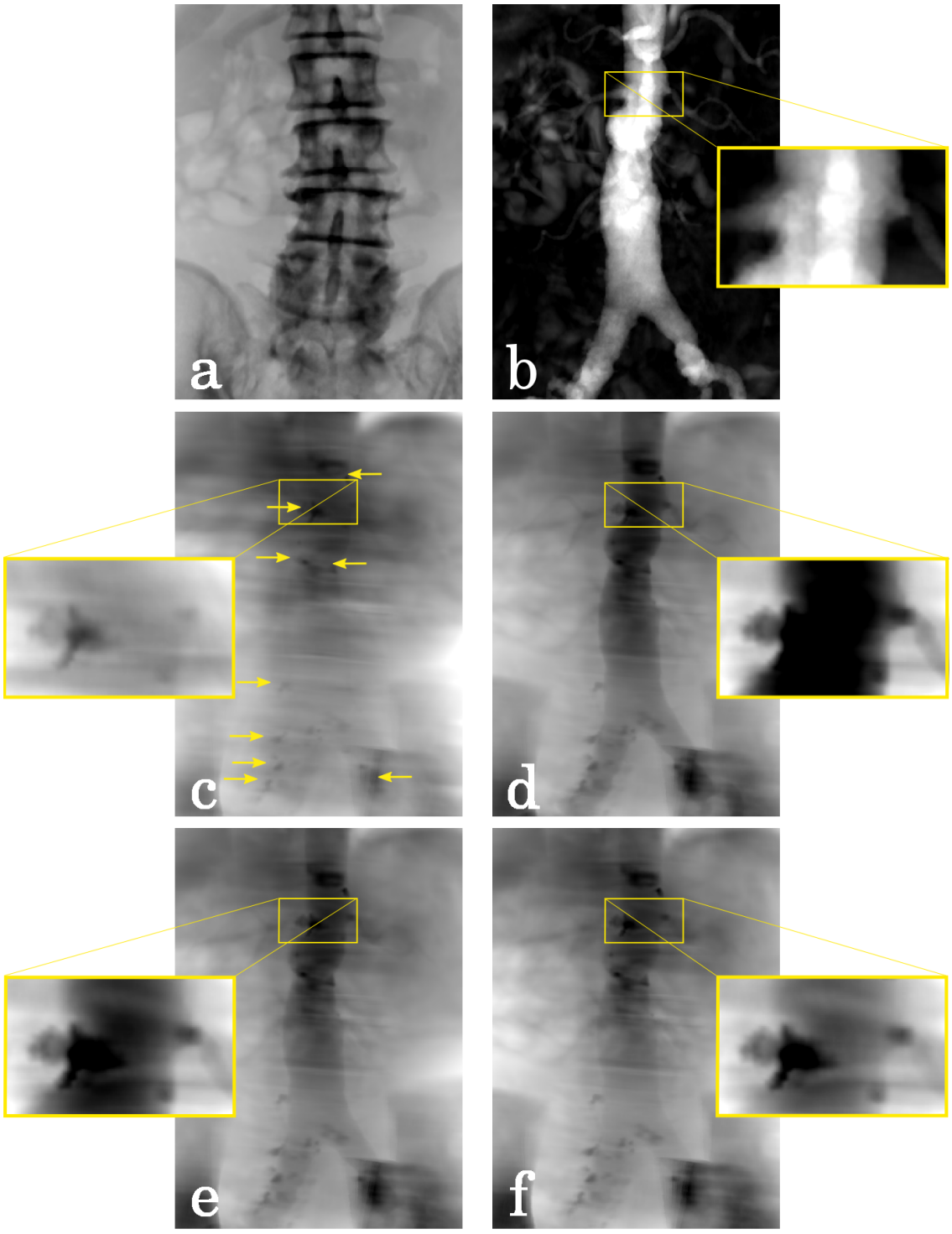

Figure 6.11: The validation synthetic images: a) $SI_{fl_{(T)}}$, b) $SI_{DSA_{(T)}}$, and the reconstructed de-iDTS images from an ∼AP view for the second experiment: c) de-iDTS0%, d) de-iDTS30%, e) de-iDTS20%, and f) de-iDTS10%. The region inside the yellow box is magnified to examine the renal ostia. Arrows in 'c' indicate calcium deposits.

synthetic images as described in Sec. 6.4. The effect of adding quantum-noise can be seen in image 'a1', where a ROI is magnified after (yellow box), and before (red box) adding quantum-noise.

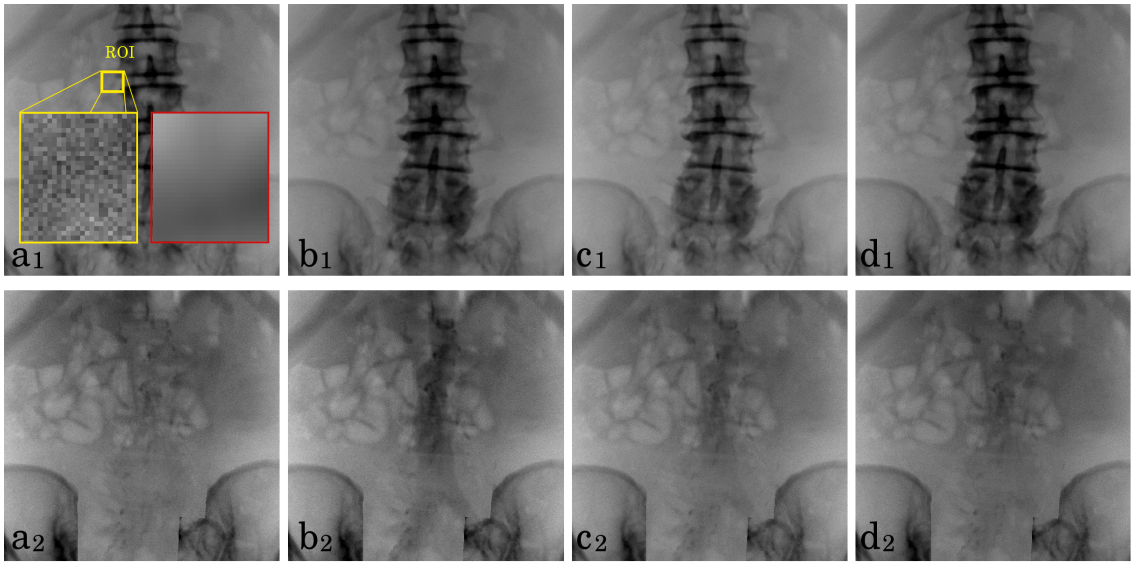

Figure 6.12: The produced synthetic images at the target view position for the third experiment: a) $SI_{fl_{(T)}}$, b) $SI_{30\%_{(T)}}$, c) $SI_{20\%_{(T)}}$, and d) $SI_{10\%_{(T)}}$, before (top row) and after (bottom row) deboning. Shown images are similar to the ones shown in Fig. 6.10 which included soft-tissue motion. However, shown images include quantum-noise. To illustrate the effect of adding quantum-noise, in 'a1', a ROI was magnified before (red box), and after (yellow box) adding noise.

Figure 6.13 shows the same images illustrated in Fig. 6.11 which included soft-tissue motion. However, in Figure 6.13, quantum-noise was added to the synthetic images before producing $SI_{DSA_{(T)}}$, and reconstructing the de-iDTS images. Results are similar to the images shown in Fig. 6.11. However, in 'b', in addition to motion artefacts, noise artefacts can also be seen which degraded the image quality further, and made the ostia even less visible. In addition, the renal ostia can be hardly seen in 'e', and cannot be seen in 'f'.

6.6.4 SDNR results

Table 6.1 lists the SDNR results for each experiment, using the two PLs across the left and right renal ostia (illustrated in Fig. 6.6) in images: 'b', 'd', 'e', and 'f'. The percentage decrease in SDNR values for the second and third experiments

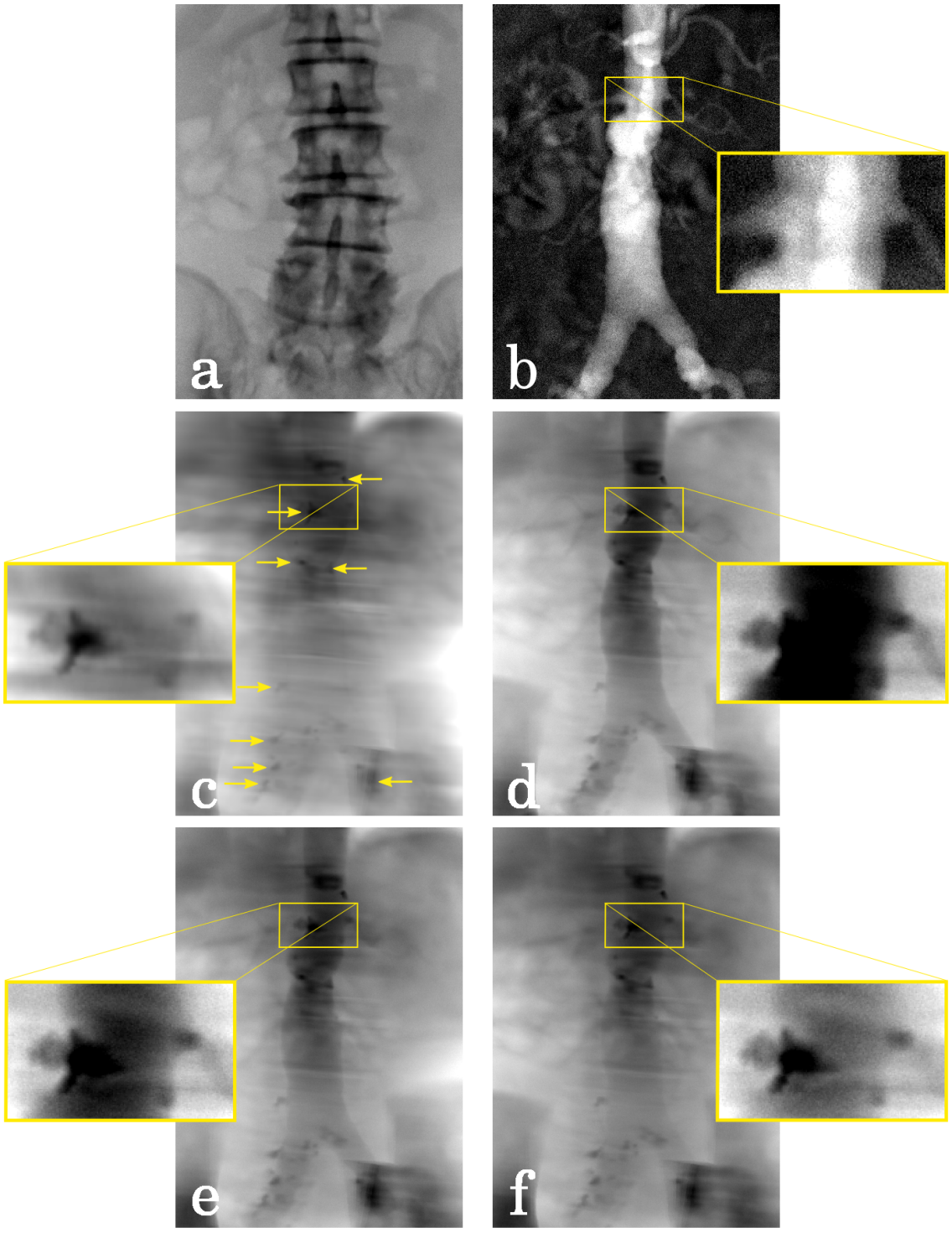

Figure 6.13: The validation synthetic images: a) $SI_{fl_{(T)}}$, b) $SI_{DSA_{(T)}}$, and the reconstructed de-iDTS images from an ∼AP view for the third experiment: c) de-iDTS0%, d) de-iDTS30%, e) de-iDTS20%, and f) de-iDTS10%. The region inside the yellow box is magnified to examine the renal ostia. Arrows in 'c' indicate calcium deposits.

(compared to the first experiment) is also presented in brackets. In addition, for visual comparison of results before and after introducing soft-tissue motion and

quantum-noise, SDNR values are plotted for each PL as seen in Fig. 6.14.

By examining Fig. 6.14, it can be seen that SDNR values decreased for all images after introducing motion, and decreased further after adding noise. However, for $SI_{DSA_{(T)}}$, the percentage decrease is much more substantial when compared to the de-iDTS results due to motion and noise artefacts (for example, for PL1, the SDNR value decreased by -41.49% and -60.67% for $SI_{DSA_{(T)}}$; whereas it only decreased by -2.31% and -5% for de-iDTS30%). Therefore, even though $SI_{DSA_{(T)}}$ had the highest SDNR values in the first experiment, after adding motion and noise, $SI_{DSA_{(T)}}$ scored the lowest SDNR values compared to all other images.

Furthermore, for each experiment, it can be observed that as the amount of simulated ICM in the de-iDTS images decreased, the corresponding SDNR value decreased as well (for example, for PL1 in the first experiment, the SDNR values for images 'd', 'e', and 'f' are 2.60, 2.31, and 1.96, respectively)

Table 6.1: SDNR results for each experiment using the two PLs shown in Fig. 6.6. The percentage decrease in SDNR values for the second and third experiments (compared to the first experiment) is also presented in brackets.

		$SI_{DSA_{(T)}}$ (b)	de-iDTS30% (d)	de-iDTS20% (e)	de-iDTS10% (f)
Exp1	LP1	4.17	2.60	2.31	1.96
	LP2	5.31	3.60	3.37	2.99
Exp2	LP1	2.44 **(-41.49%)**	2.54 **(-2.31%)**	2.30 **(-0.43%)**	1.93 **(-1.53%)**
	LP2	3.87 **(-27.12%)**	3.40 **(-5.56%)**	2.97 **(-11.87%)**	2.75 **(-8.03%)**
Exp3	LP1	1.64 **(-60.67%)**	2.47 **(-5%)**	2.22 **(-3.9%)**	1.91 **(-2.55%)**
	LP2	2.01 **(-62.15%)**	3.07 **(-14.72%)**	2.75 **(-18.4%)**	2.41 **(-19.4%)**

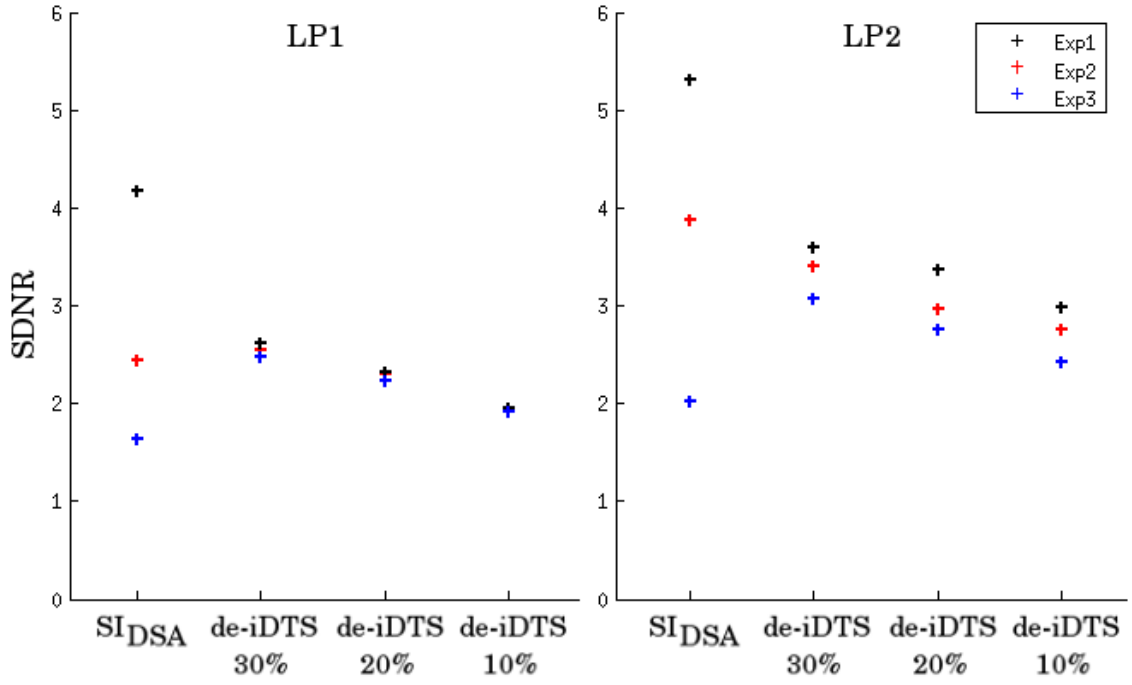

Figure 6.14: Plot of calculated SDNR values for all experiments for visual comparison before (black crosses) and after introducing soft-tissue motion (red crosses) and quantum-noise (blue crosses).

6.7 Discussion

A novel technique: "interventional digital tomosynthesis facilitated by 2D-3D image registration" has been proposed in the previous chapter (Ch. 5). Clinical results presented in Ch. 5.3.2 showed that de-iDTS was able to enhance the aortic outline and calcium deposits without the injection of any ICM, and with much reduced radiation dose compared to DSA imaging. The injection of ICM in DSA imaging, however, enables much smaller vascular structures, such as the renal ostia, to be seen. Nevertheless, ICM is nephrotoxic and must be used sparingly during the intervention (see Sec. 2.4.1).

The aim of this chapter was to extend the proposed de-iDTS method in Ch. 5 by injecting ICM during the C-arm sweep to enhance small vascular structures visualization, such as the renal ostia. The proposed amount of ICM to be injected was only 10-30% the amount used in standard DSA imaging. To avoid acquiring a new clinical dataset with additional nephrotoxic ICM injection, a CT-based synthetic dataset was produced using one of the available clinical datasets in Ch. 5.

The main difficulties were to generate realistic synthetic fluoroscopy images, and then to determine the amount of simulated ICM to be added to produce realistic synthetic angiography images.

Reconstruction results after adding soft-tissue motion and quantum-noise showed that the renal ostia can only be clearly seen with added synthetic contrast to simulate 30% of the ICM amount used in standard DSA imaging.

The produced synthetic DSA image ($SI_{DSA_{(T)}}$) with motion and noise artefacts (Fig. 6.13.b), was of much better quality compared to clinical DSA images (see Fig. 2.5). Unlike clinical angiography images, the employed synthetic angiography images to produce $SI_{DSA_{(T)}}$ contained simulated contrast in the entire aorta. Nevertheless, $SI_{DSA_{(T)}}$ with motion and noise artefacts had the lowest SDNR values compared to de-iDTS30%, de-iDTS20%, and de-iDTS10%.

The simulated ICM was added homogeneously inside the entire aorta to produce the synthetic angiography images during the simulated C-arm sweep. However, clinical angiography images show ICM flow over time after the injection of an ICM bolus. Thus, images in an angiography sequence contain ICM only in some parts of the aorta. After background subtraction, a DSA image can then be produced by using the maximum intensity projection method, which ensures all parts of the aorta containing ICM are projected into a single image (see Sec. 2.4.1). If an ICM bolus is injected during the 40° C-arm sweep, the de-iDTS image will be reconstructed from images containing partial ICM in the aorta. Thus, to ensure that all images of the sweep contain ICM in the entire aorta, a slow constant injection of ICM is required during the duration of the sweep. This might however require more ICM injection than what was estimated (i.e. >30%) as the C-arm sweep takes currently around 8 sec on average as reported in Sec. 5.3.3. Nevertheless, if the de-iDTS technique became incorporated with fluoroscopy systems where only one image per one degree of rotation is acquired at a high frame rate, the C-arm sweep will take a shorter time (e.g. if images are acquired at 10 fps, the sweep will take around 4 sec depending on the C-arm speed limitation).

Only the intestinal peristaltic motion in the abdominal region was simulated when introducing soft-tissue motion, but not respiratory motion. However, during the C-arm sweep, similarly to DSA imaging, patients can be asked to hold their

breath if they are under regional or local anaesthesia, or the ventilator can be switched off if patients are under general anaesthesia.

6.8 Conclusions

In conclusion, the novel de-iDTS technique proposed in Ch. 5 was extended to enable much smaller vascular structures, such as the renal ostia, to be seen. This was achieved by producing CT-based synthetic fluoroscopy images to simulate a 40° C-arm sweep. Synthetic contrast was then added to simulate 10-30% the amount of ICM used in standard DSA imaging before de-iDTS reconstruction. In addition, soft-tissue motion and quantum-noise were added to produce realistic synthetic images before de-iDTS reconstruction. Numerical results after adding motion and noise showed that all reconstructed de-iDTS images with simulated contrast had better SDNR values compared to the produced synthetic DSA image. Reconstructed de-iDTS images showed that the renal ostia can be clearly seen after adding motion and noise when using 30% simulated ICM.

Chapter 7

DSA Remapping Facilitated by 2D-3D Registration on a Standard Fluoroscopy System

Contents

7.1 Introduction

As discussed in Sec. 2.4.1, DSA imaging is still the gold-standard technique to enhance vascular visualisation during EIGS. This includes injecting ICM into the blood vessels of interest, and employing a significantly higher X-ray dose than standard fluoroscopy screening. After background structures are removed to produce a DSA image, the image can be superimposed onto live fluoroscopy images as a roadmap to provide a reference in the absence of ICM.

However, the produced DSA image is only useful as a roadmap for the current C-arm position, and once the C-arm is moved (translated and/or rotated), the DSA image does not correspond to the new interventional view any more because of the projection nature of X-ray. For this reason, during most procedures, a new DSA image will be produced if accurate vascular information is required after C-arm movement.

ICM usage is key during interventional procedures, but nevertheless, ICM causes the main life-threatening complication in EIGS: acute kidney injury. DSA imaging was also found to be a major contributor to the patient radiation dose (81% reported) during endovascular interventions (see Sec. 2.4.1).

New imaging techniques to reduce the need for repeated DSA, thus subsequently reducing the volume of nephrotoxic ICM and radiation exposure are required [Bicknell, 2013, Patel et al., 2013]. This is particularly significant for patients with renal insufficiency, where ICM increases mortality rates and adverse events, and for patients at high risk of radiation adverse response such as patients with a previous high dose from an earlier treatment.

Techniques to reduce repeated DSA mainly include using 2D-3D registration algorithms to provide a 3D preoperative overlay onto the 2D intraoperative fluoroscopy images during EIGS, as illustrated in Fig. 2.7 in Sec. 2.4.2. However, there are issues with non-rigid intraoperative vascular deformation as discussed in more detail in Sec. 3.3.4.

This chapter extends the preliminary work presented in Alhrishy et al. [2015b].

In this chapter, I propose employing the same 2D-3D rigid registration system described in Sec. 4.3 to facilitate DSA remapping using standard hardware during EIGS interventions. The chapter begins by providing a brief overview of the nature of projection X-ray, and the problem of remapping projection data. Then, the proposed novel method to reduce the need for repeated DSA imaging and the process of DSA remapping are explained. Finally, experiments are described, and results are presented using datasets from 9 patients.

7.2 The Projection Nature of X-ray

Because of the pinhole geometry employed in projection X-ray, structures at different depths along the beam path move in relation to each other when projected from different views.

This can be clearly illustrated in the case of the vertebrae and aorta seen in Fig. 7.1. Both images 'a' and 'b' show $DRR_{vessels}$ overlaid onto DRR_{bone} in a red colour after registering the CT volume with the C-arm (DRRs were produced as described in Sec. 6.2, i.e. by using $CT_{vessels}$ and CT_{bone} segmentations). However, in 'b', the C-arm was translated -50 mm in the Y direction (see Fig. 3.3). As a result, the renal ostium position in 'a' (marked with a yellow dot), has changed in 'b' with respect to L1 (marked with a dashed white box).

Therefore, when a new fluoroscopy image is acquired after a C-arm movement (translation in this example), the vasculature position with respect to a specific bony landmark in the previous roadmap (renal ostium position with respect to L1 in this example) cannot be used to remap the aorta roadmap into the new fluoroscopy image.

7.3 The Problem of Remapping Projection Data

Figure 7.2 illustrates the geometry of X-ray perspective projection in 2D. In both images 'a' and 'b', the X-ray source and detector move around the patient from view 1 to view 2 to acquire a new 2D projection image.

As shown in 'a', remapping an image from the first view into the second view

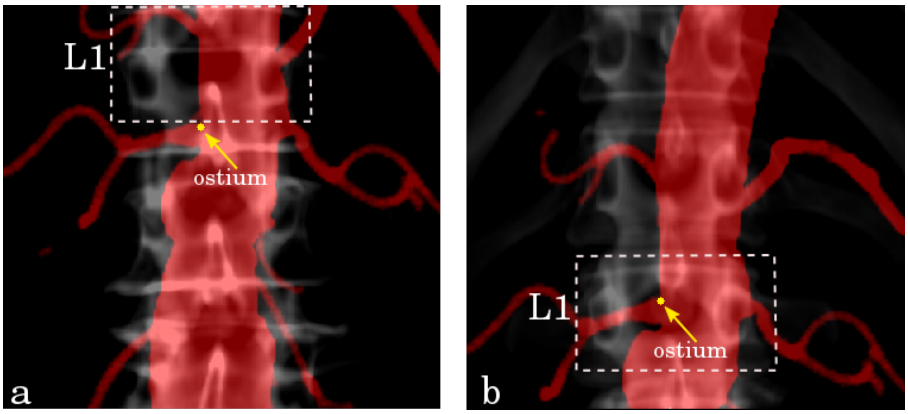

Figure 7.1: An example of the relative motion of structures at different depths, when X-ray projected from different views. a) $DRR_{vessels}$ was overlaid onto DRR_{bone} in a red colour from an AP view. b) The same DRRs but produced after translating the C-arm -50 mm in the Y direction. In both images, the renal ostium is identified with a yellow dote, while the L1 vertebra is identified with a dashed white box. It is clear that the renal ostium position with respect to L1 has changed (by approximately half the hight of the L1 vertebra) as a result of the C-arm translation.

direction cannot be accurately achieved using only knowledge about view directions 1 and 2. Additional knowledge is required: information on the depth position (distance along ray path) of the anatomical features of interest inside the patient. In 'a', the grey circle inside the patient is projected into the detector along the blue line using the first view direction. However, when the source is moved to the second view direction, the blue circle cannot be remapped to view 2 without extra information on the grey circle's position inside the patient. This is because the blue circle might be projected from any point along the blue line intersection with the patient, such as the points marked with +, which if used for remapping along the red lines will result in multiple possible locations of the red circle on view 2.

If all the 2D image information can be projected back from the first view direction into a single accurately known 2D surface, such as the one depicted in 'b', then the image can be remapped accurately into the second view. In 'b', the projected blue square, triangle, and circle using view 1 can be correctly remapped to view 2 using the position information provided by the remapping surface intersecting these features inside the patient. However, as the depth information becomes more three-dimensional (i.e. does not just originate from a single 2D remapping surface), and

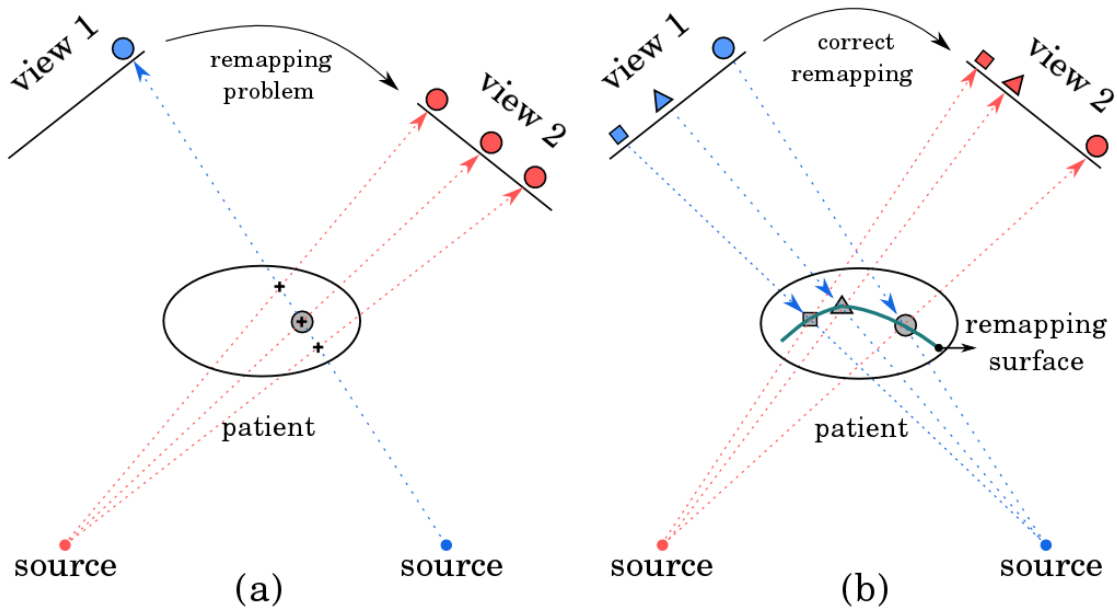

Figure 7.2: The problem of remapping projection data. a) The 2D blue circle cannot be remapped from view 1 to view 2 without knowing its 3D position (i.e. grey circle) along the blue ray path. b) If a remapping surface is known, the blue square, triangle, and circle can be correctly remapped from view 1 to view 2.

as errors arise in positioning the 2D surface, then errors will occur in the remapping process.

The ability to define such a surface accurately is essential for a correct perspective projection remapping. I propose defining a remapping surface inside the preoperative CT volume and then matching this surface to the patient using 2D-3D registration during intervention. This surface is then used to remap a DSA image to a new view direction as will be described in the next section.

7.4 Materials and Methods

The novelty of this method lies in the use of the previously described 2D-3D registration in Sec. 4.3, to facilitate DSA remapping using standard fluoroscopy hardware. In the following, I detail how this can be achieved, and describe the expected types of remapping errors.

7.4.1 Using the 2D-3D registration to facilitate DSA remapping

Figure 7.3 demonstrates how the 2D-3D registration algorithm enables DSA remapping to occur on a standard fluoroscopy system. This begins at the top with the input images:

a) The DSA mask.

b) The DSA image (I_{DSA}), which is produced from an AP view using the DSA mask 'a'.

c) The new fluoroscopy image (I_{FL}), which is acquired after the C-arm has moved from the view position of the DSA image.

d) The preoperative CT scan with the remapping surface defined inside

Images 'a', 'c', and 'd' are input into the 2D-3D registration algorithm which calculates the transformation matrices between the CT scan $(x, y, z, 1)^T$ and both the DSA image $(u, v, 1)^T_{DSA}$ and the new fluoroscopy image $(u, v, 1)^T_{FL}$, such as in Eqn. 7.1 and Eqn. 7.2:

$$M_{DSA}(x, y, z, 1)^T = \lambda(u, v, 1)^T_{DSA} \tag{7.1}$$

$$M_{FL}(x, y, z, 1)^T = \lambda(u, v, 1)^T_{FL} \tag{7.2}$$

The three boxes in Fig. 7.3 show the subsequent stages to the 2D-3D registration, which provide the necessary information to carry out DSA remapping. The Roman numerals labelling each box correspond to the following processes:

I. Calculate DSA view position: the transformation M_{DSA} to position I_{DSA} in relation to $\mathbf{CT}_{3D}$ is determined using the DSA mask. Both the DSA mask and DSA image have the same transformation as they are acquired in a single angiography sequence from the same view direction.

II. Calculate new fluoroscopy view position: the transformation M_{FL} to position I_{FL} in relation to $\mathbf{CT}_{3D}$ is determined.

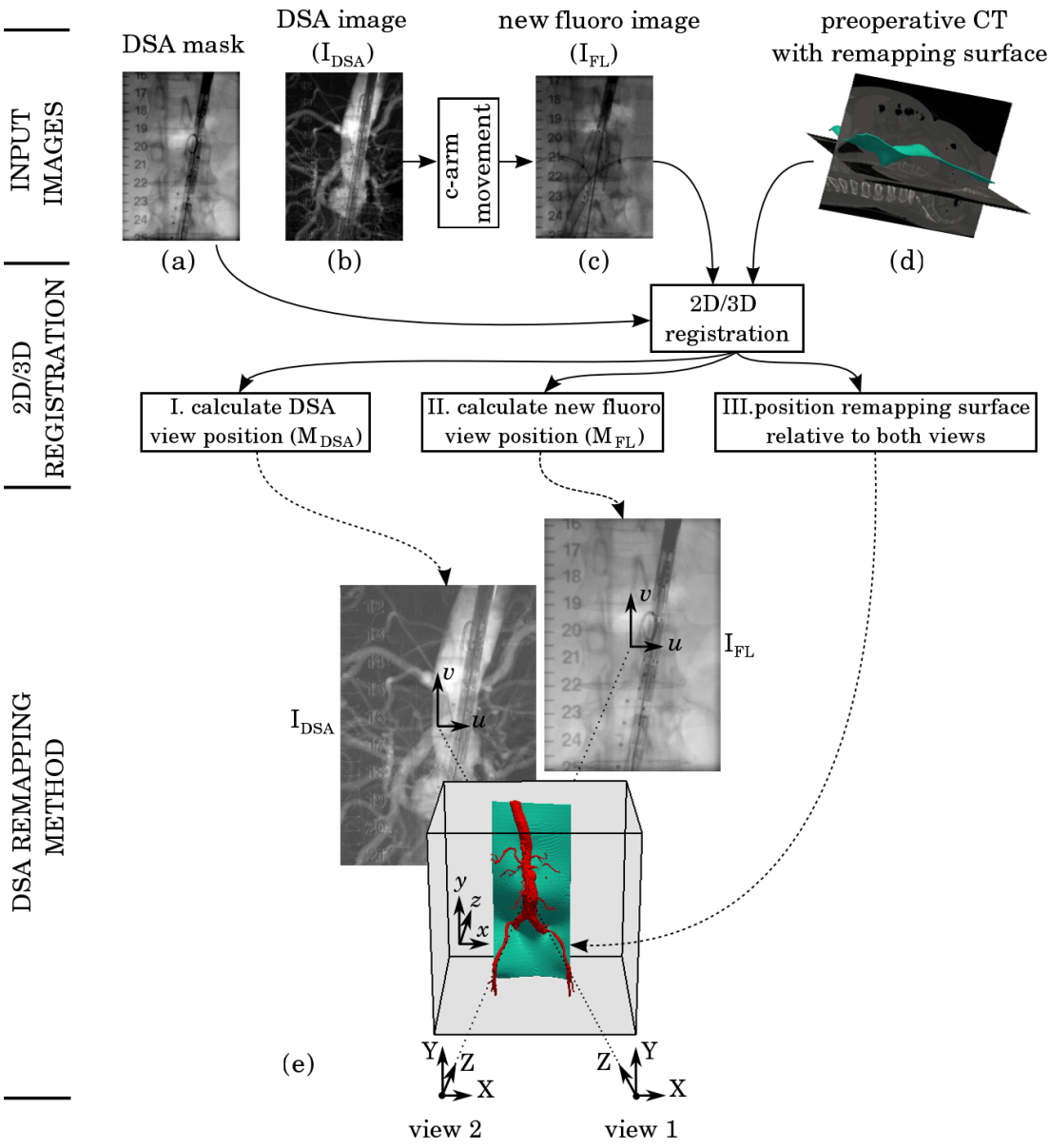

Figure 7.3: Flow diagram showing how the 2D-3D registration algorithm enables DSA remapping. Top shows input images: a) a DSA mask and b) DSA image, c) a new fluoroscopy image acquired after the C-arm was moved to a new view, and d) a preoperative CT with the remapping surface defined. Middle and bottom show the 2D-3D registration which enables e) calculation of view directions and positioning of patient-vascular-specific remapping surface.

III. The transformations M_{DSA} and M_{FL} can position the preoperatively defined remapping surface inside the CT volume with respect to both I_{DSA} and I_{FL}, enabling remapping to occur on a patient-vascular-specific surface.

7.4.2 DSA remapping process

In Sec. 7.4.1, I listed the information provided by the 2D-3D registration to enable DSA remapping. In this section, I describe how this information enables DSA remapping. This is detailed in the below steps (I, II, III, IV, V) illustrated in Fig. 7.4, where the Roman numerals in the figure correspond to the following steps:

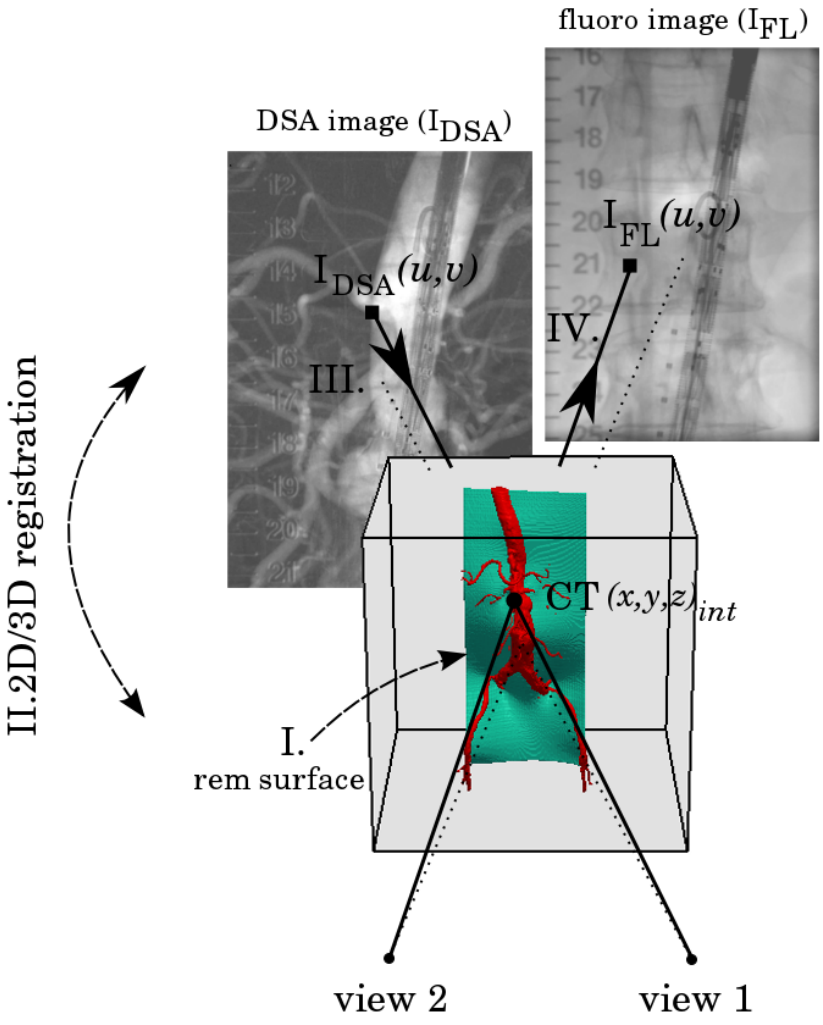

Figure 7.4: DSA remapping process shown in detail for one pixel in the DSA image: $I_{DSA}(u,v)$. A ray is back projected from $I_{DSA}(u,v)$ onto the remapping surface using M_{DSA}. The 3D interception position $CT(x,y,z)_{int}$ is then projected onto the fluoroscopy image using the transformation M_{FL} to acquire the 2D interception position in the fluoroscopy image $I_{FL}(u,v)$. Finally, the intensity at $I_{DSA}(u,v)$ is remapped to $I_{FL}(u,v)$.

I. Segmenting a remapping surface from the preoperative CT volume. The sur-

face should contain the blood vessels of clinical interest to be remapped.

II. Registering the CT volume with both images: I_{DSA} and I_{FL}, using the 2D-3D registration algorithm as described in Sec. 7.4.1. The registration allows spatial positioning of I_{DSA} and I_{FL} in relation to the segmented CT remapping surface as described in Sec. 7.4.1.I & II.

III. Back projecting rays from each of the DSA image pixels (i.e. $I_{DSA}(u, v)$) using M_{DSA}, and calculating the 3D positions in $\mathbf{CT}_{3D}$, where the rays intercept the remapping surface (i.e. $CT(x, y, z)_{int}$).

IV. Projecting rays from the 3D interception positions $CT(x, y, z)_{int}$ to I_{FL} to acquire the 2D interception position in $\mathbf{I}_{2D}$ (i.e. $I_{FL}(u, v)$). This is done using the transformation M_{FL}.

V. Finally, the intensity at each DSA image pixel $I_{DSA}(u, v)$ is remapped to the 2D interception position $I_{FL}(u, v)$ corresponding to the same pixel. This automatically produces a remapped DSA image corresponding to the current fluoroscopy view, which can be then superimposed onto the new fluoroscopy image.

7.4.3 DSA remapping errors

As discussed in Sec. 7.3, remapping a projection image into a new view requires knowledge of the depth position of the anatomical features of interest. My method provides such knowledge by defining a remapping surface inside the CT volume to intersect features of interest. The method assumes features to lie on a single 2D surface, and that the surface can be positioned correctly. However, when these assumptions are violated three types of errors arise.

Type 1 error

I define a type 1 error (E_1) to occur as a result of the thickness of the feature being remapped (i.e. the feature's size along the z direction in $\mathbf{CT}_{3D}$). E_1 is a function of the feature's thickness and changes in the ray paths (ΔrayPath) along that feature when the C-arm is moved to a new view direction, such as:

$$E_1 = f(\text{thickness}, \Delta rayPath) \begin{cases} E_1 = 0, & \text{if features completely lie} \\ & \text{on the remapping surface.} \\ E_1 > 0, & \text{otherwise.} \end{cases} \tag{7.3}$$

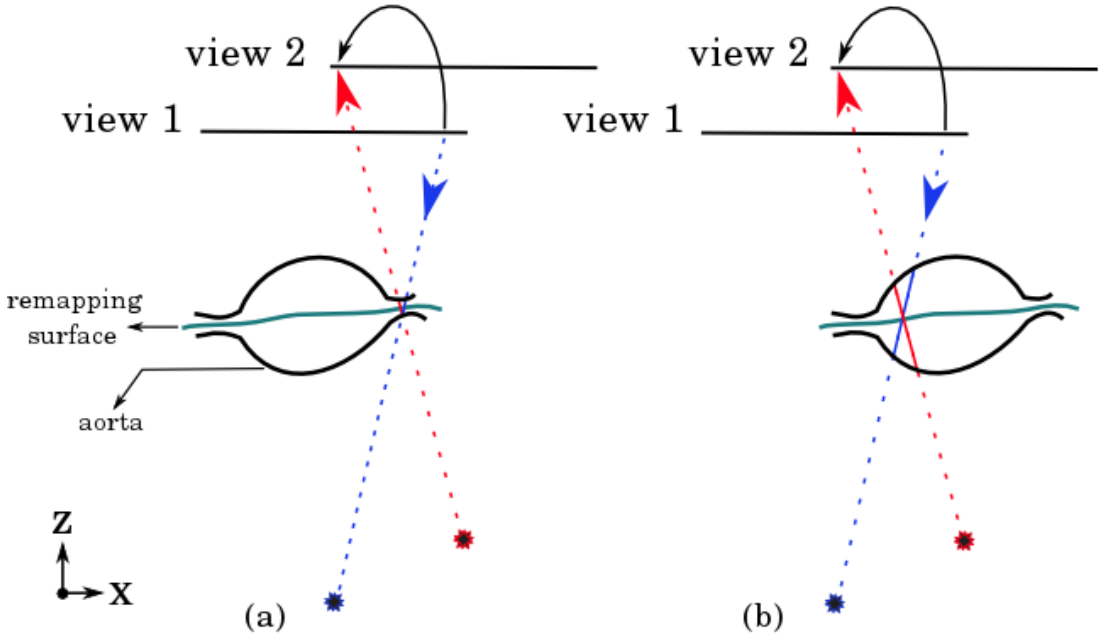

Figure 7.5: Type 1 error (E_1) as a function of the feature's thickness and changes in ray paths. Both 'a' & 'b' show images of the aorta acquired from two different views with the red arrow intersecting a different part of the aorta (solid red) than the blue arrow (solid blue), causing a type 1 error. In 'b', however, the solid red line is further away from the solid blue line when compared to 'a'.

When the entire feature lies on the remapping surface, then the ray paths along that feature are similar from any view direction and $E_1 = 0$. However, when the feature's thickness increases, the changes in the ray paths increase when the C-arm is moved, and thus, E_1 increases as seen in Fig. 7.5.

In 'a' and 'b', two images of an aneurysmal aorta are acquired from two different view directions. In both cases, the projected ray to view 2 (red arrow) does not intersect the same part of the aorta as the projected ray from view 1 (blue arrow). This causes a type 1 error in the feature's position between the remapped image from view 1 and the new image from view 2 when overlaid. In addition, in 'b', the red arrow intersection with the aorta (red solid line) is further away from the

blue arrow intersection (blue solid line) when compared to 'a'; this is because the feature's thickness in 'b' is much larger than in 'a'.

Type 2 error

I define a type 2 error (E_2) to be due to errors in positioning the remapping surface. E_2 is a function of the 2D-3D registration error (E_{reg}) as mentioned in Sec. 4.3.2, and the intraoperative deformation (D_{ef}) as described in Sec. 3.3.4, such as:

$$E_2 = f(E_{reg}, D_{ef}) \begin{cases} E_2 = 0, & \text{if } E_{reg} = 0 \text{ and } D_{ef} = 0. \\ E_2 > 0, & \text{otherwise.} \end{cases} \tag{7.4}$$

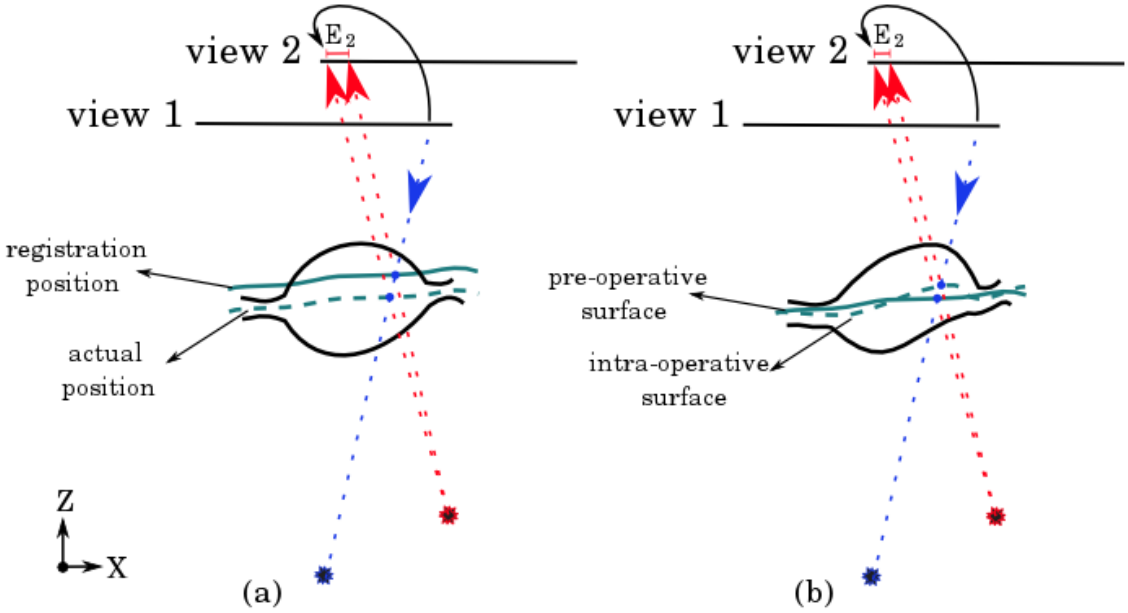

Figure 7.6: Type 2 error (E_2) relation with a) the 2D-3D registration errors (E_{reg}), and b) the intraoperative deformation (D_{ef}). In both cases two images of the aorta are acquired from different views. The blue arrow intersects the CT volume at the wrong depth position causing $E_2 > 0$ in both 'a' & 'b'.

E_{reg} results from misaligning $\mathbf{CT}_{3D}$ with $\mathbf{X}_{3D}$ (i.e. errors in $R(\theta_X, \theta_Y, \theta_Z)$ and/or $T(X, Y, Z)$). As mentioned in Sec. 4.3.2, the translation error along the Z axis (see Fig. 3.3) is the largest error observed ($\sim$ 6.7 mm) when compared to the other translational and rotational errors ($<$ 0.5 mm or degrees). Therefore, errors in positioning the remapping surface along the Z axis may occur as shown in Fig. 7.6.a. In 'a', where no deformation occurs (i.e. $D_{ef} = 0$), the blue arrow intersects the

CT volume at the wrong depth position because of the Z translation error causing E_2 error.

D_{ef} is a common issue in all methods that employ preoperative anatomy for overlay. As described in Sec. 3.3.4, the main cause of D_{ef} is the movement of stiff-wires and delivery-systems inside the aorta during intervention. This might cause errors in the position of the remapping surface as illustrated in Fig. 7.6.b. In 'b', where no registration error occurs (i.e. $E_{reg} = 0$), the blue arrow intersects the CT volume at the wrong depth position because of the intraoperative deformation of the remapping surface causing E_2 error.

It is expected that E_{reg} will have a smaller effect on type 2 errors if the remapping surface was chosen to be approximately parallel to the DSA image (I_{DSA}). This is because such a remapping surface will have a smaller error along the Z direction, which is the direction of the largest error observed in E_{reg} (i.e. the translation error along the Z axis). This is illustrated in Fig. 7.7; where the remapping surface is approximately parallel to view 1 (I_{DSA} view) in 'a', but has an angle of approximately 60° to view 1 imaging plane in 'b'. As a result, E_2 in 'b' is bigger than in 'a'.

Type 3 error

I define a type 3 error (E_3) to be due to non-rigid movement of features of interest (relative to the vertebra on which registration is based) between the time the DSA image (I_{DSA}) was acquired, and the time the new fluoroscopy image (I_{FL}) was acquired. E_3 is a function of the different stages during an intervention which exhibit different amounts of intraoperative deformation depending on the type of the interventional devices present.

E_3 is a minimum when I_{DSA} and I_{FL} are acquired during the same stage of the intervention as the amount of deformation should be similar for both images. However, if I_{DSA} and I_{FL} are acquired during different stages, then E_3 increases as the two images show anatomy with different amounts of deformation. In addition, the delivery device with the undeployed stent-grafts is the main cause of deformation, therefore, if I_{DSA} is acquired when the delivery device is present and I_{FL} when no stiff instruments are present, E_3 is likely to be a maximum when used in EVAR.

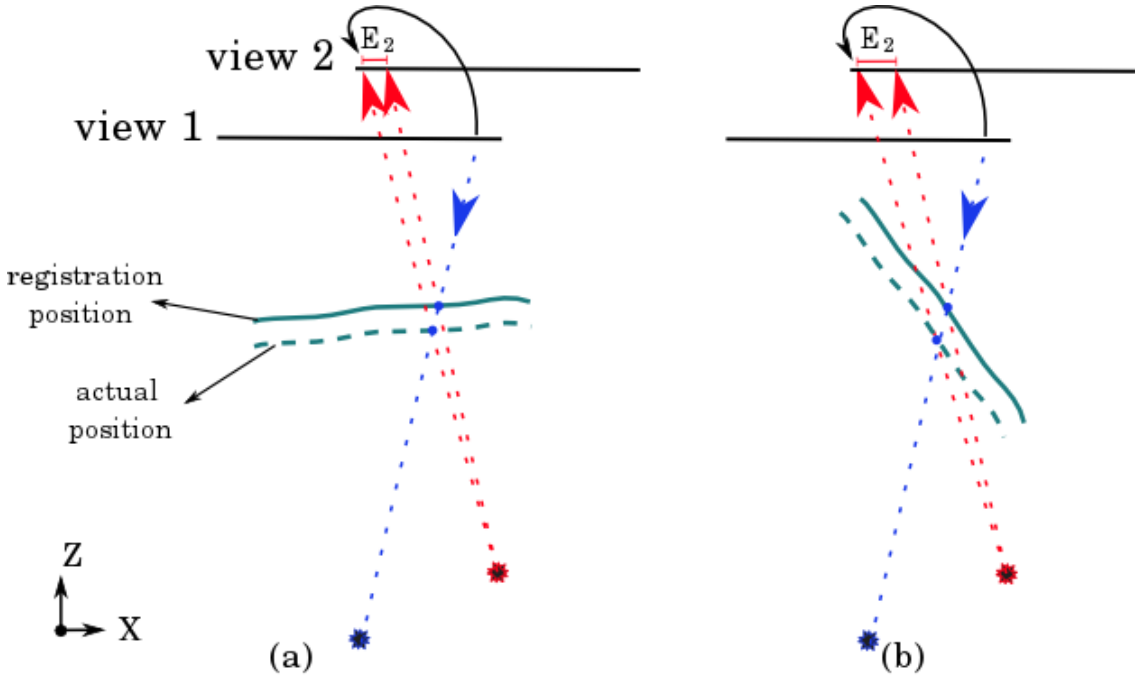

Figure 7.7: Type 2 error (E_2) relation with the direction of the remapping surface, when a 2D-3D registration error exists. a) The remapping surface is approximately parallel to view 1; whereas in b) the surface has an angle of approximately 60° with view 1 imaging plane. As a result, E_2 in 'b' is bigger than in 'a'

.

7.5 Data and Experiments

Datasets from 9 patients who underwent a complex EVAR procedure of the AAA (as presented in the case study in Sec. 2.5) were used. Experiments were carried out retrospectively (i.e. not during procedure), and were approved by the national research ethics committee (09/H0707/64), with informed patient consent. No attempt was made to select particular patient cases based on image quality or amount of intraoperative aortic deformation.

Each patient had:

1. A preoperative diagnostic CT scan, acquired on a variety of machines depending on the referring hospital.

2. A number of intraoperative images including screening images, angiography images, and DSA images acquired on a Siemens FP20.

7.5.1 Experiment with patient data

Each patient's standard diagnostic CT scan was used. These had voxel sizes which ranged from $0.683 \times 0.683 \times 0.7\,\text{mm}^3$ to $1 \times 1 \times 1\,\text{mm}^3$. The intraoperative images of all patients were acquired with image dimensions of 1024×1024 pixels, pixel sizes ranging from $0.154 \times 0.154\,\text{mm}^2$ to $0.372 \times 0.372\,\text{mm}^2$, a FoV of either 22, 32, 42, or 48 cm, and a frame rate ranging from 2 to 7 fps.

For each patient, the aorta was segmented from the preoperative CT volume using a semi-automatic method in ITK-SNAP [Yushkevich et al., 2006]. The remapping surface was then defined using the same method described in Sec. 5.2.2 (i.e. by picking points along the midline of the aorta, iliac and renal arteries and then producing a surface using thin-plate-spline interpolation). An example of such a remapping surface can be seen in Fig. 5.3 in Sec. 5.2.2. This surface was chosen to remap blood vessels of interest, i.e. the aorta, and renal and iliac arteries.

For each dataset, a DSA image produced from approximately an AP view at an early stage of the intervention was chosen to be remapped. These DSA images show the delivery devices with the undeployed stent-grafts as well as vasculature. DSA remapping, as described in Sec. 7.4.2, was then carried out to remap the chosen DSA image to a number of fluoroscopy images acquired at different stages of the intervention after C-arm movement (but still acquired approximately from AP views). Finally, each remapped DSA image was superimposed onto the corresponding fluoroscopy image as a roadmap.

7.5.2 Validation experiments

Validation fluoroscopy images were chosen for each dataset which clearly showed the position of the renal arteries, either by the position of a guide-wire or a stent-graft, or by the use of ICM. The roadmap accuracy was then calculated at a clinically relevant position: the renal ostium in both the fluoroscopy image (I_{FL}), and the remapped DSA image ($I_{DSA(rem)}$), as shown in Fig. 7.8.

In 'a', the guide-wire was used to locate the position of the renal artery in the new fluoroscopy image. An error value of zero was recorded if the wire in I_{FL} went through the $I_{DSA(rem)}$ renal ostium in the roadmap image. Otherwise, the error

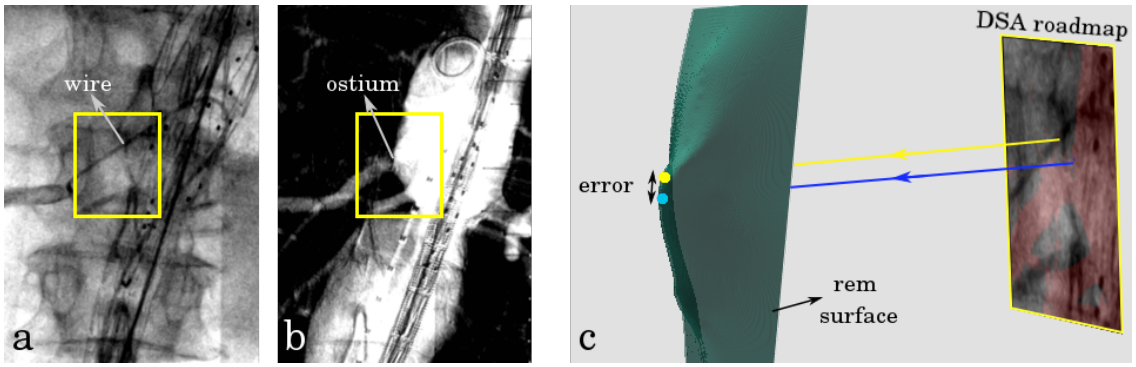

Figure 7.8: Illustration of the used validation method for DSA remapping. a) The new fluoroscopy image with the guide-wire locating the position of the renal artery identified. b) The remapped DSA image with the renal ostium identified. c) Rays are back projected from the zoomed roadmap image into the remapping surface using the transformation M_{FL}, and the error is calculated in mm in $\mathbf{CT}_{3D}$.

value was calculated as described in 'c'.

In 'c', two rays were back projected from the roadmap image into the remapping surface using the transformation M_{FL}. The blue ray was back projected from the nearest ostium's pixel to the wire; while the yellow ray was back projected from the nearest wire's pixel to the ostium. The distance (i.e. error) between the two points of interception with the surface was then calculated in mm in $\mathbf{CT}_{3D}$, using the formula in Eqn. 7.5. This method allows the error to be calculated in real anatomical distance (i.e. mm) not a projected distance (i.e. pixels).

$$Error = \sqrt{(x_1 - x_2)^2 + (y_1 - y_2)^2 + (z_1 - z_2)^2} \tag{7.5}$$

In the case where a stent-graft or ICM was used to locate the position of the renal artery, the middle-points of the ostia were located in both I_{FL} and $I_{DSA(rem)}$, and the same method of back projection was used to calculate the error in mm. In addition, if both renal ostia (i.e. left and right) could be identified in I_{FL}, rays were back projected from each ostium for the same roadmap image, thus calculating each ostium's remapping error.

For each dataset, and in all cases (i.e. wire, stent, or ICM), locations of the renal ostia were visually located by 2 observers independently. Two sets of errors were then calculated and averaged for each dataset.

7.5.3 Experiment to calculate 2D-3D overlay errors

As mentioned in the introduction, 2D-3D registration is the primary technique used to reduce repeated DSA imaging by providing 3D preoperative overlays during EIGS. Non-rigid intraoperative vascular deformation, however, is the major drawback of such methods.

To investigate the potential advantage of my proposed method over 2D-3D overlays, the experiment illustrated in Fig. 7.9 was carried out in order to calculate the accuracy of 2D-3D overlay in a method similar to the one explained in the previous section to acquire comparable results.

For each DSA remapping, the transformation M_{FL} was used to overlay a surface rendering of the CT aorta lumen and visceral vessels onto I_{FL} as illustrated in Fig. 7.9.a. To calculate the overlay accuracy using the same method explained in the previous section, a $DRR_{vessels}$ of the overlaid aorta was produced as shown in 'c' (by using $CT_{vessels}$ segmentation as described in Sec. 6.2). The $DRR_{vessels}$ image was then treated similarly to $I_{DSA(rem)}$ in the previous section: the renal ostium was visually located, and rays were back projected as in 'c'. The error in mm in $\mathbf{CT}_{3D}$ was then calculated as described in the previous section.

In addition, the accuracy errors differences between the 2D-3D overlay method and the DSA remapping method were tested for any statistical significance.

7.6 Results

In the following, I present the DSA remapping results. This includes graphical results from 3 patients which are a representative sample of the calculated remapping errors, and numerical results of the calculated remapping accuracy for all patients. Finally, the 2D-3D overlay accuracy for each patient is presented and compared with the remapping accuracy.

7.6.1 DSA remapping results

Figure 7.10 shows results from patients 2 (top row), 4 (middle row), and 8 (bottom row) as follows:

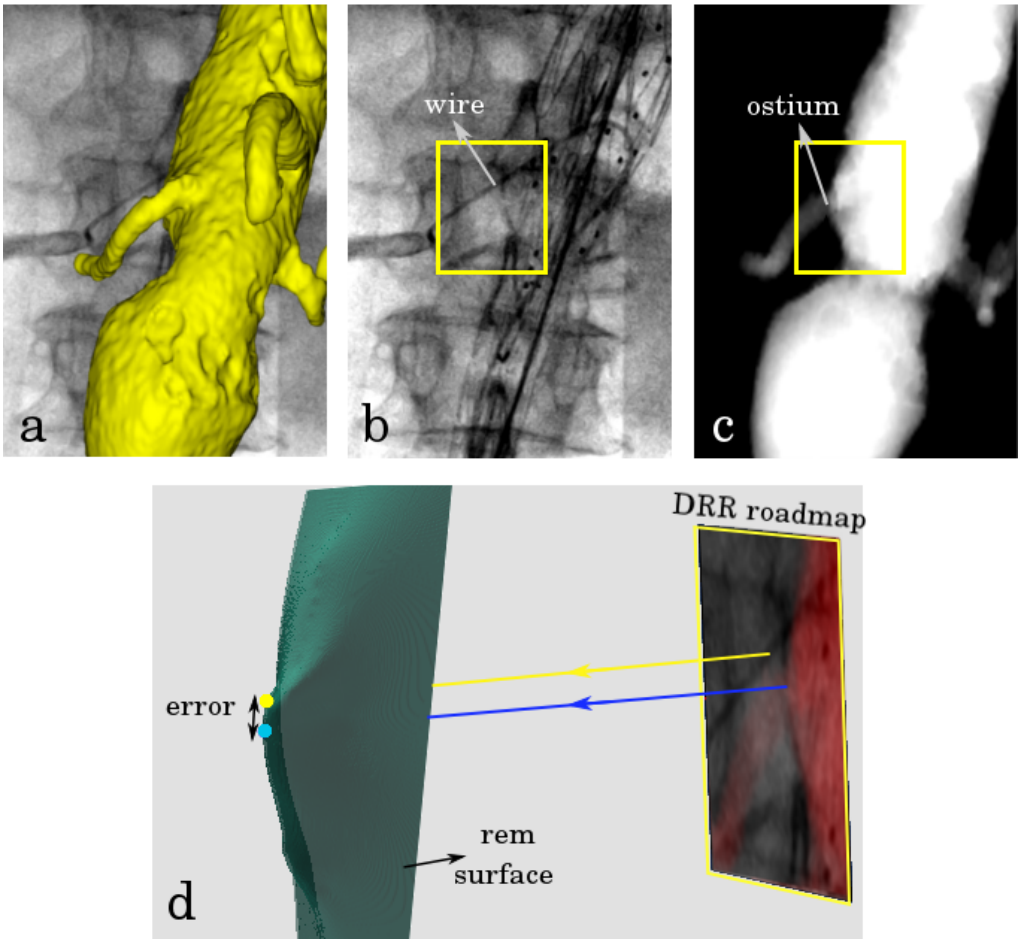

Figure 7.9: Illustration of the used method to calculate the 2D-3D overlay accuracy. a) A surface rendering of the CT aorta overlaid onto I_{FL} using the calculated transformation M_{FL}. b) I_{FL} with the guide-wire locating the position of the renal artery identified. c) A $DRR_{vessels}$ of the overlaid aorta with the renal ostium identified. d) Rays are back projected from the zoomed roadmap image into the remapping surface using the transformation M_{FL}, and the error is calculated in mm in $\mathbf{CT}_{3D}$.

a) The DSA image (I_{DSA}) which was chosen to be remapped, and was produced from approximately an AP view.

b) The fluoroscopy image (I_{FL}) acquired after the C-arm was moved, but from approximately an AP view.

c) The remapped DSA image ($I_{DSA(rem)}$).

d) $I_{DSA(rem)}$ overlaid onto I_{FL} in red as a roadmap, with the renal ostia marked with blue dots in $I_{DSA(rem)}$, and yellow dots in I_{FL}.

The presented patients were chosen to have remapping errors which covered the full range of observed averaged errors: 1.21 mm (top row), 2.92 mm (middle row), and 6.16 mm (bottom row).

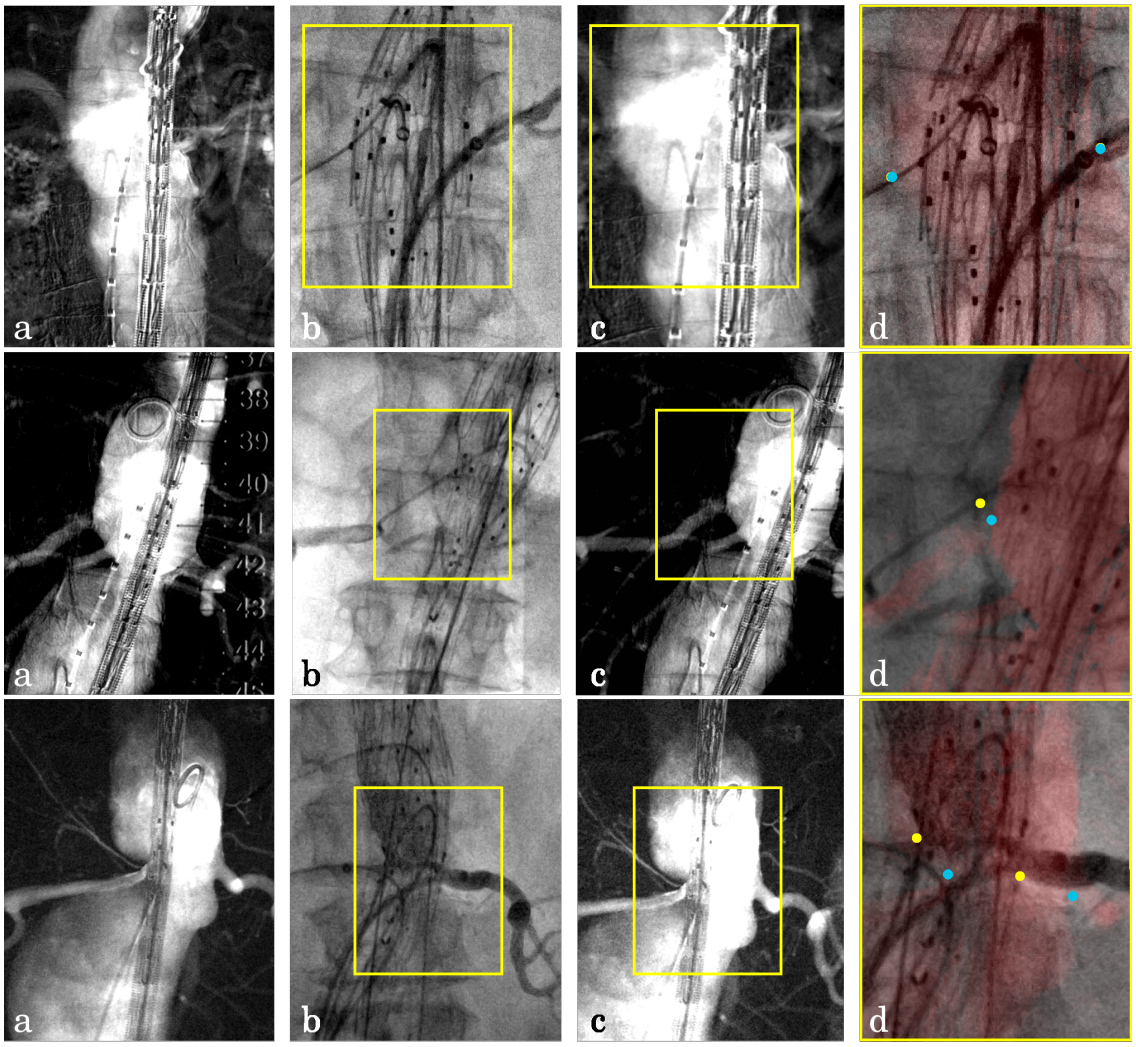

Figure 7.10: Representative results from patients 2 (top row), 4 (middle row), and 8 (bottom row), which had averaged remapping errors of 1.21 mm, 2.92 mm, and 6.16 mm, respectively. a) I_{DSA}, b) I_{FL}, c) $I_{DSA(rem)}$, and d) $I_{DSA(rem)}$ overlaid onto I_{FL} in red, with the renal ostia marked with blue dots in $I_{DSA(rem)}$ and yellow dots in I_{FL}.

DSA remapping time

The 2D-3D registration was performed on a computer with two NVidia GTX 690 graphic cards with each card containing two GPUs. A single 2D-3D registration was completed in 1.25 sec, and the remapping software took around 1 sec. Thus,

the entire remapping process time was around 3.5 sec for each fluoroscopy image.

DSA remapping accuracy

For each patient, the remapping accuracy, as described in Sec. 7.5.2, was calculated for all images and averaged. Table 7.1 lists the number of DSA remappings and error calculations performed for each patient, and the maximum and averaged remapping errors. The overall results are presented in bold text.

Table 7.1: The number of DSA remappings and error calculations performed, and the maximum and averaged remapping errors in mm for each patient. Overall results are presented in bold text.

	DSA remapping method			
	number of remappings	number of error calculations	max. error (mm)	avg. error (mm)
Pat 1	5	8	3.39	1.79
Pat 2	7	7	1.88	1.21
Pat 3	5	7	3.18	1.93
Pat 4	4	5	4.55	2.92
Pat 5	3	4	2.17	1.43
Pat 6	2	4	3.04	1.91
Pat 7	6	9	4.64	2.61
Pat 8	6	11	11.57	6.16
Pat 9	2	2	6.19	4.58
Overall	**40**	**57**	**11.57**	**2.73**

Numerical results showed an overall averaged error of 2.73 mm over 40 remapped images, with 7 cases scoring averaged errors ≤ 3 mm. For 2 patients, larger averaged errors (> 4 mm) were observed. In 4 patients, large maximum errors (> 4 mm) were observed, with patient 8 scoring the highest maximum and averaged errors (11.57 mm and 6.16 mm respectively).

7.6.2 2D-3D overlay accuracy results

For each patient, the 2D-3D overlay accuracies were calculated as described in Sec. 7.5.3, and presented in Tab. 7.2. Similarly to Tab. 7.1, Tab. 7.2 also includes the number of 2D-3D overlays and error calculations performed for each patient, and the maximum and averaged errors. The overall results are also presented in bold text.

Table 7.2: The number of 2D-3D overlays and error calculations performed, and the maximum and averaged errors in mm for each patient. Overall results are presented in bold text.

	2D-3D overlay method			
	number of overlays	number of error calculations	max. error (mm)	avg. error (mm)
Pat 1	5	8	9.61	7.40
Pat 2	7	7	4.30	3.49
Pat 3	5	7	4.20	2.24
Pat 4	4	5	9.82	4.93
Pat 5	3	4	8.09	4.46
Pat 6	2	4	9.85	7.45
Pat 7	6	9	12.10	9.05
Pat 8	6	11	19.32	10.76
Pat 9	2	2	9.76	7.52
Overall	**40**	**57**	**19.32**	**6.37**

Numerical results showed an overall averaged error of 6.37 mm over 40 overlays. Only 1 case had an averaged error ≤ 3 mm. Averaged errors for all other patients were > 4 mm, including 5 cases with errors > 7 mm. Patient 8 scored the highest maximum and averaged errors (19.32 mm and 10.76 mm respectively).

Tabel. 7.3 lists side by side the averaged errors of both the DSA remapping method and the 2D-3D overlay method for each patient for direct comparison. The percentage increase of errors after using the 2D-3D overlay is also reported. The overall results are presented in bold text.

Table 7.3: Comparing the averaged errors and percentage increase between the DSA remapping method and the 2D-3D overlay method for each patient, with the overall results presented in bold text.

	averaged error		
	DSA remapping	2D-3D overlay	increase %
Pat 1	1.79	7.40	+313.41%
Pat 2	1.21	3.49	+188.43%
Pat 3	1.93	2.24	+16.06%
Pat 4	2.92	4.93	+68.83%
Pat 5	1.43	4.46	+211.89%
Pat 6	1.91	7.45	+290.05%
Pat 7	2.61	9.05	+246.74%
Pat 8	6.16	10.76	+74.67%
Pat 9	4.58	7.52	+64.19%
Overall	**2.73**	**6.37**	**163.81%**

The results showed a 163.81% increase in overall averaged error after using the 2D-3D overlay technique. In 1 case only, there was a slight increase in error (16.06%), however, errors increased by more than 64% for all other cases.

A student's t-test (paired, 2 tails) was used to examine whether the increase in accuracy errors after using the 2D-3D overlay method was statistically significant or not. The t-test showed statistically that there was a significant difference between the mean values of the 2 error datasets ($p < 0.01$).

7.7 Discussion

A novel imaging technique: "DSA remapping", to reduce repeated DSA imaging during interventional fluoroscopy has been developed. Consequently, the volume of nephrotoxic ICM and radiation exposure would be reduced potentially, allowing interventionists to perform more complex procedures with longer screening times. The technique is particularly beneficial for patients with renal insufficiency and/or patients at high risk of radiation adverse response. I propose that DSA remapping

could find a role alongside DSA imaging, replacing DSA imaging where appropriate, while using DSA for critical points in the procedure.

My proposed method calculates the view positions of both the DSA image and the new fluoroscopy image (which is acquired after the C-arm is moved) using 2D-3D registration. Therefore, the method is able to work with any existing fluoroscopy system without any hardware alterations, and does not require mechanical tracking of the C-arm nor calibration. The method only requires the use of a preoperative CT scan, which is already available as a part of the routine planning for EVAR procedures. Moreover, the remapping surface can be defined preoperatively inside the CT volume to intersect features of interest. This then enables DSA remapping to automatically enhance vasculature without the need for any input from the interventional team during the intervention which could interrupt the clinical work-flow.

As described in Sec. 7.4.3, the proposed method can only employ an accurately positioned single 2D surface for remapping. The aorta does not just originate from a single 2D surface. However, for small structures of the aorta such as the renal ostia, this is not expected to have a large effect on type 1 errors (E_1). The robustness of the registration algorithm to accurately position the CT volume has been tested and reported (see Sec. 4.3.2). The Z translation error (~ 6.7 mm) would have a smaller effect on type 2 errors (E_2) compared to the intraoperative deformation (< 10 mm, Sec. 3.3.4). This is because the deformation could result in the use of a remapping surface at a further distance from the intraoperative position of the clinical features. Moreover, if the remapping surface was chosen to be approximately parallel to the imaging plane, errors along the direction perpendicular to the imaging plane (i.e. Z) would have a much smaller effect than errors along the other directions (i.e. X and Y), when projected into the imaging plane. Intraoperative deformation might occur along any direction, whereas registration errors occur mainly along the Z direction.

Nevertheless, during fluoroscopy interventions, surgeons are mostly interested in using overlays after the delivery-system was inserted, which is known to cause the largest amount of deformation (see Sec. 3.3.4). Unlike 2D-3D registration methods which use preoperative overlays acquired before the deformation has occurred,

my method uses an intraoperative roadmap (i.e. a DSA image) acquired after the delivery-system was inserted and has caused deformation. Therefore, when new fluoroscopy images are acquired with the delivery-system still present, the remapped DSA image should have a similar amount of deformation resulting in a better roadmap accuracy than that in 2D-3D registration overlays. To investigate this hypothesis, 2D-3D overlay accuracy was computed as in Tab. 7.2, and compared with DSA remapping accuracy as in Tab. 7.3. After using the 2D-3D overlay method, an increase in errors ranging from 16% to 313% was observed for all patients. Moreover, the overall averaged error increased by 163%. The t-test showed that the increase in accuracy errors after using the 2D-3D overlay method was statistically significant ($p < 0.01$).

The results presented in Tab. 7.1 showed an averaged remapping error of 2.73 mm over 40 remappings performed. Error variations across different remappings for the same patient were observed. This can be explained by the fact that remappings were performed at different stages of the procedure for each patient (see Sec. 7.5.1). Thus, the aorta experienced different amounts of intraoperative deformation depending on the type of interventional devices present causing type 3 errors (E_3). Patient 8 was found to have the most angulated aorta among all patients. This explains the big errors obtained for this patient as highly angulated aortas experience more intraoperative deformation than less angulated aortas as reported by Carrell et al. [2010] (see Sec. 3.3.4).

7.8 Conclusions

In conclusion, a novel method to reduce repeated DSA imaging during interventional procedures has been presented. The method employs a 2D-3D registration algorithm to enable DSA remapping onto a new fluoroscopy image after the C-arm is moved, and uses standard interventional equipment. This allows repeated ICM-free DSA imaging and reduced radiation dose. 40 DSA images were remapped. Results showed an overall averaged error of 2.73 mm, with 7 cases scoring averaged errors $\leq$ 3 mm. For 2 patients, larger averaged errors ($>$ 4 mm) were observed. The patient with the highest averaged error (6.16 mm) was found to have the most

angulated aorta, and thus experienced large intraoperative deformation. When the accuracy of the proposed method was compared with the 2D-3D overlay method, the 2D-3D overlay method had statistically significant larger averaged errors (163.81% larger).

Chapter 8

Conclusions and Future Work

Contents

The main aim of this thesis was to investigate novel methods to enhance vascular visualization, and to reduce ICM usage and the associated radiation dose during complex EVAR procedures, while maintaining the clinical work-flow. The clinical motivations behind this aim were the required high accuracy, the lengthy imaging time, and the large volumes of ICM used during complex EVAR procedures.

This chapter summarises the outcomes of the main research objectives, and puts the outcomes in context with the original contributions. The chapter then discusses the investigation's main limitations, and highlights the potential clinical impact. Finally, work to be carried out in the future is suggested, and an overall

summary is given.

8.1 Overview of Contributions

Chapter 3 provided an overview of prior work. Although very little work has been carried out on iDTS, the work on the literature has showed that iDTS has potential advantages over CBCT to aid IGS interventions. The proposed methods demonstrated reduced scanning time and patient dose, and caused much less interruption to the clinical work-flow compared to CBCT. However, out-of-plane clutter is still the main limitation. In addition, the proposed 3D iDTS images would require some interaction from surgeons to find the clinically relevant information to be displayed, which could cause an interruption to the clinical work-flow during EIGS. Moreover, these iDTS methods still use mechanical tracking of the X-ray source, which requires frequent geometrical calibration.

Chapter 3 also showed that overlaying 3D preoperative vasculature onto fluoroscopy images is the main technique developed to aid guidance during EIGS interventions without ICM injection. However, intraoperative deformation is still the major limitation, especially in complex cases with tortuous anatomy, where the technique would probably be most beneficial.

Enabling iDTS and DSA remapping on a standard fluoroscopy system by employing a rigid 2D-3D image registration algorithm, have been the two main research objectives investigated in this work. In the following, the outcomes of the research objectives in the context of the original contributions are summarised.

8.1.1 iDTS facilitated by 2D-3D registration

The first research objective investigated in chapters 4, 5, and 6, was to enable iDTS, using just a 40° sweep, on a standard fluoroscopy system by employing a rigid 2D-3D image registration. By making use of the preoperative CT scan, a number of additional advantages were investigated: reduced out-of-plane clutter, automatic reconstruction of patient-anatomy-specific 2D images, and eliminating the need for frequent geometrical calibration.

In chapters 5 and 6, I investigated employing a well established 2D-3D registra-

tion system to enable iDTS on a standard fluoroscopy system. This allowed:

1. Subtraction of the vertebral bone from fluoroscopy images prior to iDTS reconstruction. High contrast bony features are the largest cause of out-of-plane clutter, thus, removing bone prior to reconstruction greatly reduced the effect of out-of-plane clutter, and improved iDTS image quality.

2. Reconstruction of patient-anatomy-specific 2D images. 3D iDTS information was back projected onto the used 2D view without requiring clinician interaction, thus, image acquisition and display would maintain the clinical work-flow.

3. Reconstruction of iDTS images without the need of any mechanical tracking of the C-arm position. Thus, geometrical accuracy was not required, which is particularly important in C-arm systems which are known to exhibit gravity-induced mechanical flex.

The new methods were tested in chapter 5 using clinical datasets from a phantom and 4 patients who underwent a complex EVAR procedure. All datasets were acquired by rotating the C-arm 40° RAO/LAO without the use of ICM. Phantom SDNR results showed a 3419% improvement compared to standard fluoroscopy. Reconstruction results from phantom and patients showed the methods' ability to automatically enhance the aortic outline and calcium, with much reduced clutter after bone removal. Moreover, the methods resulted in a 93.96% average reduction in radiation dose compared to DSA imaging.

Chapter 6 also tested the new methods using a CT-based synthetic dataset. The dataset contained synthetic fluoroscopy images to simulate a 40° C-arm sweep, to which synthetic contrast was added to simulate 10-30% diluted amount of ICM injection compared to standard DSA imaging. Reconstruction results showed the additional benefit of enhancing small vascular structures such as the renal ostia and bifurcation, when compared with the results from chapter 5. Moreover, all reconstructed iDTS images with simulated contrast had better SDNR values compared to the produced synthetic DSA image with motion and noise artefacts.

8.1.2 DSA remapping facilitated by 2D-3D registration

The second research objective investigated in chapter 7 was to enable DSA remapping from one view to another, on a standard fluoroscopy system, by using the same rigid 2D-3D image registration proposed in chapter 4. The investigated advantage was to remove the requirement to repeat DSA imaging which often occurs during EIGS interventions after movement of the fluoroscopy set.

The new method was tested using clinical datasets from 9 patients who underwent a complex EVAR procedure. For each dataset, a DSA image was chosen to be remapped to a number of fluoroscopy images after the C-arm was moved. Remapping results showed an overall averaged error of 2.73 mm, with 7 cases scoring averaged errors $\leq$ 3 mm, which is clinically acceptable [Carrell et al., 2010]. Moreover, compared to the 2D-3D overlay method, the DSA remapping method was found to decrease the overall averaged error by 163%.

DSA remapping showed potential to enable a reduction in the overall nephrotoxic ICM usage, and radiation dose while actually improving the clinical work-flow. This is particularly beneficial for patients with renal insufficiency, and/or patients at high risk of radiation adverse response undergoing complex procedures.

8.2 Limitations of the Investigation

The reconstructed de-iDTS images in chapter 5 were able to enhance the aortic outline and calcium without any ICM injection, and were able to reduce radiation dose compared to DSA imaging. However, DSA still provides much better vascular enhancement than ICM-free de-iDTS. In addition, de-iDTS imaging without contrast was unable to enhance clinically important small vasculature such as the renal ostia. Therefore, the main limitation of current de-iDTS images is the insufficiency to guide complex EIGS procedures, making DSA imaging a much preferable method to enhance vascular visualization. Nevertheless, ICM-free de-iDTS images provided valuable intraoperative information on the position of the deformed aorta, which could be used to enable non-rigid 2D-3D image registration. If such intraoperative information is required frequently by a non-rigid registration system to warp the preoperative aorta, de-iDTS is a much preferable imaging method than DSA, as

it requires no ICM injection and involves much reduced radiation dose. Moreover, potential methods to improve input fluoroscopy images before ICM-free de-iDTS reconstruction can be investigated in the future (e.g. using more radiation dose during the C-arm sweep, but still much less than is used in DSA imaging).

To overcome this limitation, and to reconstruct de-iDTS images with better vascular enhancement including small vascular structures, de-iDTS imaging was performed with 10-30% the amount of ICM used in standard DSA imaging in chapter 6. Results showed that reduced-ICM de-iDTS imaging can potentially replace DSA, as it requires 70% less ICM injection and involves much reduced radiation dose. Nevertheless, the limitation of the investigation conducted in chapter 6 was that all experiments were carried out using only synthetic datasets, as injecting additional ICM would not have been ethically acceptable.

Another limitation of this work was the unavailability of specific validation datasets. Because of ICM nephrotoxicity and the ionizing nature of X-ray, no validation images were acquired during the performed EVAR procedures for the specific purpose of validation, as no ethical approval was available.

8.3 Potential Clinical Impact

The technical work presented in this thesis has shown promising potential using a small number of patient datasets: four patients for ICM-free de-iDTS imaging in chapter 5, and nine patients for DSA remapping in chapter 7. Reduced-ICM de-iDTS imaging was only tested using synthetic datasets in chapter 6. All datasets were not processed during EVAR interventions, but were processed offline, thus, a clinical study during interventions is required to examine the methods' impact in a clinical setting. Nevertheless, a larger set of patients data has to be first acquired and processed offline to confirm potential benefits, especially for the reduced-ICM de-iDTS imaging technique.

The main application used in this work was AA enhancement during complex EVAR interventions. However, the methods proposed in this thesis can be used to enhance blood vessel visualization in any EIGS procedure where DSA imaging is used in the thoracic and/or abdominal regions (because a vertebra is required

for registration). Other possible applications for ICM-free de-iDTS imaging are to enhance structures in other IGS interventions carried out in the thoracic and/or abdominal regions, and to enable non-rigid 2D-3D image registration by providing intraoperative information when needed.

The developed methods have promising potential clinical impact on fluoroscopy guided interventions. This includes reducing ICM related renal complications, as less ICM would be required to enhance vasculature. This will also lead to a reduction in the DSA associated radiation exposure to both the patient and the interventional team, as DSA imaging contributes most of the patient radiation dose. Patients with existing renal problems and/or patients at high risk of radiation adverse response undergoing complex EIGS interventions would benefit the most from the new techniques.

8.4 Future Work

In the following, I suggest potential research lines which could be investigated in the future. These mainly include acquiring specific datasets for validation, testing the new imaging methods clinically in a series of procedures, and enabling non-rigid registrations.

8.4.1 Validation methods

In chapter 5, two types of CT features: the aorta and aortic calcification were overlaid onto the reconstructed iDTS images for validation. However, the CT features did not include the intraoperative deformation caused by the stiff interventional instruments, and thus a manual adjustment was required to match the CT features with the iDTS enhanced features (see Sec. 5.2.3). Future work could be to acquire a 3D CBCT scan right after the C-arm sweep for validation. A CBCT scan is needed rather than a DSA image because the enhanced aortic outline in the iDTS images represents the entire aorta (i.e. aorta lumen plus thrombus), and a DSA image will only show the aorta lumen (i.e. where the contrast flows). CBCT features (which include intraoperative deformation) can then be overlaid onto the reconstructed iDTS images for validation. However, acquiring validation CBCT scans for such a

study would require ethical approval.

In chapter 6, after the DSA image was remapped to a new fluoroscopy image, validation was only possible if the new fluoroscopy image showed the position of the renal arteries either by the position of a guide-wire or a stent-graft, or by the use of ICM. Moreover, identifying the ostium in the validation fluoroscopy images was dependent on the observer's experience (see Sec. 7.5.2). A more accurate method is to acquire a DSA image at the new fluoroscopy image view for validation. The remapping accuracy can then be calculated between the remapped DSA image and the validation DSA image at a clinically relevant position. Nevertheless, injecting additional ICM just for validation is not ethically acceptable. Another validation method which can be investigated and does not involve ICM injection, is to place virtual landmarks inside the CT volume which correspond with clinical landmarks in the fluoroscopy images (e.g. the fenestration markers on the stent-graft). A remapping surface can then be defined inside the CT volume to include the virtual landmarks. The clinical landmarks could be remapped from one fluoroscopy view to another using the defined remapping surface, and compared with the existing clinical landmarks in the new fluoroscopy view.

8.4.2 Clinical study

The iDTS image acquisition and reconstruction process can be optimised for clinical use. The reconstruction process is highly parallelizable, and I believe that image acquisition and reconstruction in under a minute is easily achievable on a modern workstation using GPGPU computing.

The potential use of reduced-ICM de-iDTS imaging and DSA remapping during a series of procedures could be investigated. However, injecting additional ICM during the C-arm sweep will require an ethical approval. Clinicians will be able to view the de-iDTS images and the remapped DSA images during the procedure, and the image quality of desired clinical features and potential to improve guidance will be examined. In addition, the effect of varying image acquisition: C-arm sweep range, and frame rate on image quality and clinical acceptability (patient dose and interruption to clinical work-flow) can be examined. Furthermore, the reduction in ICM usage and radiation dose could be determined.

8.4.3 Non-rigid registration

As mentioned in Sec. 8.2, a potential benefit of ICM-free de-iDTS images is to enable non-rigid image registration. Guyot [PhD under preparation] is investigating such potential benefit of de-iDTS imaging in the following two ways:

1. Using de-iDTS images as an alternative to DSA to enable a 2D-3D non-rigid registration method. The original method requires manual picking of corresponding aortic points between the preoperative CT aorta surface, and the intraoperative fluoroscopy images. However, ICM injection was required to enhance the aorta visualization in the fluoroscopy images for point picking. The new method employs de-iDTS images to obtain intraoperative information on the position of the deformed aorta without any ICM injection, and has much reduced radiation exposure compared to DSA.

2. Using 3D de-iDTS images as an alternative to CBCT to enable a 3D-3D non-rigid registration method. The method uses the enhanced aortic calcifications in the reconstructed de-iDTS volume for registration with the preoperative CT data. Acquiring a small de-iDTS sweep rather than a semicircular CBCT images involves much less radiation dose, scanning time, and clinical interruption. To reconstruct a de-iDTS volume containing the aortic calcifications, a stack of de-iDTS images can be reconstructed using a flat plane parallel to the imaging detector, and positioned on different depths across the aorta.

8.5 Overall Summary

In this thesis, I have developed and investigated novel imaging techniques that offer enhanced vascular visualization, with reduced ICM usage and radiation exposure, but still maintain the clinical work-flow. My hypothesis was that these techniques can be beneficial during complex EIGS interventions using C-arm fluoroscopy, as such interventions require high accuracy, and involve long imaging time and a large volume of ICM.

The developed methods: de-iDTS imaging and DSA remapping were enabled on a C-arm fluoroscopy system by using a well established rigid 2D-3D registra-

tion system which has been mainly developed to improve EIGS, but suffers from intraoperative vascular deformation. Therefore, these new imaging techniques can be performed on any standard fluoroscopy system, and do not require mechanical tracking of the C-arm nor frequent calibration.

The proposed novel methods have been able to provide additional intraoperative information about the deformed aorta position, which cannot be provided by the preoperative CT volume alone. The methods also have the potential to enable a reduction in overall ICM usage and radiation dose, while maintaining the clinical work-flow. I believe that if these new imaging methods became incorporated with fluoroscopy systems, they could play an important role alongside DSA imaging, in particular for patients with renal complications undergoing complex EIGS interventions. In addition to vascular enhancement during EIGS, iDTS could be potentially used to enhance structures in a wide range of IGS applications.

Bibliography

M. Alhrishy, A. Varnavas, T. Carrell, A. King, and G. Penney. Interventional digital tomosynthesis from a standard fluoroscopy system using 2D-3D registration. In *Medical Image Computing and Computer-Assisted Intervention - MICCAI 2013*, volume 8151 of *Lecture Notes in Computer Science*, pages 98–105, 2013.

M. Alhrishy, A. Varnavas, T. Carrell, A. King, and G. Penney. Interventional digital tomosynthesis from a standard fluoroscopysystem using 2D-3D registration. *Medical Image Analysis*, 19(1):137–148, 2015a.

M. Alhrishy, A. Varnavas, A. Guyot, T. Carrell, A. King, and G. Penney. Remapping of digital subtraction angiography on a standard fluoroscopy system using 2D-3D registration. In *SPIE Medical Imaging*, volume 9413, pages 94131O–94131O–14. International Society for Optics and Photonics, 2015b.

J. L. Anderson, J. L. Halperin, N. Albert, B. Bozkurt, R. G. Brindis, L. H. Curtis, D. DeMets, R. A. Guyton, J. S. Hochman, R. J. Kovacs, et al. Management of patients with peripheral artery disease (compilation of 2005 and 2011 ACCF/AHA guideline recommendations): a report of the American College of Cardiology Foundation/American Heart Association Task Force on Practice Guidelines. *Journal of the American College of Cardiology*, 61(14):1555–1570, 2013.

G. Bachar, J. H. Siewerdsen, M. J. Daly, D. A. Jaffray, and J. C. Irish. Image quality and localization accuracy in C-arm tomosynthesis-guided head and neck surgery. *Medical Physics*, 34:4664–4677, 2007.

G. Bachar, E. Barker, S. Nithiananthan, H. Chan, M. J. Daly, J. C. Irish, and J. H. Siewerdsen. Three-dimensional tomosynthesis and cone-beam computed

tomography: An experimental study for fast, low-dose intraoperative imaging technology for guidance of sinus and skull base surgery. *The Laryngoscope*, 119 (3):434–441, 2009.

J. A. Baker and J. Y. Lo. Breast tomosynthesis: state-of-the-art and review of the literature. *Academic Radiology*, 18(10):1298–1310, 2011.

L. W. Bartels and C. J. G. Bakker. Endovascular interventional magnetic resonance imaging. *Physics in Medicine and Biology*, 48(14):R37–R64, 2003.

A. H. Baydush, D. J. Godfrey, M. Oldham, and J. T. Dobbins III. Initial application of digital tomosynthesis with on-board imaging in radiation oncology. In *Medical Imaging*, pages 1300–1305. International Society for Optics and Photonics, 2005.

H. Bengtsson, B. Sonesson, and D. Bergqvist. Incidence and prevalence of abdominal aortic aneurysms, estimated by necropsy studies and population screening by ultrasounda. *Annals of the New York Academy of Sciences*, 800(1):1–24, 1996.

C. D. Bicknell. Occupational radiation exposure and the vascular interventionalist. *European Journal of Vascular and Endovascular Surgery*, 46(4):431, 2013.

K. Bliznakova, Z. Bliznakov, and I. Buliev. Comparison of algorithms for out-of-plane artifacts removal in digital tomosynthesis reconstructions. *Computer Methods and Programs in Biomedicine*, 107(1):75–83, 2012.

L. M. Boxt. Intravenous digital subtraction angiography of the thoracic and abdominal aorta. *Cardiovascular and Interventional Radiology*, 6(4-6):205–213, 1983.

A. R. Brady, S. G. Thompson, F. G. R. Fowkes, R. M. Greenhalgh, J. T. Powell, et al. Abdominal aortic aneurysm expansion risk factors and time intervals for surveillance. *Circulation*, 110(1):16–21, 2004.

W. R. Brody. Digital subtraction angiography. *Nuclear Science, IEEE Transactions on*, 29(3):1176–1180, 1982.

T. F. Browne, D. Hartley, S. Purchas, M. Rosenberg, G. Van Schie, and M. Lawrence-Brown. A fenestrated covered suprarenal aortic stent. *European Journal of Vascular and Endovascular Surgery*, 18(5):445–449, 1999.

T. W. G. Carrell, B. Modarai, J. R. I. Brown, and G. P. Penney. Feasibility and limitations of an automated 2D-3D rigid image registration system for complex endovascular aortic procedures. *Journal of Endovascular Therapy*, 17(4):527–533, 2010.

T. Cerciello, P. Bifulco, M. Cesarelli, and A. Fratini. A comparison of denoising methods for X-ray fluoroscopic images. *Biomed Signal Process Control*, 7(6): 550–559, 2012.

C. L. Chan, B. J. Sullivan, A. V. Sahakian, A. K. Katsaggelos, S. Swiryn, D. C. Hueter, and T. Frohlich. Simulation of quantum mottle in digital angiographic images. volume 1245, pages 104–110. International Society for Optics and Photonics, 1990.

W. R. Crum, T. Hartkens, and D. L. G. Hill. Non-rigid image registration: theory and practice. *British Journal of Radiology*, 77(suppl 2):S140–S153, 2004.

M. J. Daly, J. H. Siewerdsen, Y. B. Cho, D. A. Jaffray, and J. C. Irish. Geometric calibration of a mobile C-arm for intraoperative cone-beam CT. *Medical Physics*, 35(5):2124–2136, 2008.

S. Demirci, F. Manstad-Hulaas, and N. Navab. Quantification of abdominal aortic deformation after EVAR. volume 7261, pages 72611U–72611U. International Society for Optics and Photonics, 2009.

J. T. Dobbins and H. P. McAdams. Chest tomosynthesis: technical principles and clinical update. *European Journal of Radiology*, 72(2):244–251, 2009.

J. T. Dobbins III. Tomosynthesis imaging: at a translational crossroads. *Medical Physics*, 36(6):1956–1967, 2009.

J. T. Dobbins III and D. J. Godfrey. Digital x-ray tomosynthesis: current state of the art and clinical potential. *Physics in Medicine and Biology*, 48(19):65–106, 2003.

J. T. Dobbins III, H. P. McAdams, D. J. Godfrey, and C. M. Li. Digital tomosynthesis of the chest. *Journal of Thoracic Imaging*, 23(2):86–92, 2008.

C. L. Dumoulin, S. P. Souza, and R. D. Darrow. Real-time position monitoring of invasive devices using magnetic resonance. *Magnetic Resonance in Medicine*, 29 (3):411–415, 1993.

J. Duryea, J. T. Dobbins III, and J. A. Lynch. Digital tomosynthesis of hand joints for arthritis assessment. *Medical Physics*, 30(3):325–333, 2003.

M. J. Flynn, R. McGee, and J. Blechinger. Spatial resolution of x-ray tomosynthesis in relation to computed tomography for coronal/sagittal images of the knee. volume 6510, pages 65100D–65100D. International Society for Optics and Photonics, 2007.

A. Galea, A. Durran, T. Adlan, D. Gay, R. Riordan, P. Dubbins, and M. P. Williams. Practical applications of digital tomosynthesis of the chest. *Clinical Radiology*, 69(4):424–430, 2014.

D. J Godfrey, F. F. Yin, M. Oldham, S. Yoo, and C. Willett. Digital tomosynthesis with an on-board kilovoltage imaging device. *International Journal of Radiation Oncology* Biology* Physics*, 65(1):8–15, 2006.

D. J. Godfrey, L. Ren, H. Yan, Q. Wu, S. Yoo, M. Oldham, and F. F. Yin. Evaluation of three types of reference image data for external beam radiotherapy target localization using digital tomosynthesis (DTS). *Medical Physics*, 34(8): 3374–3384, 2007.

T. Gomi, H. Hirano, and M. Nakajima. X-ray digital tomosynthesis imaging: an appropriate reconstruction algorithm for arthroplasty. 2013.

P. A. Gordon and B. Toursarkissian. Treatment of abdominal aortic aneurysms: the role of endovascular repair. *AORN journal*, 100(3):241–259, 2014.

D. G. Grant. Tomosynthesis: a three-dimensional radiographic imaging technique. *Biomedical Engineering, IEEE Transactions on*, (1):20–28, 1972.

R. M. Greenhalgh. Comparison of endovascular aneurysm repair with open repair in patients with abdominal aortic aneurysm (EVAR trial 1), 30-day operative mortality results: randomised controlled trial. *The Lancet*, 364(9437):843–848, 2004.

M. Groher, M. Baust, D. Zikic, and N. Navab. Monocular deformable model-to-image registration of vascular structures. *Biomedical Image Registration*, 6204: 37–47, 2010.

A. Guyot. *Non-rigid 2D-3D registration for use in computer-assisted abdominal aortic aneurysm repair procedures*. PhD thesis, King's College London, PhD under preparation.

A. Guyot, A. Varnavas, T. Carrell, and G. Penney. Non-rigid 2D-3D registration using anisotropic error ellipsoids to account for projection uncertainties during aortic surgery. In *Medical Image Computing and Computer-Assisted Intervention–MICCAI 2013*, volume 8151, pages 179–186. Springer, 2013.

F. Haddad, R. K. Greenberg, E. Walker, J. Nally, S. ONeill, G. Kolin, S. P. Lyden, D. Clair, T. Sarac, and K. Ouriel. Fenestrated endovascular grafting: the renal side of the story. *Journal of Vascular Surgery*, 41(2):181–190, 2005.

C. B. Henk, C. B. Higgins, and M. Saeed. Endovascular interventional MRI. *Journal of Magnetic Resonance Imaging*, 22(4):451–460, 2005.

M. Hensel, T. Pralow, and R. R. Grigat. Modeling and real-time estimation of signal-dependent noise in quantum-limited imaging. In *Proceedings of the 6th WSEAS international conference on signal processing, robotics and automation, Corfu Island, Greece, ACM Proceedings*, ISPRA'07, pages 183–191, 2007.

B. J. Hillman, T. W. Ovitt, S. Nudelman, H. D. Fisher 3rd, M. M. Frost, M. P. Capp, H. Roehrig, and G. Seeley. Digital video subtraction angiography of renal vascular abnormalities. *Radiology*, 139(2):277–280, 1981.

J. H. Hipwell, G. P. Penney, R. A. McLaughlin, K. Rhode, P. Summers, T. C. Cox, J. V. Byrne, J. A. Noble, and D. J. Hawkes. Intensity-based 2-D-3-D registration of cerebral angiograms. *Medical Imaging, IEEE Transactions on*, 22(11):1417–1426, 2003.

H. H. Holm and B. Skjoldbye. Interventional procedures. *Ultrasound in Medicine & Biology*, 26:S131–S134, 2000.

J. Huang, J. K. Triedman, N. V. Vasilyev, Y. Suematsu, R. O. Cleveland, and P. E. Dupont. Imaging artifacts of medical instruments in ultrasound-guided interventions, journal = Journal of Ultrasound in Medicine. 26(10):1303–1322, 2007.

K. Kandarpa, P. Jakab, S. Patz, F. J. Schoen, and F. A. Jolesz. Prototype miniature endoluminal MR imaging catheter. *Journal of Vascular and Interventional Radiology*, 4(3):419–427, 1993.

C. Kauffmann, F. Douane, E. Therasse, S. Lessard, S. Elkouri, P. Gilbert, N. Beaudoin, M. Pfister, and G. Blair, J. F.and Soulez. Source of errors and accuracy of a two-dimensional/three-dimensional fusion road map for endovascular aneurysm repair of abdominal aortic aneurysm. *Journal of Vascular and Interventional Radiology*, 26(4):544–551, 2015.

T. Klinder, J. Ostermann, M. Ehm, A. Franz, R. Kneser, and C. Lorenz. Automated model-based vertebra detection, identification, and segmentation in CT images. *Medical Image Analysis*, 13(3):471–482, 2009.

Z. Kolitsi, G. Panayiotakis, V. Anastassopoulos, A. Scodras, N. Pallikarakis, et al. A multiple projection method for digital tomosynthesis. *Medical Physics*, 19(4): 1045–1050, 1992.

R. A. Kruger, C. Mistretta, S. J. Riederer, et al. Physical and technical considerations of computerized fluoroscopy difference imaging. *Nuclear Science, IEEE Transactions on*, 28(1):205–212, 1981.

A. Lacout, J. Thariat, A. Fohlen, and P. Y. Marcy. Tomosynthesis: a new chest imaging technique. *Diagnostic and Interventional Imaging*, 93(1):72–74, 2012.

F. A. Lederle, S. E. Wilson, G. R. Johnson, D. B. Reinke, F. N. Littooy, C. W. Acher, D. J. Ballard, L. M. Messina, I. L. Gordon, E. P. Chute, et al. Immediate repair compared with surveillance of small abdominal aortic aneurysms. *New England Journal of Medicine*, 346(19):1437–1444, 2002.

J. Lee, X Liu, A. K. Jain, J. L. Prince, and G. Fichtinger. Tomosynthesis-based radioactive seed localization in prostate brachytherapy using modified distance

map images. In *Biomedical Imaging: From Nano to Macro, 2008. ISBI 2008. 5th IEEE International Symposium on*, pages 680–683, 2008.

Y. M. Levakhina, J. Muller, R. L. Duschka, F. Vogt, J. Barkhausen, and T. M. Buzug. Weighted simultaneous algebraic reconstruction technique for tomosynthesis imaging of objects with high-attenuation features. *Medical Physics*, 40(3): 031106, 2013.

R. Liao, Y. Tan, H. Sundar, M. Pfister, and A Kamen. An efficient graph-based deformable 2D/3D registration algorithm with applications for abdominal aortic aneurysm interventions. In *Medical Imaging and Augmented Reality*, volume 6326 of *Lecture Notes in Computer Science*, pages 561–570. Springer, 2010.

J. S. Lindholt, N. H. H. Heegaard, S. Vammen, H. Fasting, E. W. Henneberg, and L. Heickendorff. Smoking, but not lipids, lipoprotein (a) and antibodies against oxidised LDL, is correlated to the expansion of abdominal aortic aneurysms. *European Journal of Vascular and Endovascular Surgery*, 21(1):51–56, 2001.

C. Y Liu, K. Farahani, D. S. K. Lu, G. Duckwiler, and A. Oppelt. Safety of MRI-guided endovascular guidewire applications. *Journal of Magnetic Resonance Imaging*, 12(1):75–78, 2000.

M. Manhart, Y. Zhu, and D. Vitanovski. Self-assessing image-based respiratory motion compensation for fluoroscopic coronary roadmapping. In *IEEE InternationalSymposium on Biomedical Imaging: From Nano to Macro*, pages 1065–1069. IEEE, 2011.

P. Markelj, D. Tomazevic, B. Likar, and F. Pernus. A review of 3D/2D registration methods for image-guided interventions. *Medical Image Analysis*, 16(3):642–661, 2012.

P. A. McCullough. Contrast-induced acute kidney injury. *Journal of the American College of Cardiology*, 51(15):1419–1428, 2008.

E. H. W. Meijering, W. J. Niessen, and M. A. Viegever. Retrospective motion correction in digital subtraction angiography: a review. *IEEE Transactions on Medical Imaging*, 18(1):2–21, 1999.

D. L. Miller. Interventional fluoroscopy: reducing radiation risks for patients and staff. *Journal of Vascular and Interventional Radiology*, 20(7):274–274, 2009.

K. Nash, A. Hafeez, and S. Hou. Hospital-acquired renal insufficiency. *American Journal of Kidney Diseases*, 39(5):930–936, 2002.

L. T. Niklason, B. T. Christian, L. E. Niklason, D. B. Kopans, D. E. Castleberry, B. H. Opsahl-Ong, C. E. Landberg, P. J. Slanetz, A. A. Giardino, R. Moore, et al. Digital tomosynthesis in breast imaging. *Radiology*, 205(2):399–406, 1997.

W. R. Nitz, A. Oppelt, W. Renz, C. Manke, M. Lenhart, and J. Link. On the heating of linear conductive structures as guide wires and catheters in interventional mri. *Journal of Magnetic Resonance Imaging*, 13(1):105–114, 2001.

K. Ogawa, R. P. Langlais, W. D. McDavid, M. Noujeim, K. Seki, T. Okano, T. Yamakawa, and T. Sue. Development of a new dental panoramic radiographic system based on a tomosynthesis method. *Development*, 39(1), 2010.

S. O'Neill, R. K. Greenberg, F. Haddad, T. Resch, J. Sereika, and E. Katz. A prospective analysis of fenestrated endovascular grafting: intermediate-term outcomes. *European Journal of Vascular and Endovascular Surgery*, 32(2):115–123, 2006.

A. P. Patel, D. Gallacher, R. Dourado, O. Lyons, A. Smith, H. Zayed, M. Waltham, T. Sabharwal, R. Bell, T. Carrell, et al. Occupational radiation exposure during endovascular aortic procedures. *European Journal of Vascular and Endovascular Surgery*, 46(4):424–430, 2013.

G. P. Penney, J. Weese, J. A. Little, P. Desmedt, D. L. G. Hill, et al. A comparison of similarity measures for use in 2D/3D medical imageregistration. *Medical Imaging, IEEE Transactions on*, 17(4):586–595, 1998.

G. P Penney, A. Varnavas, N. Dastur, and T. Carrell. An image-guided surgery system to aid endovascular treatment of complex aortic aneurysms: description and initial clinical experience. In *Information Processing in Computer-Assisted Interventions–IPCAI 2011*, volume 6689, pages 13–24. 2011.

D. P. Perrin, N. V. Vasilyev, P. Novotny, J. Stoll, R. D. Howe, P. E. Dupont, I. S. Salgo, and P. J. del Nido. Image Guided Surgical Interventions. *Current Problems in Surgery*, 2009.

T. M. Persons, R. L. Webber, P. F. Hemler, W. Bettermann, and J. D. Bourland. Brachytherapy volume visualization. In *Medical Imaging 2000*, volume 3976, pages 45–56. International Society for Optics and Photonics, 2000.

T Peters and K Cleary, editors. *Image Guided Interventions*. Springer US, 2008.

T. M. Peters. Image-guidance for surgical procedures. *Physics in Medicine and Biology*, 51(14):R505, 2006.

M. Prinssen, E. L. G. Verhoeven, J. Buth, P. W. M. Cuypers, M. R. H. M. van Sambeek, R. Balm, E. Buskens, D. E. Grobbee, and J. D. Blankensteijn. A randomized trial comparing conventional and endovascular repair of abdominal aortic aneurysms. *New England Journal of Medicine*, 351(16):1607–1618, 2004.

A. Puggioni, M. Kalra, M. Carmo, G. Mozes, and P. Gloviczki. Endovenous laser therapy and radiofrequency ablation of the great saphenous vein: analysis of early efficacy and complications. *Journal of Vascular Surgery*, 42(3):488–493, 2005.

A. Raheem, T. Carrell, B. Modarai, and G. Penney. Non-rigid 2D-3D image registration for use in Endovascular repair of Abdominal Aortic Aneurysms. In *Medical Image Understanding and Analysis–MIUA Proceedings 2010*, volume 15, pages 153–157, 2010.

V. K. Raman and R. J. Lederman. Interventional cardiovascular magnetic resonance imaging. *Trends in Cardiovascular Medicine*, 17(6):196–202, 2007.

R. Razavi, D. L. G. Hill, S. F. Keevil, M. E. Miquel, V. Muthurangu, S. Hegde, K. Rhode, M. Barnett, J. vanVaals, D. J. Hawkes, et al. Cardiac catheterisation guided by MRI in children and adults with congenital heart disease. *The Lancet*, 362(9399):1877–1882, 2003.

I. Reiser and S. Glick, editors. *Tomosynthesis Imaging*. Taylor & Francis Group, 2014.

J. J. Ricotta and G. S. Oderich. Fenestrated and branched stent grafts. *Perspectives in Vascular Surgery and Endovascular Therapy*, 20(2):174–187, 2008.

D. Robinson, B. Mees, H. Verhagen, J. Chuen, et al. Aortic aneurysms: screening, surveillance and referral. *Australian Family Physician*, 42(6):364, 2013.

K. Rohr, M. Fornefett, and H. S Stiehl. Approximating thin-plate splines for elastic registration: Integration of landmark errors and orientation attributes. In *Information Processing in Medical Imaging*, volume 1613 of *Lecture Notes in Computer Science*, pages 252–265. Springer, 1999.

S. Rudin, D. R. Bednarek, and K. R. Hoffmann. Endovascular image-guided interventions (EIGIs). *Medical Physics*, 35(1):301–309, 2008.

A. M. Sailer, M. W. de Haan, A. G. Peppelenbosch, M. J. Jacobs, J. E. Wildberger, and G. W. H. Schurink. CTA with fluoroscopy image fusion guidance in endovascular complex aortic aneurysm repair. *European Journal of Vascular and Endovascular Surgery*, 47(4):349–356, 2014.

J. F. Schenck, F. A. Jolesz, P. B. Roemer, H. E. Cline, W. E. Lorensen, R. Kikinis, S. G. Silverman, C. J. Hardy, W. D. Barber, and E. T. Laskaris. Superconducting open-configuration MR imaging system for image-guided therapy. *Radiology*, 195 (3):805–814, 1995.

M. L. Schermerhorn, A. J. O'Malley, A. Jhaveri, P. Cotterill, F. Pomposelli, and B. E Landon. Endovascular vs. open repair of abdominal aortic aneurysms in the Medicare population. *New England Journal of Medicine*, 358(5):464–474, 2008.

J. R. H. Scurr and R. G. McWilliams. Fenestrated aortic stent grafts. In *Seminars in Interventional Radiology*, volume 24, pages 211–220, 2007.

I. Sechopoulos. A review of breast tomosynthesis. Part II. Image reconstruction,processing and analysis, and advanced applications. *Medical Physics*, 40: 014302, 2013.

E. Seeliger, M. Sendeski, C. S. Rihal, and P. B. Persson. Contrast-induced kidney injury: mechanisms, risk factors, and prevention. *European Heart Journal*, 33 (16):2007–2015, 2012.

A. H. Seto, M. S. Abu-Fadel, J. M. Sparling, S. J. Zacharias, T. S. Daly, A. T. Harrison, W. M. Suh, J. A. Vera, C. E. Aston, R. J. Winters, et al. Real-time ultrasound guidance facilitates femoral arterial access and reduces vascular complications: FAUST (Femoral Arterial Access With Ultrasound Trial). *JACC: Cardiovascular Interventions*, 3(7):751–758, 2010.

D. Shimao, T. Kunisada, H. Sugiyama, and M. Ando. Shift-and-add tomosynthesis of a finger joint by X-ray dark-field imaging: Difference due to tomographic angle. *European Journal of Radiology*, 68(3):S27–S31, 2008.

T. Shiomi and T. Nishii. Clinical feasibility of tomosynthesis to evaluate bone remodeling after rotational acetabular osteotomy. *Osteoarthritis and Cartilage*, 22:S286–S287, 2014.

J. H. Siewerdsen, D. J. Moseley, S. Burch, S. K. Bisland, A. Bogaards, B. C. Wilson, and D. A. Jaffray. Volume CT with a flat-panel detector on a mobile, isocentric C-arm: pre-clinical investigation in guidance of minimally invasive surgery. *Medical Physics*, 32:241, 2005.

J. H. Siewerdsen, M. J. Daly, G. Bachar, D. J. Moseley, G. Bootsma, K. K. Brock, S. Ansell, G. A. Wilson, S. Chhabra, D. A. Jaffray, et al. Multimode C-arm fluoroscopy, tomosynthesis, and cone-beam CT forimage-guided interventions: from proof of principle to patient protocols. In *Medical Imaging*, volume 6510, pages 65101A–65101A. SPIE, 2007.

P. Skaane, R. Gullien, H. Bjorndal, E. B. Eben, U. Ekseth, U. Haakenaasen, G. Jahr, I. N. Jebsen, and M. Krager. Digital breast tomosynthesis (DBT): initial experience in a clinical setting. *Acta Radiologica*, 53(5):524–529, 2012.

H. J. Teertstra, C. E. Loo, M. A. A. J. van den Bosch, H. van Tinteren, E. J. T. Rutgers, S. H. Muller, and K. G. A. Gilhuijs. Breast tomosynthesis in clinical practice: initial results. *European Radiology*, 20(1):16–24, 2010.

M. M. Thompson. Controlling the expansion of abdominal aortic aneurysms. *British Journal of Surgery*, 90(8):897–898, 2003.

A. Tingberg. X-ray tomosynthesis: a review of its use for breast and chest imaging. *Radiation Protection Dosimetry*, 139(1-3):100–107, 2010.

J. M. Tobis, O. Nalcioglu, and W. L. Henry. Digital subtraction angiography. *Chest Journal*, 84(1):68–75, 1983.

I. B. Tutar, R Managuli, V. Shamdasani, P. S. Cho, S. D. Pathak, and Y. Kim. Tomosynthesis-based localization of radioactive seeds in prostate brachytherapy. *Medical Physics*, 30(12):3135–3142, 2003.

G. R. Upchurch and T. A Schaub. Abdominal aortic aneurysm. *American Family Physician*, 73(7):1198–204, 2006.

K. A. Vardulaki, N. M. Walker, N. E. Day, S. W. Duffy, H. A. Ashton, and R. A. P. Scott. Quantifying the risks of hypertension, age, sex and smoking in patients with abdominal aortic aneurysm. *British Journal of Surgery*, 87(2):195–200, 2000.

M. J. Wallace, M. D. Kuo, C. Glaiberman, C. A. Binkert, R. C. Orth, and G. Soulez. Three-dimensional C-arm cone-beam CT: applications in the interventional suite. *Journal of Vascular and Interventional Radiology*, 19(6):799–813, 2008.

T. V. Walsum, K. J. Zuiderveld, J. W. C. Chin-A-Woeng, B. C Eikelboom, and M. A. Viergever. CT-based simulation of fluoroscopy and DSA for endovascular surgery training. In *CVRMed-MRCAS'97*, volume 1205, pages 273–282. Springer, 1997.

R. L. Webber, R. A. Horton, D. A. Tyndall, and J. B. Ludlow. Tuned-aperture computed tomography (TACT). Theory and application for three-dimensional dento-alveolar imaging. *Dentomaxillofacial Radiology*, 26(1):53–62, 1997.

J. Weese, G. P. Penney, P. Desmedt, T. M. Buzug, D. L. G. Hill, and D. J Hawkes. Voxel-based 2-D/3-D registration of fluoroscopy images and CT scans for image-guided surgery. *Information Technology in Biomedicine, IEEE Transactions on*, 1(4):284–293, 1997.

T. Wilmink, C. R. G. Quick, C. S. Hubbard, and N. E. Day. The influence of screening on the incidence of ruptured abdominal aortic aneurysms. *Journal of Vascular Surgery*, 30(2):203–208, 1999.

D. J. Withers and R. J. Ashleigh. Inspiration or expiration? Reducing motion artefact in digital subtraction arch angiography of the extracranial carotid arteries. *The British Journal of Radiology*, 68(813):1017–1020, 1995.

Q. J. Wu, D. J. Godfrey, Z. Wang, J. Zhang, S. Zhou, S. Yoo, D. M. Brizel, and F. Yin. On-board patient positioning for head-and-neck IMRT: Comparing digital tomosynthesis to kilovoltage radiography and cone-beam computed tomography. *International Journal of Radiation Oncology* Biology* Physics*, 69(2):598–606, 2007.

T. Wu, R. H. Moore, E. A. Rafferty, and D. B. Kopans. A comparison of reconstruction algorithms for breast tomosynthesis. *Medical Physics*, 31:2636, 2004.

S. Yoo, Q. J. Wu, D. Godfrey, H. Yan, L. Ren, S. Das, W. R. Lee, and F. Yin. Clinical evaluation of positioning verification using digital tomosynthesis and bony anatomy and soft tissues for prostate image-guided radiotherapy. *International Journal of Radiation Oncology* Biology* Physics*, 73(1):296–305, 2009.

P. A. Yushkevich, J. Piven, H. C. Hazlett, R. G. Smith, S. Ho, J. C. Gee, and G. Gerig. User-guided 3D active contour segmentation of anatomical structures: significantly improved efficiency and reliability. *Neuroimage*, 31(3):1116–1128, 2006.

List of Publications

Articles in Journals

- **M. Alhrishy**, A. Varnavas, T. Carrell, A. King, and G. Penney. Interventional digital tomosynthesis from a standard fluoroscopysystem using 2D-3D registration. *Medical Image Analysis*, 19(1):137148, 2015a.

Articles in conference proceedings

- **M. Alhrishy**, A. Varnavas, A. Guyot, T. Carrell, A. King, and G. Penney. Remapping of digital subtraction angiography on a standard fluoroscopy system using 2D-3D registration. In *SPIE Medical Imaging*, volume 9413, pages 94131O-94131O-14. International Society for Optics and Photonics, 2015b.

- **M. Alhrishy**, A. Varnavas, T. Carrell, A. King, and G. Penney. Interventional digital tomosynthesis from a standard fluoroscopy system using 2D-3D registration. In *Medical Image Computing and Computer-Assisted Intervention - MICCAI 2013*, volume 8151 of Lecture Notes in Computer Science, 2013. ISBN 978-3-642-40759-8